

UCLA

UCLA Electronic Theses and Dissertations

Title

Application of Atmospheric Pressure Plasma in Polymer and Composite Adhesion

Permalink

<https://escholarship.org/uc/item/8wk0h26p>

Author

Yu, Hang

Publication Date

2015

Peer reviewed|Thesis/dissertation

UNIVERSITY OF CALIFORNIA

Los Angeles

Application of Atmospheric Pressure Plasma in Polymer and Composite Adhesion

A dissertation submitted in partial satisfaction of the
requirement for the degree Doctorate of Philosophy
in Chemical Engineering

by

Hang Yu

2015

Abstract of the Dissertation

Application of Atmospheric Pressure Plasma in Polymer and Composite Adhesion

By

Hang Yu

Doctor of Philosophy in Chemical Engineering

University of California, Los Angeles, 2015

Professor Robert F. Hicks, Chair

An atmospheric pressure helium and oxygen plasma was used to investigate surface activation and bonding in polymer composites. This device was operated by passing 1.0-3.0 vol% of oxygen in helium through a pair of parallel plate metal electrodes powered by 13.56 or 27.12 MHz radio frequency power. The gases were partially ionized between the capacitors where plasma was generated. The reactive species in the plasma were carried downstream by the gas flow to treat the substrate surface. The temperature of the plasma gas reaching the surface of the substrate did not exceed 150 °C, which makes it suitable for polymer processing. The reactive species in the plasma downstream includes $\sim 10^{16}$ - 10^{17} cm⁻³ atomic oxygen, $\sim 10^{15}$ cm⁻³ ozone molecule, and $\sim 10^{16}$ cm⁻³ metastable oxygen molecule ($O_2^1\Delta_g$). The substrates were treated at 2-5 mm distance from the exit of the plasma. Surface properties of the substrates were characterized using water contact angle (WCA), atomic force microscopy (AFM), infrared spectroscopy (IR), and X-ray photoelectron spectroscopy (XPS). Subsequently, the plasma treated samples were bonded adhesively or fabricated into composites. The increase in mechanical strength was correlated to changes in the material composition and structure after

plasma treatment. The work presented hereafter establishes atmospheric pressure plasma as an effective method to activate and to clean the surfaces of polymers and composites for bonding. This application can be further expanded to the activation of carbon fibers for better fiber-resin interactions during the fabrication of composites.

Treating electronic grade FR-4 and polyimide with the He/O₂ plasma for a few seconds changed the substrate surface from hydrophobic to hydrophilic, which allowed complete wetting of the surface by epoxy in underfill applications. Characterization of the surface by X-ray photoelectron spectroscopy shows formation of oxygenated functional groups, including hydroxyl, carbonyl, and carboxyl groups, on the polymer surface after plasma treatment. The resulting strength of the bond based on lap-shear and T-peel tests correlates well with the concentration of oxygen on the polymer surface. The failure modes observed for lap-shear and T-peel tests changed from interfacial to cohesive after the plasma activation.

Treating carbon-fiber-reinforced epoxy composites with the atmospheric plasma resulted in the removal of fluorinated contaminants in shallow surface layers. For contaminants that diffused deeply into the composite surface, mechanical abrasion was needed in addition to the plasma treatment to remove the impurities. While cleaning the composite, plasma also generated active oxygen groups on the substrate surface. The presence of these groups improved the adhesive bonding strength of the composite even in the presence of residual fluorine contaminants. Thus, it was speculated that plasma treatment can promote better polymer adhesion with or without fluorine contamination.

Carbon nanotube sheets were also treated by the helium oxygen plasma, and the CNT surface turn from super hydrophobic to hydrophilic after a few seconds of exposure. The

nanotube surface contained 15 % of oxygen in the form of hydroxyl groups. Chemical coupling agents were added to the plasma activated CNT surfaces in order to crosslink the CNTs and to create bonding sites for the resin matrix. Stretched, activated and functionalized CNT was cured with dicyclopentadiene (DCPD) to produce a sheet composite with a tensile strength of 636 MPa, a modulus of 28 GPa, and a density of 1.4 g/cm³. This may be compared to aerospace-grade aluminum with tensile strength of 572 MPa, modulus of 72 GPa, and density of 2.7 g/cm³. This work demonstrates that new high-strength composite can be produced with the use of atmospheric plasma activation and chemical crosslinking of the fiber matrix.

The dissertation of Hang Yu is approved.

Yunfeng Lu

Suneel Kodambaka

Robert F. Hicks, Committee Chair

University of California, Los Angeles,

2015

DEDICATION

I would like to dedicate this dissertation to my parents Joshua (Zengshou) Yu and Joy (Xien) Wang for all that they have done in supporting me up until this point. I would also like to dedicate this work to professor Robert Hicks and Mrs. Carol Hicks for their kindness towards me during my time at UCLA. Lastly, I would like to dedicate this to my beloved wife to be, Tuotuo Wang. May this be the beginning of a beautiful life that we shall enter together.

TABLE OF CONTENTS

Abstract of the dissertation		ii
Dedication		vi
List of Figures		i x
List of Tables		xiii
Acknowledgement		xv
Vita		xvi
Chapter 1	An Introduction to Polymer Surface Preparation for Bonding	1
	References	11
Chapter 2	Atmospheric and Vacuum Plasma Treatments of Polymer Surfaces for Enhanced Adhesion in Microelectronics Packaging	18
	References	71
Chapter 3	Surface Preparation using Atmospheric Pressure Plasma for Adhesive Bonding of Carbon-Fiber-Reinforced Epoxy Laminates	84
	References	109
Chapter 4	Rapid Oxidative Activation of Carbon Nanotube Yarn and Sheet by a Radio Frequency, Atmospheric Pressure Helium and Oxygen Plasma	112
	References	147

Chapter 5	Thermal, Electrical and Tensile Characterization of CNT/DCPD Sheet Composites	153
	References	177

LIST OF FIGURES

Figure 1.1	Possible fracture interfaces during peel ply removal.	6
Figure 2.1	Assembled plastic ball-grid-array package.	20
Figure 2.2	Different types of plasma used for surface preparation.	26
Figure 2.3	Concentration of reaction species as function of distance from the exit of the atmospheric pressure RF He/O ₂ plasma.	33
Figure 2.4	Water contact angle of polymers before and after activation with dielectric barrier discharge or RF capacitive discharge.	41
Figure 2.5	Dependence of water contact angle of FR-4 on exposure time to the atmospheric pressure He/O ₂ plasma.	47
Figure 2.6	The oxygen atomic percentage on the FR-4 surface as a function of exposure time to the atmospheric pressure He/O ₂ plasma.	50
Figure 2.7	The XPS carbon 1s spectra for FR-4 before and after exposure to the atmospheric pressure He/O ₂ plasma.	51
Figure 2.8	Distribution of oxidized carbon groups on FR-4 surface before and after atmospheric pressure He/O ₂ plasma treatment.	52
Figure 2.9	Dependence of the lap-shear strength of epoxy bonded FR-4 on exposure time to the atmospheric pressure He/O ₂ plasma.	54
Figure 2.10	The lap-shear fracture interface of FR-4 coupons with and without exposure to the atmospheric pressure He/O ₂ plasma before bonding.	57
Figure 2.11	Dependence of the water contact angle of polyimide on exposure time to the atmospheric pressure He/O ₂ plasma.	60

Figure 2.12	The oxygen atomic percentage on the polyimide surface as a function of exposure time to the atmospheric pressure He/O ₂ plasma.	63
Figure 2.13	The XPS carbon 1s spectra for polyimide before and after exposure to the atmospheric pressure He/O ₂ plasma.	64
Figure 2.14	Distribution of oxidized carbon groups on the polyimide surface before and after the atmospheric pressure He/O ₂ plasma treatment.	65
Figure 2.15	T-peel failure mode of polyimide bonded with and without treatment by atmospheric pressure He/O ₂ plasma.	67
Figure 3.1	An XPS survey spectra of 5320-1 fabricated with and without peel ply.	90
Figure 3.2	Survey spectra of 977-3, 5320-1, and MTM45-1 fabricated without peel ply.	91
Figure 3.3	The XPS carbon 1s spectrum of 5320-1 AW before and after 15s of plasma treatment.	95
Figure 3.4	Oxygen concentration on the surface of 5320-1 PPAW as a function of plasma exposure time.	97
Figure 3.5	Fraction of oxidized carbon and functional groups as a function of plasma exposure time for 5320-1 PPAW.	98
Figure 3.6	Oxygen concentration on the surface of 5320-1 PPSAW as a function of plasma exposure time.	99
Figure 3.7	Carbon bonding states on the surface of 5320-1 PPSAW as a function of plasma exposure time.	101
Figure 4.1	Water contact angles recorded on CNT sheets before and after 30s of plasma treatment.	119
Figure 4.2	Dependence of water contact angle on plasma exposure time on	121

the front and back side of the carbon nanotube sheet.

Figure 4.3	X-ray photoemission survey spectra of the CNT as a function of plasma exposure time.	123
Figure 4.4	The XPS C1s photoemission spectrum of CNT sheets with and without 30s of plasma activation.	125
Figure 4.5	The oxygen to carbon ratio as a function of plasma exposure time from the O1s peaks and from the oxidized C1s peaks.	128
Figure 4.6	Infrared single beam spectrum of CNT sheet following increasing plasma exposure time.	130
Figure 4.7	Infrared absorbance spectrum of CNT as a function of exposure time to the plasma.	131
Figure 4.8	Carbon nanotube yarn exposed to plasma, to wet chemicals, and dispersed in the resin monomer.	133
Figure 4.9	Scanning electron micrograph of CNT sheets before and after plasma treatment.	134
Figure 4.10	The electrical resistivity of CNT yarn as a function of the plasma exposure time and of the oxygen to carbon ration on CNT.	136
Figure 4.11	The tensile strength of CNT yarn as a function of plasma exposure Time.	138
Figure 4.12	Dependence of the concentration of neutral species on distance from the exit of the atmospheric pressure plasma.	139
Figure 4.13	A proposed mechanism for the oxidation of carbon nanotubes by exposure to the atmospheric pressure He/O ₂ plasma.	145
Figure 5.1	TGA mass loss and derivative mass loss of CNT/DCPD composites.	159

Figure 5.2	Nitrogen adsorption isotherm of CNT sheets before and after stretching	161
Figure 5.3	Stress and strain curve of CNT sheet and CNT/DCPD composite	164
Figure 5.4	SEM images of CNT sheet before and after stretching	168
Figure 5.5	Top down and cross section image of a 10-ply CNT composite	175

LIST OF TABLES

Table 2.1	Breakdown voltages, electron impact ionization thresholds and cross sections for helium, argon, nitrogen and oxygen.	23
Table 2.2	Physical properties of vacuum and atmospheric pressure plasmas.	30
Table 2.3	Water contact angle and surface roughness of FR-4, solder mask, and polyimide before and after vacuum plasma treatment.	35
Table 2.4	Carbon-to-oxygen atom ratio on the surface of FR-4, soldermask, and polyimide before and after vacuum plasma treatment in different plasma gases.	38
Table 2.5	Effect of vacuum plasma treatment on adhesion between epoxy underfill and three polymer substrates.	39
Table 2.6	The effect of atmospheric plasma activation on the surface composition of polymers.	43
Table 2.7	Surface energy and lap-shear strength of epoxy bonded polymers before and after atmospheric pressure plasma activation.	44
Table 2.8	Dependence of FR-4 surface roughness on exposure time to the atmospheric pressure He/O ₂ plasma.	48
Table 2.9	First-order rate constants determined for FR-4 surface property changes with plasma treatment.	56
Table 2.10	Dependence of polyimide surface roughness on exposure time to the atmospheric pressure He/O ₂ plasma.	61
Table 3.1	Plasma oxidation parameters for composite systems.	88

Table 3.2	Effect of peel ply and peel ply plus sanding on the surface chemistry of 5320-1 AW epoxy composite.	93
Table 3.3	Effect of plasma oxidation on the surface chemistry of 5320-1 AW epoxy composite.	94
Table 3.4	Effects of mechanical abrasion on the surface chemistry of 977-3 composite.	102
Table 3.5	Effects of plasma oxidation on the surface chemistry of 977-3 composite.	103
Table 3.6	Combined effects of mechanical abrasion and plasma oxidation on the surface chemistry of 977-3 composite.	105
Table 4.1	Carbon distribution on the surface of plasma treated carbon nanotube sheets.	127
Table 4.2	Atomic oxygen and ozone concentrations reported for the plasma systems used to treat carbon nanotubes.	141
Table 4.3	Effect of treatment method and time on the extent of oxidation and distribution of oxidized species on the surface of nanotubes.	142
Table 5.1	Electrical and thermal properties of CNT/DCPD composite	161
Table 5.2	Tensile properties of CNT/DCPD sheet composites CNT/DCPD composite.	163
Table 5.3	Tensile strength and elastic modulus of CNT sheet composite in this and previous work.	170
Table 5.4	Density, tensile strength, Young's modulus, and elongation to failure of the CNT composite, carbon fiber composite, aluminum 7075-T6 and Nomex® paper.	174

ACKNOWLEDGEMENT

First of all I should thank God for creating me. I would like to thank my parents, Joshua (Zengshou) Yu and Joy (Xien) Wang for bringing me to this world and for supporting me for all this years, allowing me to pursue my ambitious. I may have been ungrateful from time to time, but I truly appreciate all that they have done for me. I would also like to thank my thesis advisor Professor Hicks, for being a fantastic mentor, teaching to me to design, execute, and present my research work. In addition, both professor Hicks and Mrs. Carol Hicks have been very kind to me, in a way it is almost like a second family out here in Los Angeles.

I would like to thank my committee members, Professor Jane P. Chang, Professor Yunfeng Lu, and Professor Kodambaka Suneel, for taking the time out of their busy schedule to provide me with the guidance in this thesis work. Professor Lu especially, in addition to being a thesis advisor, has also acted as a counselor to me in times of crisis.

I would also like to thank Huihui Zhou for her support over the past three years both as a good friend and as a fellow material chemist/engineer. It will be unfair for me to not acknowledge my former and current co-workers, especially Dr. Dick Cheng, Dr. Thomas Williams, and Dr. Joseph Severino, much of the work in this thesis were completed as collaborate effort with these gentlemen. I would also like to thank Igor De Rosa from UCLA Material Science Department and Misha Grigoriev from Aerospace Material Processing for providing me with guidance in composite manufacturing.

Last but not least, I really want to appreciate my brothers and sisters from Life Christian fellowship and Life Baptist Church for their mental and spiritual supports.

VITA

Aug 2003- 2007	University of California - Berkeley Bachelor of Science in Chemical Engineering Overall GPA: 3.24	Berkeley, CA
2007-2009	Applied Materials Inc. Process Engineer in Blanket Dielectric Film Division	Santa Clara, CA
2010-2015	University of California-Los Angeles Ph.D. Candidate in Chemical Engineering Overall GPA: 3.90	Los Angeles, CA

Publications:

Chapter in Books

1. Yu, H., Zhang, Y. Y., Wong, A., De Rosa, I. M., Chueh, H. S., Grigoriev, M., Williams, T. S., Hsu, T., and Hicks, R. F., "Atmospheric and Vacuum Plasma Treatment of Polymer Surfaces for Enhanced Adhesion in Microelectronics Packaging," in *Adhesion in Microelectronics*, Mittal, K. L., and Ahsan, T., Eds., pp. 137-172, Wiley-Scrivener, Beverly, MA (2014).

Journal Articles

1. Williams, T. S., Yu, H., Yeh, P. C., Yang, J. M., and Hicks, R. F., "Atmospheric pressure plasma effects on adhesive bonding properties of stainless steel and epoxy composites," *J. Compos. Mater.* **48**, 219-233, 2014.
2. Sun, S. Y., Yu, H., Williams, T. S., Hicks, R. F., and Qiu, Y. P., "Eco-friendly sizing technology of cotton yarns with He/O₂ atmospheric pressure plasma treatment and green sizing recipes" *TEXT. RES. J.* **83**, 2177-2190, 2013.
3. Li, Y. J., Zhu, E. B., Chen, Y., Chiu, C. Y., Yu, H., Huang, X. Q., Hicks, R. F., and Huang, Y., "Gold clusters alloyed to nanoporous palladium surfaces as highly active bimetallic oxidation catalysts," *ChemSusChem* **6**, 1868-1872, 2013.
4. Yu, H., Cheng, D., Williams T. S., Severino, J. De Rosa I. M., Carlson, L., and Hicks, R. F., "Rapid oxidative activation of carbon nanotube yarn and sheet by a radio frequency, atmospheric pressure, helium and oxygen plasma," *Carbon* **57**, 11-21, 2013.
5. Williams, T. S., Yu, H., and Hicks, R. F., "Atmospheric pressure plasma activation as a surface pre-treatment for the adhesive bonding of aluminum 2024," *J. Adhes. Sci. Technol.* **28**, 653-674, 2013.
6. Williams, T. S., Yu, H., and Hicks, R.F., "Atmospheric pressure plasma activation of polymer and composite for adhesive bonding," *Rev. Adhes. Adhes.* **1**, 46-87, 2013.
7. Baio, J. E., Yu, H., Flaherty, D. W., Winters, H. F., and Graves, D. B., "Electron-impact dissociation cross sections for CHF₃ and C₃F₈," *J. Phys. D: Appl. Phys.* **40**, 6969-6974, 2007.

8. Characterization of the thermal, electrical and mechanical properties of CNT/DCPD sheet composites, in progress.

Symposium Proceeding

1. Yu, H., Hicks, R.F., Grigoriev, M., Palmer, M. J., and Cheng, D., "Surface preparation using atmospheric pressure plasma for adhesive bonding of carbon-fiber-reinforced epoxy laminates" to be published in 2014 SAMPE Annual Technical Conference Proceedings, Seattle, WA, June 2-6, 2014.

Conference Presentation

1. Yu, H., "Activation of carbon nanotube yarn and sheet by radio frequency atmospheric pressure plasma" De Novo Carbon Session, Material Research Society Spring Meeting, San Francisco, CA, April 12, 2012.

Patents

1. Yu, H., Padhi, D., Cai, M. P., Yoshida, N., Miao, L. Y., Cheng, S. F., Shaikh, S., Park, S., Park, H. L., Kim, B. H., "Amorphous carbon deposition method for improved stack defectivity," U.S. Patent No. 8349741 B2, January 8, 2013.
2. Du, B. D., Ayoub, M., Kim, R., Bansal, A., Fodor, M., Nguyen, B., Cheng, S. F., Yu, H., Chan, C., Balasubramani, G., Padhi, D., Rocha, J., "Shadow ring for modifying wafer edge and bevel deposition," Patent No. WO 2011082020 A3, November 17, 2011.
3. Zhou, J. H., Padhi, D., Janakiraman, K., Cheng, S. F., Yu, H., Saripalli, Y. N., Summan, T., "Nonplanar faceplate for a plasma processing chamber," Patent No. WO 2009134588 A3, March 18, 2010.

Chapter 1

An Introduction to Polymer Surface Preparation for Bonding

1.1 Introduction

Macromolecular polymers are of great technological importance to modern society. They have replaced metal and ceramic in applications all across the aerospace, automobile, consumer goods, electronic, and medical industries, and they have enabled new products unavailable previously. Plastic, in comparison to metal and ceramic, is lighter, easier to process, and more resistant to corrosion [1]. In applications where high strength is required, fiber reinforcement can be added to the polymer matrix to produce composites with mechanical properties comparable to those of aluminum and steel. In contrast to metals, plastics are bonded together adhesively instead of by mechanical fasteners. The advantage of adhesive bonding includes weight reduction, uniform load distribution across the bonding surface, resistance to corrosion, and conformance to complex aerodynamic contours [2]. This, however, means that the quality of the bond between polymer and the adhesive plays a crucial role in these materials for structural applications.

Wu et al. [3] has defined adhesion as the state in which two dissimilar bodies are held together by intimate interfacial contact, such that the mechanical force or work can be transferred across the interface. The interfacial forces holding the two phases together may arise from van der Waal forces, chemical bonding, or electrostatic interaction. The mechanical strength of the system is determined not only by the interfacial forces, but also by the mechanical properties of the interfacia and the two bulk phases. Surfaces of

commercial polymers are frequently smooth with inherently low surface energy, which makes them difficult to bond [4]. Surface preparation methods can be utilized to enhance adhesive strength by promoting higher surface energy, increased surface roughness, and modified surface chemistry. In short, proper preparation of the polymer surface will enhance the polymer bonding strength and enables its uses in applications where applied stress is present.

1.2 Polymers

Plastics can be broken down into two categories, thermosets and thermoplastics. Thermosets start as a liquid at low temperature, but cure irreversibly with catalyst or heat by polymer cross-linking. The cross-linking process transforms the thermosetting polymers into a rigid 3-D structure with high molecular weight. Thermosets have high melting temperature, and in most cases, melt above the decomposition temperature. Thermosets, as the name suggests, cannot be melted or reshaped after they have been cured. Thermoplastics are constructed of high-molecular-weight, long-chain polymers associated by intermolecular forces. Due to the lack of chemical bonds in their 3-D structure, thermoplastics, when heated above the glass transition temperature, become soft and malleable, capable of being reshaped. Thermosets are often selected based on their ability to withstand heat and pressure for long periods of time without failure. Thermoplastics, though not as strong and stable as thermosets, have higher impact resistance. Their ability to be shaped also makes them more valuable for certain applications. Despite their differences, thermosets and thermoplastics are difficult to bond [5-7]. Plastics have smooth surface with low surface energy, which can prevent

uniform adhesive coverage as well as strong chemical bonds between the adhesive the polymer.

1.3 Fiber reinforced composites

Polymer resins can be mixed with fibers, including glass, carbon, aramid, and carbon nanotubes to achieve superior mechanical, thermal, and electrical properties. The annual demand for fiber reinforced composites (FRC) in the United States is about 4% of domestic plastic production, and this number continues to rise [8-9]. Composites are widely used in aerospace, automotive and sports equipment. A challenge to the manufacturing of FRC is the weak interaction between the fiber and the resin [10-11]. The surface of carbon fibers, aramid fibers, and carbon nanotubes are composed of conjugated aromatic groups, which give them low surfaces energy and chemical inertness. These fibers are not easily wetted by the resin, and they are even less inclined to bond chemically. A key to increase the contribution of fiber strength in the composite is to create chemical crosslinks between the fiber and the resin. The fibers can be treated with plasma to enhance their bondability.

1.4 Existing methods to prepare polymer surface for bonding

The aim of plastic surface treatment is to increase wettability, create sites for adhesion, and promote stronger bonds across the interface [5]. In any surface preparation procedure, the first step must be cleaning and removal of dirt, grease and other contaminants from the surface [3,5]. When strong adhesion is required, additional steps involving mechanical abrasion, wet chemical etching, and plasma activation may be used.

Traditional plastic surface preparation uses organic solvents to degrease and remove organic contaminants. In the past, solvents used for degreasing include trichloroethylene and perchloroethylene, and the treatment consists of wiping the surface of the plastic with a cloth saturated with the solvent [13-14]. Due to the toxic nature of these solvents, such a treatment usually requires specific vapor-degreasing units, and the banning of chlorinated solvents has eliminated their use. More recently, the joint surfaces have been cleaned by wiping with a lint-free cloth soaked with acetone followed by the complete evaporation of acetone. Acetone, however, is still considered a toxic solvent, thus this task must be carried out in a well ventilated work environment.

In composite manufacturing for aerospace, nylon or polyester peel-ply is utilized for surface preparation during the fabrication of thermoset composites [5,15,16]. Peel-ply adheres to the surface of the composite laminate during its construction. It protects the laminate from dirt, dust, and tool-side grease. Composite laminates covered with peel ply can be store for up to months, and when needed, the ply is removed to create a fresh surface for bonding. The peel-ply covered samples require only a minimal amount of preparation. However, the peel-ply procedure has its drawbacks. Dry plies tend to leave fiber residues as well as lubricants from the fiber weaving on the resin surface [15-17]. More recent plies are pre-impregnated with low toughness resins layers to avoid the deposition of fiber on the bonding surface. However, the pattern of ply weaving is still transferred onto the laminate. In addition, manufacturers of the peel-ply continue to utilize fluorine or silicone based lubricants to ensure easy release of the ply from the laminate. Residues of the lubricants are frequently left on the bonding surfaces, and worst yet, fluorine and silicone can diffuse into the resin matrix when the laminate is

being cured. This results in the need for mechanical abrasion following peel-ply removal. In addition, peel ply removal can damage to the bulk laminate. Figure 1.1 shows a schematic of a fiber-reinforced-composite covered with peel-ply. Lines marked 1-4 indicate ways that the peel-ply can be removed from the laminate surface. Line 1 is the ideal case in which removing peel-ply leaves a thin layer of the resin matrix covering the fiber-reinforcement. Line 2 shows the scenario where ply-fiber has been lifted off leaving lubricant or impregnate residues on the surface. Line 3 shows a case where the peel-ply cannot be fully removed, leaving much of the fiber behind. Line 4 shows the case where top layers of the resin matrix and fiber-reinforcement have been removed along with the peel ply, thus cracking and damaging the composite [15-16].

Previous work has shown that stronger joints can be fabricated by using a combination of peel-ply with mechanical abrasion [18]. Mechanical abrasion is used to increase the surface roughness and thus the available contact area for bonding. During abrasion, residual contaminants are removed from the resin surface. The current state-of-art procedure for mechanical abrasion is grit blast. Grit blasting operates by propelling a stream of abrasive material under high pressure to modify the topography. This procedure is labor intensive and requires a containment system for the abrasive media. An alternative abrasive treatment is hand sanding. Previous work shows that the surface roughness of thermoset composite is significantly increased by sanding [19-20]. However, the abrasion of thermoplastics tend to show lesser improvement due to the low surface energy [5-7]. Like peel-ply, a drawback of the abrasion techniques is the lack of a quantitative standard for sample readiness for bonding. The operator determines when the proper surface state is achieved based on visual criteria, which can easily lead to

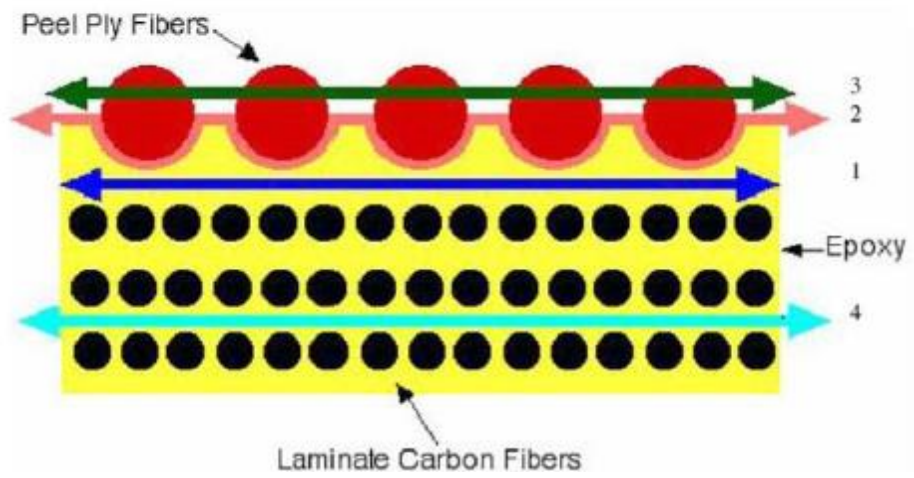


Figure 1.1. Possible fracture interfaces of peel ply removal [18].

under-preparation and poor adhesion, or over-treatment and structural damage. Furthermore, abrasion leaves loose particles on the surface, which requires subsequent solvent cleaning [21].

In addition to changing surface roughness, creating chemically active bonding sites on the polymer surface is another approach to promote better adhesion. The procedures to modify the polymer surface chemistry can be carried out by either liquid phase or gas phase processes [22]. Liquid-phase surface activation uses strong oxidants, either aqueous acids [23-26] or bases [27]. The oxidation reaction leads to the formation of carbonyl [23,24] and carboxylic acid groups [25,26] on polymer surface. Mineral acids, such as sulfuric acid and nitric acid, can generate small quantities of sulfonate and amine moieties on the surface. Similarly, exposing polymers to oxidative gases can generate surface functional groups such as hydroxyls, carbonyls and carboxylic acids. The drawbacks of using strong oxidants, include difficulty in generating a single type of surface functional group and tendency to over etch and damage the substrate. Furthermore, strong acids and bases may be dangerous to handle and to explosive to dispose of, which leads to higher operating cost.

Gas phase oxidation of polymer surfaces is enhanced by employing UV light, electron beams, and plasma discharge. The external energy sources break down oxygen molecules into reactive species such as ions, atomic oxygen, and ozone [28]. Among these methods, weakly ionized plasmas have been extensively used to functionalize polymer surfaces. A plasma is an electrically neutral ionized gas. It can be “hot” or thermal plasma if nearly all the species are ionized, otherwise it is “cold” or non-thermal

plasma, where only a small fraction of the species are ionized, i.e., 1- 100 parts per billion. In a hot plasma, the electron energy (T_e) is in equilibrium with the ion energy (T_i) [28-31], and the gas temperature T_g can range from 5,000 to 50,000 degrees Kelvin [28,31]. It is impossible to use such a high gas temperature in polymer processing without damaging the substrate. Therefore, the majority of the industrial plasmas are weakly ionized [28,31]. The neutral gas temperature, T_g , of a partially ionized discharge is much lower than its electron energy, i.e., between 300 and 600 °K. The plasma gas contains atoms, metastable molecules, in addition to electrons, ions, and ground-state molecules. The plasma is generated by exposing the feed gas to an electrical field, and when the field strength exceeds the breakdown voltage of the gas, free electrons and ions are generated. Subsequent inelastic collision between high energy electrons and the feed gas sustains the plasma.

Commercial plasmas can operate either under vacuum or at atmospheric pressure. Vacuum plasmas have been well studied, and their application in polymer processing has been adopted by the microelectronics and biomedical industries [32-34]. However there are several drawbacks to operating plasmas at reduced pressure. Low pressure processing requires a vacuum apparatus, and the presence of a vessel limits the shape and size of the substrate. Operation in vacuum chambers occurs in batch mode and does not allow continuous in- line processing. The need to repeatedly pump and vent chamber adds significantly to the processing time and operating cost, and these costs grow exponentially with chamber size.

The process challenges presented by vacuum pressure can be overcome by utilizing atmospheric pressure plasmas. These include torches, dielectric barrier discharges (DBD), and radio frequency noble-gas discharges. The torch and DBD are usually operated by ionize air with high voltage power supplies at up to 10 kV [35-42]. Ionized gas in the torch forms an arc between closely spaced power and ground electrodes. Since the arc is a thermal plasma, in which the neutral temperature is many thousands of degrees [29,38,39], thermally sensitive polymer materials cannot be treated in situ. Instead, the substrates are treated by a high velocity gas stream that is blown through the arc and then onto the substrate placed downstream. In a DBD, one or both of the electrodes are covered with a dielectric barrier that prevents the arc from forming. During operation, charge buildup on the insulator surface discharges as micro-arcs that occur randomly in space and time [40-42]. The dielectric barrier discharge has long been used to process rolls of plastic film, whereby the surface is activated for printing [29,30,43]. In some instance, the DBD can also be deployed as a downstream discharge to treat 3D objects.

Atmospheric pressure noble gas plasmas driven by 13.56 or 27.12 MHz generators operate in a different way than the torch and DBD plasmas. These plasmas are weakly ionized, capacitive discharges [28,44-46]. Helium and argon breakdown at much lower voltages (150 to 600 V) in comparison to air (~2000 V). The ions and electrons uniformly fill the gas volume between the metal electrodes, and the polymer substrates are exposed to the reactive gas species downstream of the electrodes. Work by previous authors has shown that the radio frequency noble gas plasmas are effective in modifying polymer surfaces [47-52]. A more detailed discussion of different types of

plasma and their effectiveness in polymer treatment can be found in Chapter two of this manuscript.

1.5 Outline of the Thesis

The goal of this thesis is to characterize the effect of atmospheric pressure He/O₂ plasma for the activation of carbon-based materials towards improved wetting and adhesion. The first half of this work focuses on the creation of active chemical bonding sites on the surface of thermoset plastics, whereas the second half emphasizes the activation of carbon nanotube towards improved interaction with a thermoset polymer resin. Each chapter of this dissertation represents either a manuscript that has been published or one that is in preparation to be published. A review of plasma fundamentals and a comparison of commonly used plasmas for material processing is covered in Chapter 2. Chapter 3 covers the effect of atmospheric pressure He/O₂ plasma in simultaneous cleaning and activating fluorine contaminated composite surfaces. In Chapter 4, carbon nanotube sheets have been exposed to the atmospheric pressure He/O₂ plasma, and activated for dispersion in organic resin. In Chapter 5, carbon nanotube reinforced composites have been fabricated using mechanical alignment, plasma activation and chemical crosslinking. Then their mechanical, electrical and thermal properties have been examined. This method of making CNT-reinforced composites yields a material that is nearly as strong as aluminum, but at half the weight.

References

1. Manufacturing Engineering, Change-up Pitch: From metal to plastic,
<http://www.sme.org/EMMagazine/Article.aspx?id=82709&taxid=1416>.
2. F. Benyahia, A. Albedah and B.B. Bouiadjra, Bonded composite repairs of aluminum alloy 2024T3 cracked plates, in proceeding of ASME 2014 International Mechanical Engineering Congress and Exposition (2014).
3. S. Wu, *Polymer Interface and Adhesion*, 1st. ed. CRC Press, New York, NY (1982).
4. Henkel North America Technical Data Base, Adhesive for the assembly of hard to bond plastics,
http://henkelna.com/us/content_data/Hard_to_Bond_Plastics756739.pdf.
5. A. J. Kinloch, *Adhesion and adhesives*. Chapman & Hall: London (1987).
6. J.R.J. Wingfield, Treatment of composite surfaces for adhesive bonding, *International Journal of Adhesion and Adhesives*, 13, 151-156 (1993).
7. B.R.K. Blackman, A.J. Kinloch and J.F. Watts, The plasma treatment of thermoplastic fiber composites for adhesive bonding, *Composites* 25, 332-341 (1994).
8. G. Borcia, C. A. Anderson and N. M. D. Brown, The surface oxidation of selected polymers using an atmospheric pressure air dielectric barrier discharge, *Part II. Appl. Surface Sci.* 225, 186-197 (2004).
9. Freedonia, Fiber-reinforced plastic composites,
<http://www.freedoniagroup.com/industry-study/3092/fiber-reinforced-plastic-composites.htm>.

10. American Chemistry Council, North America resins industry expands in 2014 despite weakness in key export markets
<http://www.americanchemistry.com/2009-year-in-review>.
11. M. Kodama, I. Karino and J. Kobayashi, Interaction between the reinforcement and matrix in carbon-fiber-reinforced composite: Effect of forming the thin layer of polyimide resin on carbon fiber by *in situ* polymerization. *J. App. Poly. Sci.* 33, 361-373 (1987).
12. H.D. Kim, J.H. Lee, K.M. Ahn, H.S. Kim and H.S. Cha, Effect of silane activation on shear bond strength of fiber-reinforced composite post to resin cement. *J. Adv. Prosthodont* 5, 104-109 (2013).
13. C.A. Harper and E.M. Petrie, *Plastics Materials and Processes: A Concise Encyclopedia*, John Wiley & Sons Inc, Hoboken, NJ (2003).
14. S. Ebnesajjad, *Surface Treatment of Materials for Adhesive Bonding*, 2nd ed., Elsevier Inc, Waltham, MA 02451 (2014).
15. J.L. Cotter and A. Mahoon, Development of new surface pretreatments, based on alkaline hydrogen peroxide solutions, for adhesive bonding of titanium. *Int. J. Adhes. Adhes.* 2, 47-52 (1982).
16. R. J. Zaldivar, G. L. Steckel, B. A. Morgan, J. P. Nokes and H. I. Kim, Bonding optimization on composite surfaces using atmospheric plasma treatment, *J. Adhes. Sci. Technol.* 26, 381-401 (2012).
17. L.J. Hart-Smith, Adhesive-bonded joints for composites phenomenological considerations, presented at Conference on Advanced Composites Technology (1978).

18. B. Flinn, B. Clark, J. Satterwhite and P. Van Voast, In Proceedings of the SAMPE Technical Conference Baltimore, MD, 2007.
19. R. J. Zaldivar, H. I. Kim, G. L. Steckel, J. P. Nokes and B. A. Morgan, Effect of processing parameter changes on the adhesion of plasma-treated carbon fiber reinforced epoxy composites, *J. Composite Mater.* 44, 1435-1453 (2010).
20. M. Davis and D. Bond, Principles and practices of adhesive bonded structural joints and repairs. *Intl. Adhesion Adhesives* 19, 91-105 (1999).
21. P. Molitor, V. Barron, T. Young, Surface treatment of titanium for adhesive bonding to polymer composites: a review, *International Journal of Adhesion and Adhesives* 21, 129-136 (2001).
22. J.G.A. Terlingen, Introduction of functional groups at polymer surfaces by Glow discharge techniques, PhD. Thesis, University of Twente, Enschede, Netherland (1993).
23. K. Kato, Formation of 2,4-dinitrophenylhydrazones in polyethylene film treated with chromic acid mixture, *J. Appl. Poly. Sci.* 18, 3087-3094 (1974).
24. K. Kato, Investigation of high-density polyethylene film surface treated with chromic acid mixture by use of 2,4-dinitrophenylhydrazine, *J. Appl. Poly. Sci.* 20, 2451-2460 (1976).
25. S.R. Holmes-Farley and G.M. Whitesides, Reactivity of Carboxylic Acid and Ester Groups in the Functionalized Interfacial Region of "Polyethylene Carboxylic Acid" (PE-CO₂H) and Its Derivatives: Differentiation of the Functional Groups into Shallow and Deep Subsets Based on a Comparison of Contact Angle and ATR-IR Measurements, *Langmuir* 3, 62-76 (1987).

26. 18 D. Briggs, D.M. Brewis and M.B. Konieczo, X-ray photoelectron spectroscopy studies of polymer surfaces, *J. Mater. Sci.* 11, 1270-1277 (1976).
27. D.W. Dwight and W.M. Riggs, Fluoropolymer surface studies, *J. Colloid Interface Sci.* 47, 650-660 (1974).
28. A. Schutze, J.Y. Jeong, S.E. Babayan, J. Park, G.S. Selwyn and R.F. Hicks, The atmospheric-pressure plasma jet: A review and comparison to other plasma sources. *IEEE Transactions on Plasma Science* 26, 1685-1694 (1998).
29. C. Tendero.; C. Tixier, P. Tristant, P.; J. Desmaison, and P. Leprince, Atmospheric pressure plasmas: A review. *Spectrochimica Acta Part B-Atomic Spectroscopy* 61, 2-30 (2006).
30. G.S. Selwyn, H.W. Herrmann, J. Park, and I. Henins, Materials processing using an atmospheric pressure, RF-generated plasma source, *Contributions to Plasma Physics* 41, 610-619 (2001).
31. F.F. Chen, J.P. Chang, *Principles of Plasma Processing*, Plenum/Kluwer Publishers, 2002.
32. M.J. Shenton and G.C. Stevens, Surface modification of polymer surfaces: atmospheric plasma versus vacuum plasma treatments, *Journal of Physics D Applied Physics* 34, 2761-2768 (2001).
33. H. Lim, Y. Lee, S. Han, J. Cho and K.J. Kim, Surface treatment and characterization of PMMA, PHEMA, and PHPMA, *Journal of Vacuum Science & Technology A-Vacuum Surfaces and Films* 19, 1490-1496 (2001).

34. M.D. Duca, C.L. Plosceanu and T. Pop, Surface modifications of polyvinylidene fluoride (PVDF) under RF Ar plasma, *Polymer Degradation and Stability* 61, 65-72 (1998)
35. R.W. Smith, D. Wei and D. Apelian, Thermal plasma materials processing applications and opportunities. *Plasma Chemistry and Plasma Processing* 9, 135S-65 (1989).
36. G. Lucovsky, D.V. Tsu, S.S. Kim, R.J. Markunas and G.G. Fountain, Formation of thin-film dielectrics by remote plasma-enhanced chemical-vapor deposition (remote PECVD), *Applied Surface Science* 39, 33-56 (1989).
37. P. Fauchais, M. Vardelle, A. Vardelle and L. Bianchi, Plasma spray: Study of the coating generation, *Ceramics International* 22, 295-303 (1996).
38. M. Goldman and N. Goldman, *Corona Discharges In Gaseous Electronics: Vol. 1*, Hirsh, M. N.; Oakam, H. J., Eds.; Academic: New York, NY, 1978.
39. J.S. Chang, P.A. Lawless and T. Yamamoto, Corona discharge processes, *IEEE Transactions on Plasma Science*, 19, 1152-1166 (1991)
40. V.I. Gibalov and G.J. Pietsch, The development of dielectric barrier discharges in gas gaps and on surfaces. *Journal of Physics D Applied Physics* 33, 2618-2636 (2000).
41. S. Kanazawa, M. Kogoma, T. Moriwaki and S. Okazaki, Stable glow plasma at atmospheric-pressure, *Journal of Physics D Applied Physics* 21, 838- 840 (1988).
42. T. Yokoyama, M. Kogoma, T. Moriwaki and S. Okazaki, The mechanism of the stabilization of glow plasma at atmospheric-pressure, *Journal of Physics D Applied Physics* 23, 1125-1128 (1990).

43. E. Neagu, The influence of annealing time on thermally stimulated discharge current of corona-charged polymers, *Materials Letters* 21, 119-125 (1994).
44. J.Y. Jeong, J. Park, I. Henins, S.E. Babayan, V.J. Tu, G.S. Selwyn, G. Ding and R.F. Hicks, Reaction chemistry in the afterglow of an oxygen-helium, atmospheric-pressure plasma, *Journal of Physical Chemistry A* 104, 8027-8032 (2000).
45. S.E. Babayan, G. Ding and R.F. Hicks, Determination of the nitrogen atom density in the afterglow of a nitrogen and helium, nonequilibrium, atmospheric pressure plasma, *Plasma Chemistry and Plasma Processing* 21, 505-521 (2001).
46. X. Yang, S.E. Babayan and R.F. Hicks, Measurement of the fluorine atom concentration in a carbon tetrafluoride and helium atmospheric-pressure plasma, *Plasma Sources Science & Technology* 12, 484-488 (2003).
47. E. Gonzalez, M.D. Barankin, P.C. Guschl and R.F. Hicks, Remote atmospheric pressure plasma activation of the surfaces of polyethylene terephthalate and polyethylene naphthalate, *Langmuir* 24, 12636-12643 (2008).
48. E. Gonzalez, M.D. Barankin, P.C. Guschl and R.F. Hicks, Ring opening of aromatic polymers by remote atmospheric-pressure plasma, *IEEE Transactions on Plasma Science* 37, 823-831 (2009).
49. E. Gonzalez, M.D. Barankin, P.C. Guschl and R.F. Hicks, Surface activation of poly(methyl methacrylate) via remote atmospheric pressure plasma. *Plasma Processes and Polymers* 7, 482-493 (2010).
50. E. Gonzalez and R.F. Hicks, Surface analysis of polymers treated by remote atmospheric pressure plasma, *Langmuir* 26, 3710-3719 (2010).

51. T.S. Williams, H. Yu, P.C Yeh, J.M. Yang and R. F. Hicks, Atmospheric pressure plasma effects on the adhesive bonding properties of stainless steel and epoxy composites, *Journal of Composite Materials* 48, 219-233 (2014).
52. T.S. Williams, H. Yu and R.F. Hicks, Atmospheric pressure plasma activation of polymer composite for adhesive bonding, *Reviews of Adhesion and Adhesives* 1, 46-87 (2013).

Chapter 2

Atmospheric and Vacuum Plasma Treatments of Polymer Surfaces for Enhanced Adhesion in Microelectronics Packaging

Abstract

The treatment of polymer surfaces with atmospheric pressure and vacuum plasmas for enhanced adhesion is examined in this chapter. Poor wetting and adhesion can occur in microelectronic packages in key manufacturing steps such as applying epoxy molding compound to the substrate and applying epoxy underfill to the flip chip module. Low-pressure plasmas have long been utilized by the packaging industry to activate polymer surfaces prior to bonding. However, atmospheric pressure plasmas (APPs) have been developed which provide reactive species concentrations that are several thousand times higher than in vacuum plasmas, which suggests that the APP treatment may provide higher process throughput. Here, the physics and chemistry of atmospheric and vacuum discharges are examined. Then a rigorous comparison is made between these two technologies for the activation of flame-retardant 4 (FR-4) and polyimide substrates for adhesion to epoxy underfill. The data indicate that both low-pressure and atmospheric pressure plasmas are well suited for enhancing adhesion. The selection of one method over the other should be based on other considerations, such as throughput, cost, and yield.

2.1. Introduction

Semiconductor packages provide the physical structure for mounting integrated circuits (ICs) onto printed circuit boards (PCBs). Over 30 billion packages are produced each month throughout the world [1]. Semiconductor packages have three main functions: (1) to connect the electrical input and output signals between the microelectronic chip and the PCB; (2) to provide environmental isolation and protection to the ICs; and (3) to efficiently conduct heat away from the device. The diversity of semiconductor packages has increased dramatically in recent years due to the extremely high levels of integration in ICs, and to their broad range of uses in computers, tablets, mobile devices, automobiles, appliances, telecommunication systems, etc. Due to the diverse and complex nature of these products, the manufacturer is faced with many challenges in cleaning and then bonding the different components of the package together.

The traditional method of electrically connecting the IC die to the outside world is to attach wire bonds along the perimeter of the chip and bond the wires to a lead frame [2]. The wire bonds can only utilize the outer peripherals of the chip for bonding thus limiting the density of input/output signal pathway. Higher density of input/output routes may be achieved by going to a flip chip, where the electrical connections are achieved through a solder ball-grid-array (BGA) [3]. Pictures of these two options are shown in Figure 2.1. In the former case, the chips are glued to the frame, wire bonded to the leads, and finally covered with an epoxy overmold. The overmold covers the chip, wire bonds and bond pads, thereby isolating the entire package from the environment. If surfaces are not properly cleaned and activated, delamination can occur between the overmold, the chip, the metal frame, and the plastic substrate. With flip chip, an epoxy underfill must

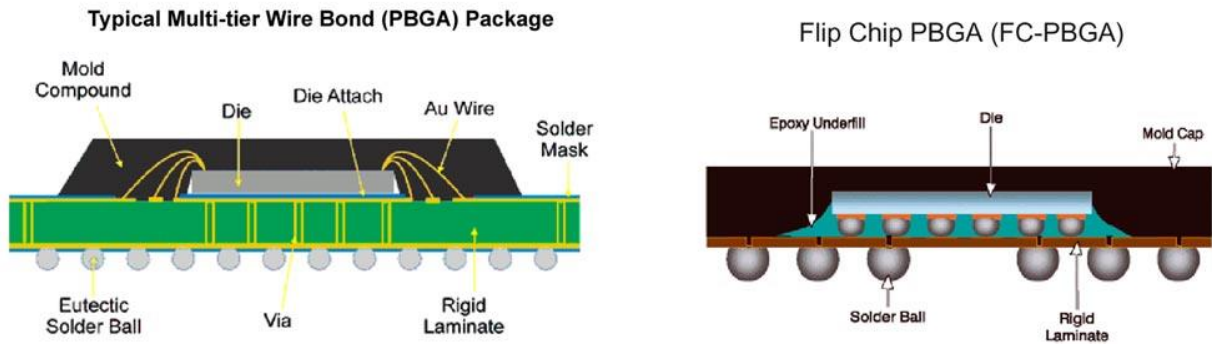


Figure 2.1. Assembled plastic ball-grid-array (PBGA) package, in which the IC die is attached to the chip holder by (a) wired bond and (b) flip chip [4].

wick into and cover the open areas around the BGA underneath the integrated circuit. Since the silicon chip and the polymer substrates have largely different coefficients of thermal expansion, unsupported solder balls are easily damaged by the shear forces generated during thermal cycling. Low-k polymers and composites used as substrates in semiconductor packages tend to have low surface energy, such that underfill dispensed on these materials may not uniformly wet the polymer surface and fill in the exposed areas around the solder balls. Plasma treatment solves this problem by oxidizing the polymer surface and making it highly wetting towards the underfill resin. [5]

Recently, electronic manufacturers have turned to 3D packaging as a means to further increase transistor density on the integrated circuit without enlarging the size of the package. Three-dimensional chip stacking technology is still a few years away from mass production [6]. Nevertheless, this approach will produce its own set of contamination and adhesion issues, and dry plasma processes will be needed more than ever to address these problems.

In this chapter, the authors examine the use of low-pressure and atmospheric-pressure plasmas for the treatment of polymer substrates used in chip packaging. The chapter begins with a review of plasma properties, with an aim to highlight the key parameters one needs to compare one type of gas discharge to another. Then we review the effects of low-pressure and atmospheric-pressure plasma treatments on polymer surfaces. Specific attention is paid to flame retardant 4 (FR-4) and polyimide (PI), since these materials are ubiquitous in semiconductor packaging. The effects of the plasma processes on the surface energy, water contact angle, roughness, composition and

adhesion strength are presented and compared among the process types. Finally, we discuss the advantages and disadvantages of the low-pressure and atmospheric-pressure plasma technologies for use in manufacturing chip packages.

2.2. Plasma Fundamentals

A plasma is an ionized gas consisting of positively and negatively charged species in which the discharge volume maintains quasi charge neutrality [7]. Thermal plasmas are close to being fully ionized, and due to the high rate of collisions between electrons and neutral species, thermal equilibrium is achieved, in which the electron temperature (T_e) approximately equals the neutral temperature (T_n). The high temperatures in thermal plasmas, e.g., arcs, make them unsuitable for materials processing. By contrast, a non-thermal plasma, or weakly ionized gas discharge, has very low concentrations of free electrons. In this case, there are insufficient collisions between the electrons and neutral species for thermal equilibrium to be achieved. The electrons are accelerated to high kinetic energies, with T_e from 1 to 2 eV (1 eV = 11,600 K), while T_n remains below 400 K. Consequently, weakly ionized plasmas are well suited for treating thermally sensitive materials, such as integrated circuits [8].

Plasmas are generated by flowing gas between powered and grounded electrodes, and by providing a sufficiently high voltage to break down the gas. Initially, when power is applied to the electrodes, the system operates in the Townsend dark region, where the voltage rises quickly with the current until ionization occurs. The breakdown voltage, V_B , depends on the gas composition, the pressure, P , and the gap spacing, d , between the electrodes [9,10]. A Paschen curve provides the characteristic dependence of V_B on $P d$

Table 2.1. Breakdown voltages (V_B), electron impact ionization thresholds (E_{iz}) and cross sections (σ_{iz}) for helium, argon, nitrogen and oxygen [7,9,12-18].

Gas	V_B DC* (kV)	V_B RF* (kV)	E_{iz} (eV)	σ_{iz}^{**} (10^{-16} cm ²)
He	0.44	0.11	24.59	0.07
Ar	0.61	0.45	15.80	1.58
N ₂	6.00	-	15.63	1.24
O ₂	6.50	-	12.07	1.13

*The DC and RF breakdown voltages were taken at 76 Torr-cm.

**Electron impact ionization cross sections were evaluated at electron temperature of 30 eV.

for a given gas [9,11]. A minimum in the breakdown voltage is observed at Pd values between 0.5 and 5.0 Torr·cm. Thus, it is more straightforward to ionize a gas inside a chamber if the pressure is reduced to between 20 and 100 mTorr. At atmospheric pressure, the noble gases, helium and argon, undergo ionization at much lower voltages than nitrogen and oxygen, as shown in Table 2.1. To break down air one must apply close to 10 kV DC or AC power!

Plasmas sustain themselves by generating free electrons in the gas through electron-impact ionization [7-9]. The surface may also contribute free electrons through thermionic emission and Auger processes [9]. Electron-impact ionization may be represented by the following equation:



Here, M is a gas molecule. The rate of this reaction depends on the electron temperature, T_e , the electron density, n_e , and the gas density, n_g . For a vacuum plasma operating at 100 mTorr, this reaction is slow enough for the gas to remain in a weakly ionized state. On the other hand, at atmospheric pressure (760 Torr) with $n_g \sim 2 \times 10^{19} \text{ cm}^{-3}$, this reaction may run away: One electron becomes two electrons, two becomes four, four becomes eight, and so forth, until the gas is fully ionized and you have an arc.

The ionization rate, r_{iz} obtained from collision theory is [11]:

$$r_{iz} = \sigma_{iz} \nu n_g n_e \quad (2)$$

Where σ_{iz} is the ionization cross section (cm^2), and ν is the mean velocity of the free electrons (cm/s). Listed in Table 2.1 are the ionization thresholds and cross sections for

helium, argon, nitrogen and oxygen [7,9,12-18]. The cross sections have been evaluated at 30 eV, which corresponds to the high energy tail in the electron energy distribution. Argon, nitrogen and oxygen have similar cross sections, such that they have fast ionization rates at atmospheric pressure. When rapid ionization is combined with breakdown voltages of 6.0 to 6.5 kV, it is easy to understand why air (containing 78% N₂ and 21% O₂) immediately transitions into an arc following ionization. Helium, on the other hand, has a much lower cross section. This fact, combined with the low breakdown voltage, makes it possible to stabilize a weakly ionized helium plasma at atmospheric pressure [11,19,20].

Non-thermal argon plasmas can be generated at atmospheric pressure as well [21-23]. They are more difficult to stabilize than the helium discharge for several reasons. The cross section is large, comparable to that of nitrogen and oxygen, yielding a fast rate of ionization. Secondly, the mass of argon is twenty times greater than helium, which reduces the electron mobility in the gas. In order to maintain a reasonable current through the argon discharge, the electron density must be pushed to a value greater than $1 \times 10^{12} \text{ cm}^{-3}$, where the plasma can transition from alpha- to gamma-mode ionization and become unstable [24,25]. Nevertheless, atmospheric pressure argon plasmas have been developed that operate at low temperatures and are well suited for semiconductor packaging operations [26].

Examples of plasma devices used to clean and activate polymer surfaces are presented in Figure 2.2. Low-pressure plasmas used in electronic packaging are usually oven-type systems (see Fig. 2a), where the substrates are stacked on trays inside the

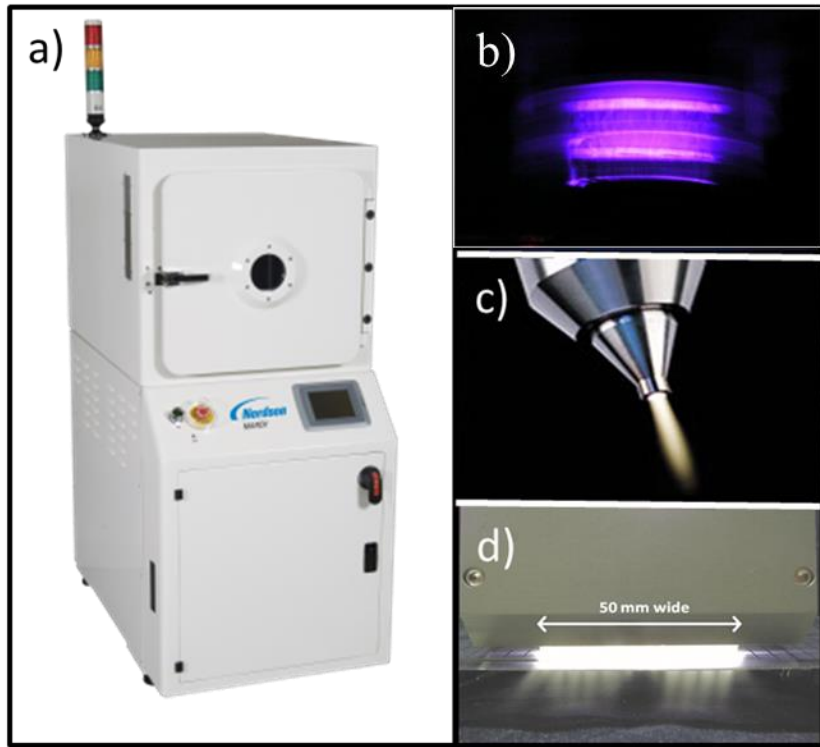


Figure 2.2. Different types of plasma systems used for surface preparation include (a) vacuum plasma, (b) dielectric barrier discharge, (c) plasma torch, and (d) atmospheric pressure, RF capacitive discharge [27-31].

discharge. These units operate at approximately 100 mTorr, and are fed with argon and other molecular gases, such as oxygen, hydrogen, nitrogen, or carbon tetrafluoride. The plasma is generated between a pair of electrodes powered by a radio-frequency (RF) generator operating at 13.56 MHz. The substrates are positioned between the electrodes, so that the surface is subjected to ion bombardment as well as to the reactive species generated by electron collisions with the molecular gases. Argon ion bombardment non-selectively sputters away material from the sample surface, which may be good or bad depending on the application. These machines can be configured for downstream treatment as well, in which argon ion bombardment is avoided. Commercial vacuum systems are available with automatic loading and unloading of substrates, and where one substrate is treated at a time on a track system. Further discussions of vacuum plasma design can be found in several books [7,8]. One important point about vacuum plasmas is that the entire substrate surface is exposed to the ionized gas.

Figures 2.2b, 2.2c, and 2.2d show the three types of atmospheric pressure plasmas used to treat materials. These include a dielectric barrier discharge (DBD), a torch, and a radio-frequency, noble gas discharge [9,11,31-35]. The DBD has long been employed to treat rolls of plastic film whereby the material is continuously passed between the electrodes [36]. In some instances, the DBD may be deployed as a downstream device, so that 3-D objects can be treated with the reactive gasses that flow out from between the electrodes. The torch and the RF noble-gas discharge are strictly downstream plasmas. Here, the ions and electrons are confined to the gap between the electrodes, and the substrate is exposed to a beam of neutral reactive species that exits from the source. A robot is used to scan the plasma beam over the substrate surface which is positioned <1

cm below the device. In contrast to vacuum plasmas, only the area on the sample surface requiring treatment is exposed to the reactive gas species.

The dielectric barrier discharge is usually operated with air. A 10 kV power supply operating at approximately 20 kHz supplies the voltage necessary to break down the gas. A dielectric barrier covers one of the electrodes, and prevents a high current arc from forming. During operation charges build up on the surface of the insulator and discharge as tiny “micro-arcs” within each cycle of the AC waveform [11,37,38]. The micro-discharges occur randomly in space and time, lasting for periods of 10 to 100 ns. Inside the micro-discharge, the electron density is high, whereas outside it is extremely low. Consequently, it is not possible to measure an average electron density and electron temperature for the entire gas volume between the electrodes. Note that substrates placed downstream of the DBD will not be treated uniformly with the plasma on the micro scale. In addition, the discharge can interact electrically with the substrate, making it difficult to treat components containing metals.

The torch is generated by forming an arc between closely spaced powered and grounded electrodes. Air is passed between the electrodes and ionized by applying 10 kV AC power. The arc is a thermal plasma in which the neutral temperature is many thousands of degrees [11,39]. Nevertheless, it is possible to blow gas through the arc at a sufficient velocity such that the overall gas temperature is low enough to treat thermally sensitive materials, such as polymers. The PlasmaflumeTM by PlasmaTreat is an example of this type of device (shown in Fig. 2c). It utilizes a rotating, cone-shaped electrode that rapidly spins the arc through the flowing gas volume, maintaining the average neutral

temperature below 700 K. Plasma streamers diluted by the flowing gas would exit from the electrode and treat objects placed a short distance below. The primary industrial application for the low-temperature plasma torch is polymer surface activation in automobile manufacturing.

Atmospheric pressure noble gas plasmas, driven with radio-frequency power at 13.56 or 27.12 MHz, operate in a different way than the DBD and torch plasmas. These plasmas, sometimes referred to as atmospheric pressure plasma jets (APPJ), are weakly ionized, capacitive discharges [11,13,21,40]. The ions and electrons uniformly fill the gas volume between the metal electrodes, with a collisional sheath forming at the boundaries to repel the electrons and maintain the plasma. The average electron density and temperature in the RF noble gas plasma have been determined to be $n_e = 10^{11}$ to 10^{12} cm^{-3} and $T_e = 1$ to 2 eV [9,11,13,21-23]. Depending on the RF power level and whether the source is water cooled or not, the neutral gas temperature ranges from 323 to 573 K. Molecular gases are fed with helium or argon at concentrations from 2.0 to 5.0 volume%. The chemistry of the plasma depends on the gas fed to the discharge. For example, O_2 , N_2 , H_2 , and CF_4 generate O, N, H, and F atoms, respectively [13,21,40,41,43]. A number of different designs of these plasma sources are available, including showerheads, small spot sources, and linear beams from 25 to 150 mm across. A 50 mm wide beam is shown in Figure 2.2d.

In Table 2.2 the properties of the vacuum plasma and the atmospheric pressure RF noble gas discharge are compared. For both of these technologies, a wealth of scientific data has been published on the plasma physics [7-9,11-23,42,44-51]. By contrast, to the

Table 2.2. Physical properties of vacuum and atmospheric pressure plasmas [7-9,11-23,40,44-50]

Plasma type	Vacuum	Atmospheric Pressure
Plasma gas	Ar/O ₂	He/O ₂ , Ar/O ₂
Breakdown voltage(kV)	0.2-0.6	0.2-0.6
Electron density (cm ⁻³)	10 ¹⁰ -10 ¹¹	10 ¹¹ -10 ¹²
Electron temperature (eV)	2	1-2
Neutral temperature (K)	<400	<600
Oxygen atom concentration (cm ⁻³)	10 ¹⁴ -10 ¹⁵	10 ¹⁶ -10 ¹⁷
Ozone concentration (cm ⁻³)	10 ¹⁰	10 ¹⁴ -10 ¹⁵

authors' knowledge, this type of data is lacking for the downstream DBD and the torch, due to the inhomogeneous nature of the processes occurring inside these discharges. The vacuum plasma considered in Table 2.2 is a parallel-plate capacitive discharge driven directly with RF power at 13.56 MHz. In the literature, this is sometimes referred to as a reactive ion etcher (RIE) [8]. The electron density in these devices ranges from 10^{10} to 10^{11} cm^{-3} , depending on the applied power [7,8,11]. The average electron temperature depends on the neutral pressure, decreasing with increasing pressure [8]. At 100 mTorr, T_e is approximately 2.0 eV. This may be compared to the atmospheric pressure plasma, where n_e varies from 10^{11} to 10^{12} cm^{-3} , and T_e is approximately 1.5 eV. Since the gas density is about 2×10^{19} cm^{-3} at atmospheric pressure, an n_e of 10^{12} cm^{-3} corresponds to 50 free electrons per billion gas particles.

Neutral reactive species are generated inside plasmas by collisions between the molecules and high energy electrons. Atomic oxygen is produced by electron impacted dissociation of molecular oxygen [7,8,40]:



Other reactive neutral species generated in argon and oxygen plasmas include metastable oxygen molecules, ($\text{O}_2(^1\Delta_g)$ and $\text{O}_2(^1\Sigma_g^+)$), and ozone [10,43-48,51]. The average concentrations of ground-state oxygen atoms and ozone in the vacuum and atmospheric pressure, RF capacitive discharges are listed in Table 2.2. Note that the concentration of oxygen atoms flowing out of the atmospheric pressure plasma is two orders of magnitude higher than the concentration of oxygen atoms inside the vacuum plasma.

The difference between the vacuum and atmospheric plasma can be understood from the rate expression for electron impact dissociation of oxygen:

$$r_{dO} = A \cdot \exp(-E_a / RT_e) [O_2] \cdot n_e \quad (4)$$

Where A is the pre-exponential factor, E_a is the activation energy, R is the ideal gas constant, and $[O_2]$ is molecular oxygen concentration. The average electron density in the atmospheric pressure discharge is about 10 times higher than in the vacuum case. In addition, the O_2 partial pressure is ~ 30 Torr for the atmospheric plasma, compared ~ 50 mTorr for vacuum plasma. Therefore, the ratio of the rates of O atom production, $r_{dO}(\text{atmospheric}) / r_{dO}(\text{vacuum}) = 10 \times 30 / 0.05 = 6,000$. The speed of cleaning and activation of a polymer surface should be directly proportional to the density of O atoms in the gas, meaning that the atmospheric plasma is an inherently faster process. Although the huge difference in reactive species densities is moderated somewhat by the fact that in the atmospheric pressure discharge, these species are focused in a beam with a thickness of about 1 cm when it comes in contact with the substrate. By contrast, the vacuum plasma contacts the entire sample surface at once.

Shown in Figure 2.3 are the concentrations of the reactive species as a function of distance downstream of the atmospheric pressure, radio-frequency helium/oxygen plasma. These concentration profiles were predicted from a numerical model of the process [51]. At 5 mm from the source exit, the concentrations are as follows: $4 \times 10^{16} \text{ cm}^{-3}$ O atoms, $6 \times 10^{16} \text{ cm}^{-3}$ $O_2(^1\Delta_g)$, $< 1 \times 10^{13} \text{ cm}^{-3}$ $O_2(^1\Sigma_g^+)$, and $8 \times 10^{15} \text{ cm}^{-3}$ O_3 . Titration of the atomic oxygen with nitric oxide has confirmed that the O atom concentration at the exit is in the range of 10^{16} to 10^{17} cm^{-3} , or on the order of 0.1 to 1.0 volume% of the gas flow [21]. On

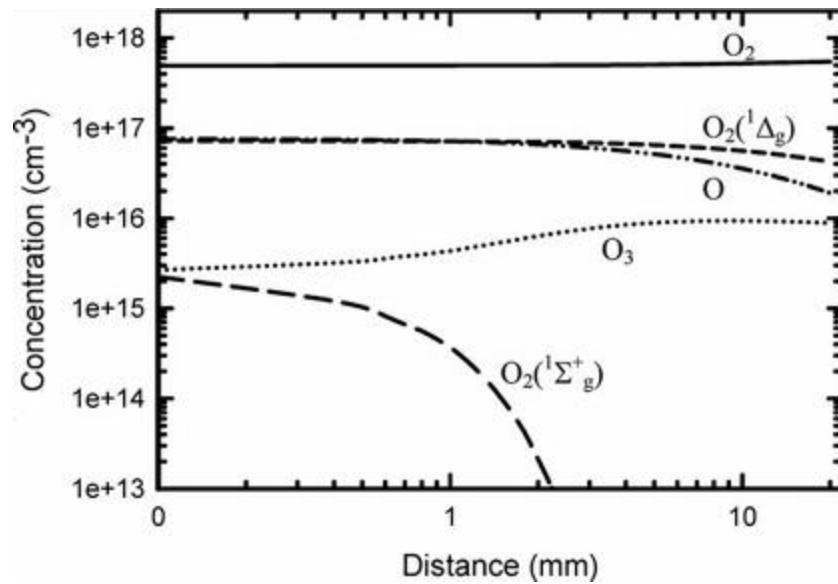


Figure 2.3. Concentration of reactive species as a function of distance from the exit of the atmospheric pressure, RF, He/O₂, capacitive discharge [51].

the other hand, direct measurement of the ozone concentration in the afterglow yields a value of $8 \times 10^{14} \text{ cm}^{-3}$, or 40 parts per million.

2.3. Survey of Vacuum Plasma Treatment of Polymers

The most common polymers used in electronic packaging are flame retardant 4 (FR-4), solder mask, and polyimide. Flame retardant 4 is a glass-reinforced epoxy composite, which has good strength to weight ratio, near zero water absorption, and is electrically insulating. Its mechanical strength and electrical insulation in both dry and humid conditions makes FR-4 the preferred material for printed circuit boards (PCBs) [52]. Solder masks are polymers with low surface energy, and their function is to protect metal lines on the substrate during solder deposition. Solder mask materials include thermally cured epoxies, UV curable acrylate, and polyimide tape [53]. Polyimide has a low dielectric constant combined with excellent, chemical, mechanical and thermal stability [54]. These properties make it an excellent substrate for flexible electronic products.

The effect of vacuum plasma treatment on the water contact angle (WCA) and surface roughness of FR-4, solder mask and polyimide is presented in Table 2.3 [6]. Noh and coworkers [55] exposed the uncoated surface of FR-4 to an Ar/O₂ plasma for 300 s, after which they found that the water contact angle dropped from 50° to <10°. Sham et al. [56] observed a drop in the WCA of solder mask from 80° to 40° following a 600 s immersion in the argon plasma. In this case, surface activation most likely resulted from Ar⁺ ion bombardment. Getty and Zhao [57] treated solder mask and polyimide with

Table 2.3. Water contact angle (WCA) and surface roughness of FR-4, solder mask, and polyimide before and after vacuum plasma treatment.

Material	Plasma gas	Time (s)	WCA (°)		Surface Roughness (nm)		Ref.
			Before	After	Before	After	
FR-4	Ar/O ₂	300	50	<10	3.8	0.1	[55]
Solder mask	Ar	600	80	40	56	70	[56]
Solder mask	Ar	---	82	74	---	---	[57]
Solder mask	N ₂	---	82	74	---	---	[57]
Solder mask	O ₂	---	82	30	---	---	[57]
Polyimide	Ar	---	60	52	---	---	[57]
Polyimide	N ₂	---	60	46	---	---	[57]
Polyimide	O ₂	---	60	5	---	---	[57]
Polyimide	He/O ₂	50	70	20	---	---	[58]
Polyimide	Ar	300	---	---	0.4	17.6	[60]
Polyimide	NH ₃	300	---	---	0.4	2.9	[60]
Polyimide	O ₂	600	---	---	50	200	[61]
Polyimide	O ₂ /SF ₆	600	---	---	50	400	[61]

remote argon, nitrogen and oxygen plasmas for an unspecified period of time. By operating in a remote fashion, the substrate was not subjected to ion bombardment. These authors found that exposure to the argon and nitrogen plasmas decreased the water contact angle only by a small amount, whereas the oxygen plasma yielded a large decline. In the latter case, the decrease in WCA was from 82° to 30° for the solder mask, and 60° to 5° for the polyimide. Egitto and coworkers [58] found that exposure of polyimide to a direct He/O₂ plasma for 50 s reduced the WCA from 70° to 20°. In summary, the surface energy of FR-4, solder mask, and polyimide may be significantly increased by treatment with low-pressure oxygen plasmas, which should be beneficial towards enhancing the wetting by the adhesives [59].

No consistent trend in surface roughness with vacuum plasma exposure was found when reviewing the literature. As seen in Table 2.3, Noh et al. [55] recorded a drop in the roughness of FR-4 from 3.8 to 0.1 nm after Ar/O₂ plasma treatment. Sham et al. [56] observed a slight increase in the root-mean-square (rms) roughness of solder mask, from 56 to 70 nm, after immersion in the argon plasma. Bhusari et al. [60] and Uddin et al. [61] found that the treatment of polyimide with direct argon, ammonia or oxygen plasmas yielded a 4 to 44 times increase in surface roughness. The largest increase in roughness was observed when the polyimide was exposed to the argon plasma. In this case, the change in surface roughness is mainly due to physical sputtering, and not to a chemical etching process.

The effect of vacuum plasma treatment on the surface composition of FR-4, solder mask and polyimide has been examined by X-ray photoelectron spectroscopy

(XPS). The changes observed in the atomic ratio of carbon to oxygen on the polymer surfaces are shown in Table 2.4. In all cases, a significant drop in the C/O ratio is observed, regardless of whether the material is treated with oxygen, argon, argon/O₂ or ammonia plasmas. Noh et al. [55] reported that exposure of the FR-4 surface to the Ar/O₂ plasma increased the fraction of hydroxyls, carbonyls and highly oxidized carbon atoms (which they assigned to C-O₃) by 2%, 8%, and 18%, respectively. Sham et al. [56] found that the solder mask was oxidized by sputtering with argon ions. It is speculated that the argon sputtering of solder mask leaves dangling carbon bonds on the substrate surface, which can react with oxygen or water molecules in air to form oxidized carbon groups. Analysis of the XPS spectrum indicated that the concentrations of carbonyls and carboxylic acids on the surface increased by 7% and 8%. Bhusari et al. [60] observed a similar effect of argon-ion sputtering on polyimide: the C/O ratio declined from 5.6 to 2.8, while at the same time, the concentration of surface hydroxyl and carbonyl groups increased by 6% to 7%.

The adhesive bond strength between epoxy underfill and FR-4, solder mask and polyimide, before and after vacuum plasma treatment, is shown in Table 2.5. For rigid substrates such as FR-4, their adhesion strength to epoxy underfill is measured using either the single lap shear test (ASTM D1002/ASTM D3163) or the button shear test (SEMI G69-0996) [65-67]. Exposure of FR-4 to an Ar/O₂ plasma increases the lap-shear strength from 8 to 12 MPa. In addition, the failure mode of the specimen changed from adhesional failure at the underfill/FR-4 interface, to cohesive failure within the underfill itself [55]. The Ar or O₂ plasma treatments of solder mask also yielded excellent results. Zhao et al. [64] observed an increase in lap-shear strength between the solder mask and

Table 2.4. Carbon-to-oxygen atom ratio on the surface of FR-4, soldermask, and polyimide before and after vacuum plasma treatment in different plasma gases.

Material	Plasma type	Plasma gas	C/O Ratio		Ref.
			Before	After	
FR-4	Direct	Ar/O ₂	2.5	0.9	[55]
Solder mask	Direct	Ar	2.4	1.5	[56]
Solder mask	Remote	O ₂	5.6	3.7	[62]
Polyimide	Remote	O ₂	4.5	2.1	[63]
Polyimide	Direct	Ar	5.6	2.8	[60]
Polyimide	Direct	NH ₃	5.6	2.6	[60]

Table 2.5. Effect of vacuum plasma treatment on adhesion between epoxy underfill and three polymer substrates.

Substrate	Plasma gas	Test	Bond Strength*		Failure Mode		Ref.
			Before	After	Before	After	
FR-4	Ar/O ₂	L-Shear ^a	8	12	adhesional	cohesive	[55]
Solder mask	O ₂	L-Shear	16	31	adhesional	cohesive	[64]
Solder mask	O ₂	L-Shear	16	33	adhesional	cohesive	[64]
Solder mask	Ar	L-Shear	16	36	adhesional	cohesive	[64]
Solder mask	Ar	D-Shear ^b	8	12	adhesional **	cohesive ***	[56]
Polyimide	O ₂	T-Peel	400	1,100	adhesional	cohesive	[64]
Polyimide	O ₂	T-Peel	400	900	adhesional	cohesive	[64]
Polyimide	Ar	T-Peel	400	900	adhesional	cohesive	[64]
Polyimide	Ar	90° Peel	600	600	adhesional	---	[61]
Polyimide	O ₂	90° Peel	600	900	adhesional	---	[61]
Polyimide	O ₂ /SF ₆	90° Peel	600	1,400	adhesional	cohesive	[61]

^aL-shear is lap shear.

^bD-shear is die shear.

*The strength units are MPa for the shear tests, and N/m for the peel tests.

**Failure occurred at the interface between epoxy underfill and FR-4, soldermask, or polyimide.

***Failure occurred cohesively within the solder mask instead of within the epoxy resin.

the underfill from 16 MPa to between 31 and 36 MPa, and a switch in failure mode from adhesional to cohesive within the underfill.

The bond strength between polyimide and epoxy underfill has been examined by T-peel and 90° peel tests, as shown in Table 2.5. The T-peel and 90° peel tests were performed in accordance to ASTM standards D1876 and D6862, respectively [68,69]. Zhao et al. [64] observed an increase in the polyimide T-peel strength from 400 N/m to between 900 and 1,100 N/m following exposure to a vacuum plasma filled with Ar or O₂. They also noted that the plasma process changed the failure mode from adhesional to cohesive. Uddin et al. [61] activated polyimide films with Ar, O₂, and O₂/SF₆ plasmas for up to 60 minutes. After processing, the samples were bonded to dies with underfill, and the bond strength was measured using a 90° peel test. Initially, the polyimide was separated from the chip at a force of 600 N/m. Exposure to the argon plasma did not improve the adhesion. Treatment with O₂ and O₂/SF₆ plasmas increased the peel strength to 900 and 1,400 N/m, respectively. The authors proposed that the oxyfluoride species were much more reactive and better able to oxidize the polymer surface, thereby resulting in higher bond strength.

2.4. Survey of Atmospheric Pressure Plasma Treatment of Polymers

Atmospheric pressure plasma treatment is an emerging technology that is not yet widely employed in semiconductor packaging. Nonetheless, this technology has gained acceptance in other industries where it is routinely used to activate polymer surfaces for adhesion. Results obtained on common plastic materials will be examined first, after which original data will be presented on atmospheric plasma processing of FR-4 and

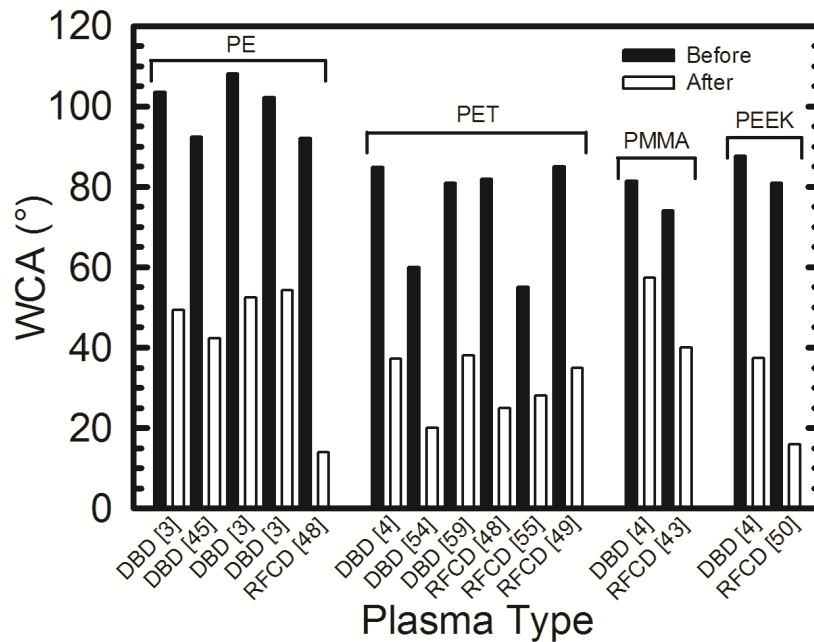


Figure 2.4. Water contact angles (WCA) on polyethylene (PE), poly(ethylene terephthalate) (PET), poly(methyl methacrylate) (PMMA), and poly(ether ether ketone) (PEEK) before and after activation with dielectric barrier discharge (DBD) or radio-frequency capacitive discharge (RFCD) [51,70-77].

polyimide. In Figure 2.4, water contact angle measurements are shown for the activation of polyethylene (PE), poly(ethylene terephthalate) (PET), poly(methyl methacrylate) (PMMA), and poly(ether ether ketone) (PEEK) [30]. Two types of plasma devices are compared, the dielectric barrier discharge (DBD), and the RF capacitive discharge (RFCD) fed with noble gases. It can be seen that treatment of PE with the DBD decreases the WCA from $100^{\circ}\pm 10^{\circ}$ to $45^{\circ}\pm 5^{\circ}$. Treatment with the RFCD is significantly better, where the final WCA is 10° . The change in water contact angle on PET is roughly the same after exposure to the DBD or the RFCD. In both cases, the WCA is reduced from about 80° to between 20° and 40° . For both PMMA and PEEK, the RFCD shows a more effective treatment of the polymer surface than the DBD. The WCA values for PMMA and PEEK after exposure to the atmospheric pressure RF capacitive discharge are 40° and 15° , respectively.

Table 2.6 shows the surface oxygen concentration and carbon-to-oxygen ratio for polyethylene, polypropylene and poly(ethylene terephthalate) before and after treatment with the atmospheric pressure plasmas. The surface composition has been determined by XPS. Three types of plasmas are compared in the Table, the torch, DBD and RFCD. One sees that the oxygen atomic percentage on the surface significantly increases after exposure to the air, He/O₂, and Ar/O₂ plasmas, with values ranging from 8.7% for treatment of PP with the torch to 40% for treatment of PET with the DBD. It is likely that there are some differences in performance of the three types of plasma sources. For example, on polypropylene, the torch fed with air reduced the C/O ratio to 10.5, whereas the RFCD fed with argon/oxygen reduced the C/O ratio to 1.9. Unfortunately in these

Table 2.6. The effect of atmospheric plasma activation on the surface composition of polymers.

Polymers	Plasma type	Plasma gas	O atomic %		C/O ratio		Ref.
			Before	After	Before	After	
PE	Torch	Air	2.0	24.4	50.0	3.1	[78]
PP	Torch	Air	3.1	8.7	33.0	10.5	[78]
PET	Torch	Air	15.2	32.4	5.6	2.1	[78]
PE	DBD	He/O ₂	6.6	21.3	14.0	3.7	[72]
PET	DBD	Air	28.6	40.0	2.5	1.4	[79]
PET	DBD	Air	29.1	35.5	2.4	1.8	[80]
PP	RFC	Ar/O ₂	6.8	33.6	14.0	1.9	[81]
PET	RFC	He/O ₂	25.0	37.0	3.0	1.7	[74]

Table 2.7. Surface energy and lap-shear strength of epoxy bonded polymers before and after atmospheric pressure plasma activation.

Polymers	Plasma type	Plasma gas	Surface energy (mJ/m ²)		Lap shear strength (MPa)		Ref.
			Before	After	Before	After	
PE	Torch	Air	28	60	0.3	4.6	[78]
PP	Torch	Air	27	52	0.3	3.7	[78]
PET	Torch	Air	35	63	1.6	4.8	[78]
PEEK	DBD	Air	51	73	0.5	5.6	[83]
PET	RFC	He/O ₂	44	55	3.8	11.2	[74]
PEEK	RFC	He/O ₂	50	75	1.0	3.7	[75]

studies, data are lacking on the time it took to activate each of the polymers with the different plasma sources.

In Table 2.7, a summary is presented of the changes in surface energy and lap-shear strength of different polymers following exposure to the atmospheric pressure plasmas [59,74,75,78,82]. The torch, DBD and RFCD are all found to be effective at preparing the plastics for bonding. Surface energies after activation are in the range of 52 to 75 mJ/m². In addition, a large jump in adhesion is observed, with lap-shear strengths increasing by three to fifteen times. Noeske et al. [78], Iqbal et al. [82], and Gonzalez et al. [74,75] have noted that untreated polymers exhibit interfacial failure at the adhesive-substrate interface, whereas treated polymers exhibit cohesive failure within the adhesive itself. One may conclude that atmospheric pressure plasmas are an effective tool for the surface preparation of polymers for bonding.

2.5. Atmospheric Pressure Plasma Activation of Polymer Materials Relevant to Microelectronics

2.5.1. FR-4 Activation

Surface preparation of FR-4 by the atmospheric pressure RF capacitive discharge is considered in this section. The polymer surfaces were activated using a 50-mm linear beam plasma (Surfx Technologies, Atomflo™ 400) operated at 150 W (27.12 MHz), 0.5 L/min oxygen, 30.0 L/min helium, 5.0 mm source-to-sample distance, and 20 mm/s scan speed. After exposure to the plasma, the samples were characterized by water contact angle, atomic force microscopy, X-ray photoelectron spectroscopy, and single lap-shear tests (ASTM D1002/D3163) [65,66].

The dependence of the WCA on exposure time for FR-4 is shown in Figure 2.5. Initially, the contact angle of FR-4 was $92^{\circ} \pm 3^{\circ}$, which after a 0.1 s treatment fell to 35° . From 0.1 to 15.0 seconds of exposure to the He/O₂ plasma, the WCA of FR-4 remained close to 35° , whereas from 15.0 to 60.0 seconds, it dropped gradually to 10° . The trend in water contact angle with plasma exposure time may be fitted with two exponential decay equations, with each equation of the form:

$$WCA(t) = WCA_f + [WCA_i - WCA_f] \cdot \exp(-k_{wca} t) \quad (5)$$

Here, WCA_f is the water contact angle at long times, WCA_i is the initial water contact angle, k_{wca} is the rate constant (s^{-1}), and t is exposure time (s). The fast and slow rate constants, k_{wca1} and k_{wca2} , obtained by fitting Eq. (5) to the data in Figure 2.5 are $17.9 \pm 3.7 s^{-1}$ and $0.08 \pm 0.05 s^{-1}$, respectively. The exponential decay function can be explained by a Langmuir adsorption model, whereby reactive oxygen species in the afterglow of the atmospheric plasma bind with vacant sites on the polymer surface [74,83]. With regard to the two-stage decay, it may be hypothesized that there are two types of vacant sites on the polymer surface, each with a different adsorption rate. The fast rate could be adding functional groups along the polymer chain, whereas the slow rate could cause an etching reaction.

Table 2.8 shows the surface roughness of FR-4 as measured by atomic force microscopy (AFM). The specimens were treated with the He/O₂ RF discharge for 0.0, 0.5, 10.0, 30.0, and 60.0 s. The root mean square (RMS) roughness of the control sample was 60 ± 24 nm. One sees that the roughness values oscillated up and down throughout the duration of treatment, ranging from a low of 17 nm to a high of 54 nm. No trend can

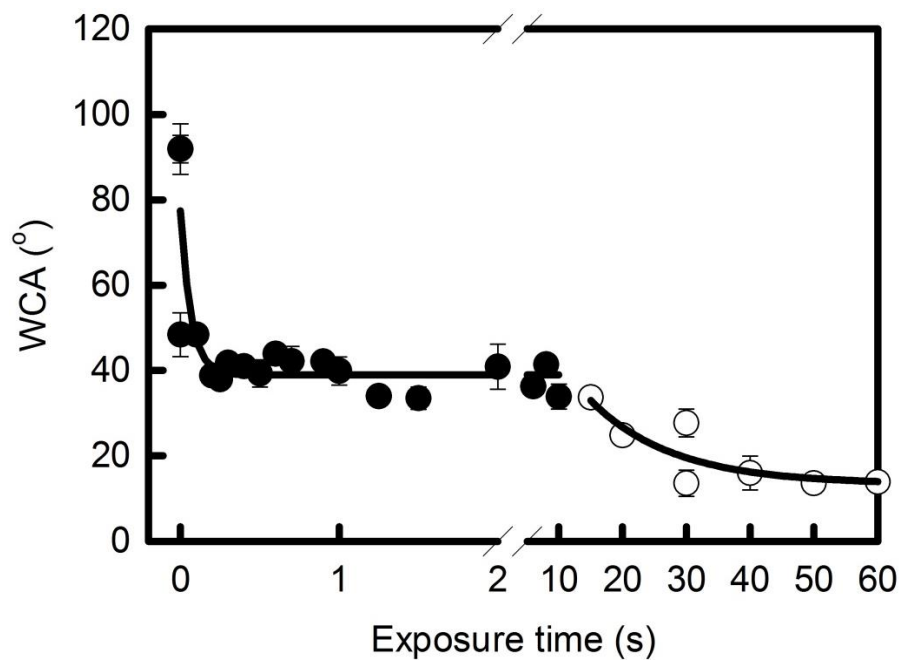


Figure 2.5. Dependence of the water contact angle (WCA) of FR-4 on exposure time to the atmospheric pressure He/O₂ plasma. Solid dots (●) are data collected when WCA drops sharply with plasma exposure and open circles (○) are data collected when WCA becomes less sensitive to increasing plasma exposure

Table 2.8. Dependence of FR-4 surface roughness on exposure time to the atmospheric pressure He/O₂ plasma.

Exposure Time (s)	Roughness (nm)
0.0	60 ± 24
0.5	17 ± 5
10.0	22 ± 11
30.0	35 ± 14
60.0	54 ± 28

be observed between the roughness and the two-stage exponential decay in water contact angle. The changes are most likely due to the evolution of the surface morphology as the polymer was slowly etched by the He/O₂ plasma.

The change in surface composition of FR-4 during plasma activation has been studied using x-ray photoelectron spectroscopy (XPS). The composition of FR-4 can be calculated using the molecular structure of bisphenol-A-diglycidyl ether (DGEBA), which is the primary resin component in FR-4 [84,85]. In this molecule, the atomic percentages of carbon and oxygen are 82 and 18 %, respectively. Based on the areas under the carbon 1s and oxygen 1s emission peaks, the atomic percentages of carbon and oxygen measured for the untreated (control) sample are 85 and 15 %, respectively. These values agree with the theoretical composition of the FR-4 resin.

Shown in Figure 2.6 is the atomic percentage of oxygen on the FR-4 surface as a function of plasma exposure time. The O atomic% rose rapidly from 0.0 to 2.0 s, and then eventually came to a plateau at 5.0 s. The fully oxidized surface exhibited an oxygen atom concentration of 22%. The trend in the data seen in Figure 2.6 may be fitted with the following equation:

$$O(t) = O_f + [O_i - O_f] \cdot [\exp(-k_O t)] \quad (6)$$

where O_i is the oxygen atom% on the control specimen, O_f is the oxygen atom% at long times, and k_O is the first-order rate constant for oxidation of the polymer. In this case, k_O is calculated to be $2.5 \pm 1.2 \text{ s}^{-1}$, which is a factor of four slower than the initial rate constant for the decay in water contact angle, k_{wca1} .

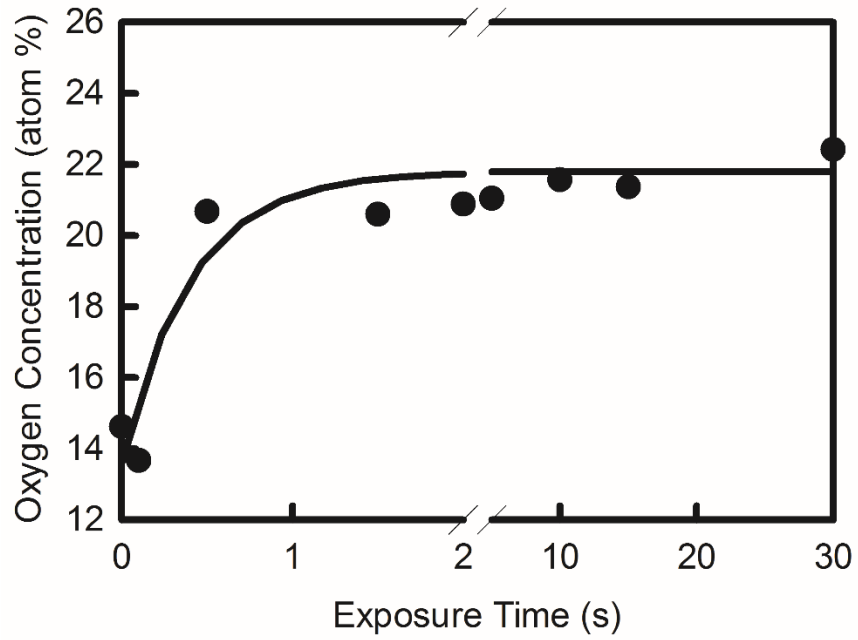


Figure 2.6. The oxygen atomic% on the FR-4 surface as a function of exposure time to the atmospheric pressure He/O₂ plasma.

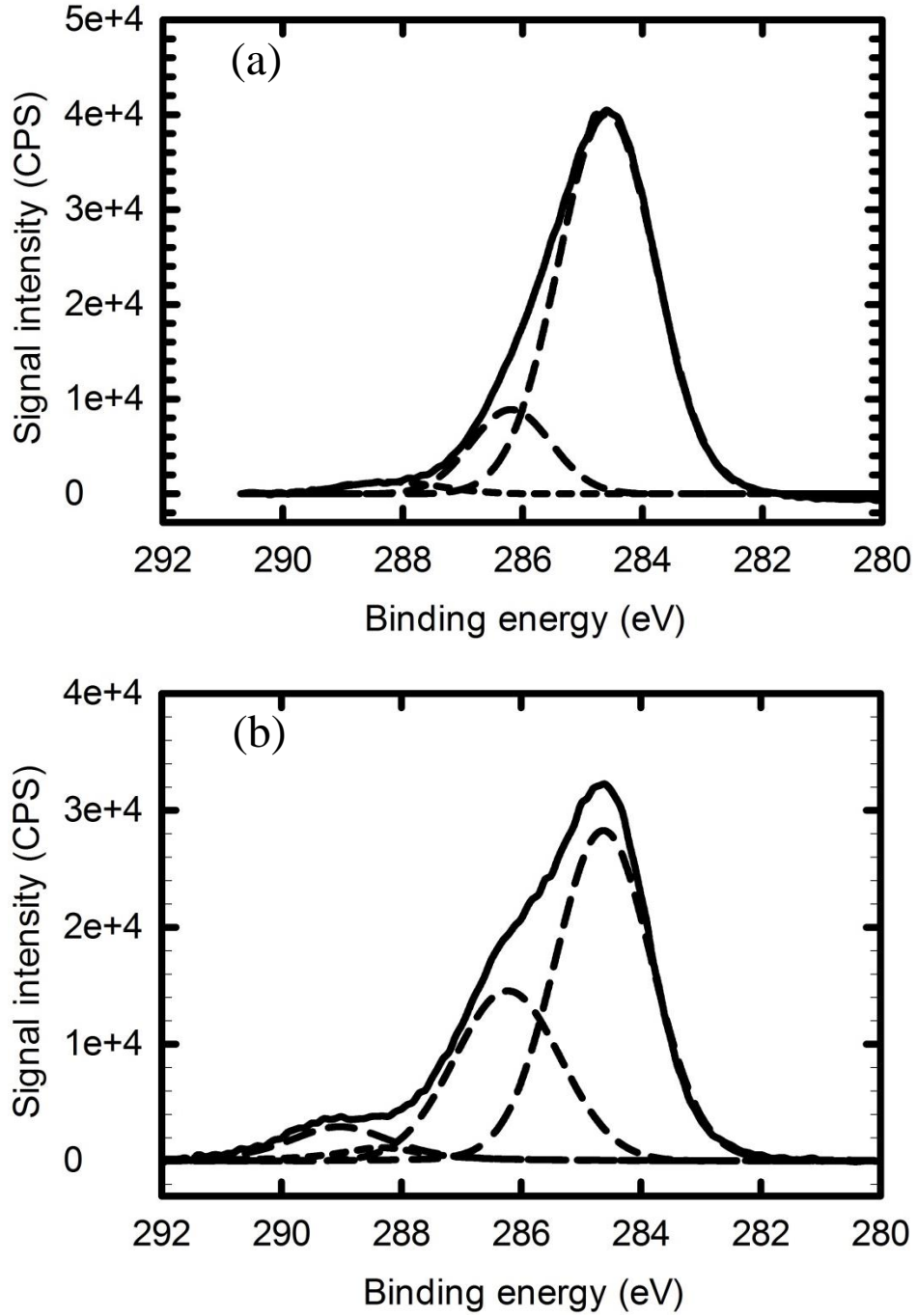


Figure 2.7. Carbon 1s spectra for FR-4: (a) before plasma treatment, and (b) after 10 s exposure to the atmospheric pressure He/O₂ plasma.

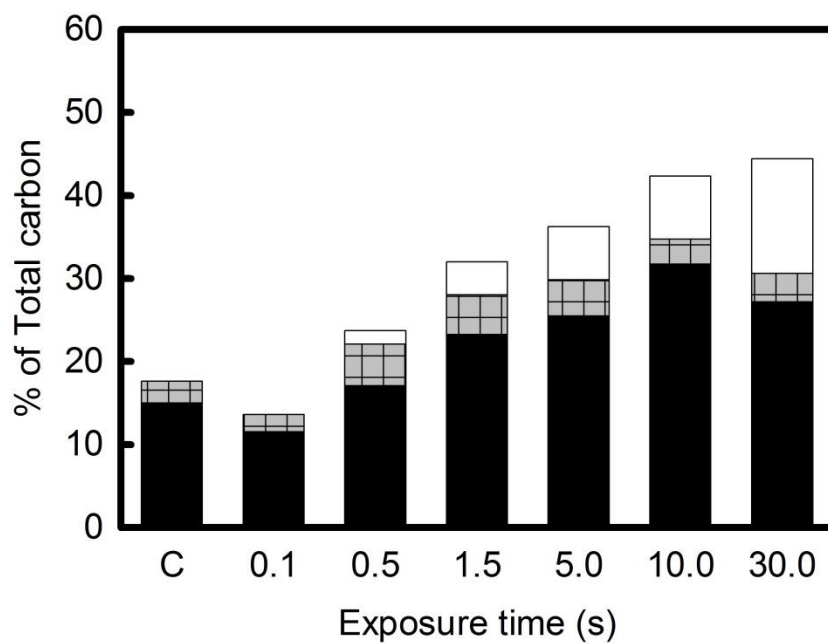


Figure 2.8. Distribution of oxidized carbon groups on FR-4 surface before and after the atmospheric pressure He/O₂ plasma treatment. ■ represents the C-O groups, ▨ represents the C=O groups, and □ represents the O=C-O groups.

The carbon 1s spectra of FR-4 before and after He/O₂ plasma activation are presented in Figure 2.7. The control spectrum has been deconvoluted into three peaks centered at 284.6, 286.2, and 288.3 eV. These peaks are assigned to aromatic/aliphatic carbon atoms (C-C and C=C bonds), hydroxyl carbon atoms (C-O bonds), and carbonyl carbon atoms (C=O bonds) [86-89]. After plasma activation, a new peak appeared at 289.0 eV, which is assigned to carboxylic acid groups (O-C=O bonds).

Shown in Figure 2.8 is the distribution of carbon oxidation states on FR-4 as a function of He/O₂ plasma treatment time. Initially, the oxygen bound to the polymer surface consisted of ~85% hydroxyl groups and 15% carbonyl groups. During the initial 0.5 s of exposure to the plasma, the fraction of carbonyl groups increased slightly, and in addition, a significant amount of carboxylic acids was generated on the surface. As the plasma exposure time increased from 0.5 to 30.0 s, the amounts of carboxylic acid and hydroxyl groups on the surface increased at the expense of the carbonyl groups. The average distribution of these species on the surface between 1.5 and 30.0 s of exposures was 69% C-O, 10% C=O and 21% O-C=O.

The effect of plasma treatment on the bond strength between FR-4 and epoxy underfill was examined using a single lap shear test (ASTM D1002/ASTM D3163) [65,66]. The specimens were bonded using Hysol FP4549 underfill resin, and cured at 160 °C and 68.9 MPa pressure. The thickness of the underfill was controlled to 300 μm by using a stainless steel spacer during the cure cycle.

Figure 2.9 illustrates how the lap shear strength τ of adhesively bonded FR-4 depends on the treatment time with the atmospheric pressure RF capacitive discharge

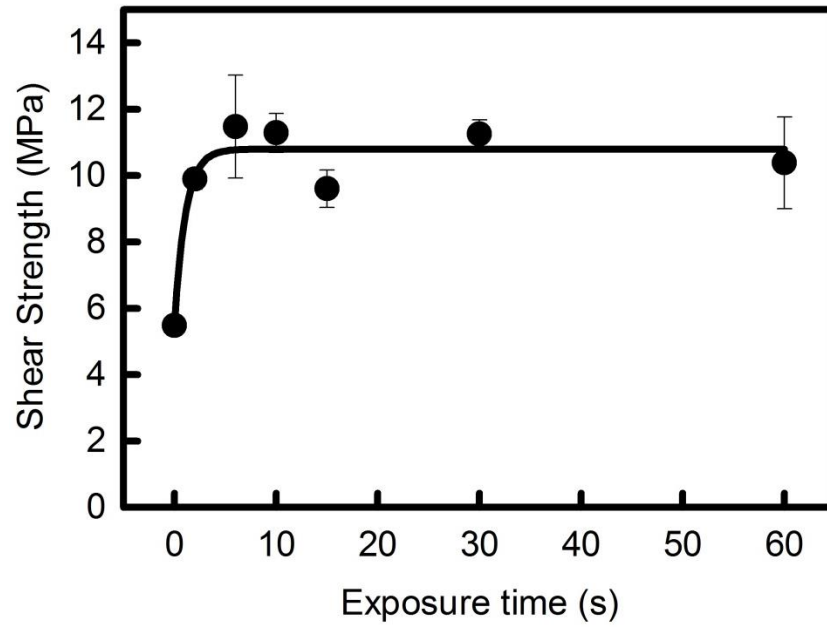


Figure 2.9. Dependence of the lap-shear strength of epoxy bonded FR-4 on exposure time to the atmospheric pressure He/O₂ plasma.

using He/O₂. Without any surface preparation, the shear strength of the FR-4/underfill assembly was approximately 5.4 MPa, which is comparable to the control value reported by Noh et al. [55]. From 0.0 to 5.0 s of plasma exposure, the shear strength increased by over twofold to 11.5 MPa. Further exposure to the plasma, out to 60s, did not significantly change the strength of the joint.

The lap-shear strength data presented in Figure 2.9 can be fitted using the following equation:

$$\tau(t) = \tau_f + [\tau_i - \tau_f] \cdot [\exp(-k_\tau t)] \quad (7)$$

where τ_i is the shear strength of the control specimen, τ_f is the maximum shear strength, and k_τ is the first-order rate constant for the change in shear strength with exposure time to the plasma. The rate constant obtained by the best fit of Eq. (7) to the data in Figure 2.9 is $k_\tau = 0.9 \pm 0.5 \text{ s}^{-1}$.

The rate constants measured for the changes in WCA, surface oxygen concentration, and lap-shear strength over time are summarized in Table 2.9. One sees that the rate constant of wetting the surface, k_{wcal} , is much higher than the rate constant of oxidation or strength enhancement. On the other hand, the rate of strength enhancement is one-third of the rate of surface oxidation. These results may be understood as follows: wetting does not require as many active sites on the polymer surface as does adhesion. The water droplet can spread out flat so long as there are enough hydroxyl, carbonyl or other oxygen-containing functional groups to interact with the macro-scale droplet. Adhesion, on the other hand, depends on the “quality and quantity” of the chemical bonds formed between the surface and the adhesive, with bonding occurring at the nanoscale

Table 2.9. First-order rate constants determined for FR-4 surface property changes with plasma treatment.

Property	Rate constant	Value (s ⁻¹)
WCA fast ^a	k_{wca1}	17.9 ± 3.7
WCA slow ^b	k_{wca2}	0.08 ± 0.05
Surface oxygen	k_O	2.5 ± 1.2
Lap-shear strength	k_τ	0.9 ± 0.5

^aFrom 0-10 s of atmospheric pressure He/O₂ plasma treatment, water contact angle drops rapidly with plasma exposure

^bBeyond 10 s of atmospheric pressure He/O₂ plasma treatment, water contact angle drops more slowly with increasing plasma exposure.

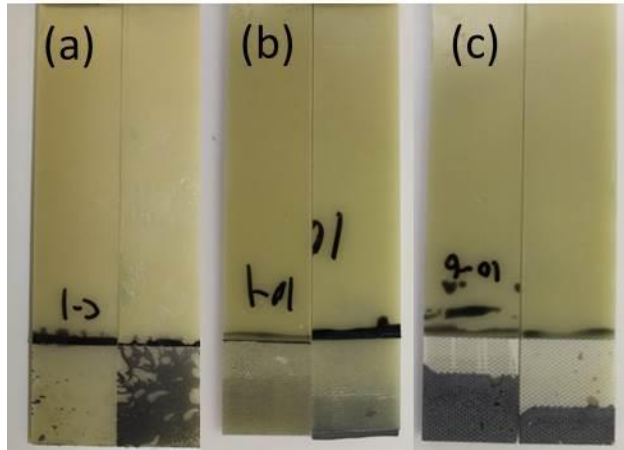


Figure 2.10. The lap shear fracture surface of FR-4 coupons is located (a) at the polymer/adhesive interface for FR-4 not treated by atmospheric pressure He/O₂ plasma, (b) within the adhesive for FR-4 treated by the plasma treatment, and (c) within the substrate laminate for FR-4 treated by the plasma and bonded with thinner adhesive thickness.

[90]. The lower rate constant recorded for strength enhancement relative to polymer oxidation may be due to the nature of the functional groups generated on the surface. For example, the carboxylic acid groups, which are known to form strong bonds with epoxy adhesive, formed less quickly than the hydroxyls and carbonyls under the He/O₂ plasma [51,74,75,91-94].

The fracture surfaces of FR-4 specimens have been examined visually after the lap-shear test in order to determine the failure mode. Pictures of the fracture surfaces of the control and plasma treated samples are presented in Figure 2.10. The control sample (a) exhibited 100% adhesional failure, exposing large areas of bare FR-4 surface after the test. By contrast, the sample activated by the He/O₂ plasma exhibited 100 % cohesive failure in the epoxy underfill, as can be seen by the uniform gray coating on both coupons in (b). The bonded regions of the control and plasma treated samples were further inspected using an optical microscope at 50 X magnification. The microscope image confirms the failure modes stated above. Figure 2.10(c) shows the fracture surface of a plasma treated FR-4 sample in which the thickness of the underfill was reduced from 300 to 200 μm . In this case, the shear plane was located within one of the FR-4 laminates. The lap-shear strength recorded was 12 MPa. This is in agreement with the theory that lower adhesive thickness yields higher bond strength [95,96]. In summary, a few seconds treatment with the atmospheric He/O₂ plasma yields FR-4 surfaces that are optimally activated for bonding to epoxy adhesives (underfill and overmold).

2.5.2. Polyimide Activation

The polyimide was treated with the atmospheric pressure RF capacitive discharge using the same conditions as described above for FR-4: 50-mm wide plasma beam operated at 150 W, 0.5 L/min oxygen, 30.0 L/min helium, 5.0 mm source-to-sample distance, and 20 mm/s scan speed. Shown in Figure 2.11 is the dependence of the water contact angle of the polyimide on plasma exposure time. Initially, the WCA was $64^{\circ} \pm 8^{\circ}$. Within 0.2 s plasma exposure, the WCA fell rapidly to 20° , and then remained constant at 20° from 0.2 to 1.5 s. At longer exposure times, it decayed slowly to below 10° . The fast and slow decay curves were fitted with the model given by Equation (5) above. The best fit yielded values for k_{wca1} and k_{wca2} were 12.8 ± 3.0 and $0.2 \pm 0.04 \text{ s}^{-1}$, respectively. These first order rate constants are similar to those recorded for the FR-4.

Table 2.10 lists the surface roughness of polyimide samples measured by atomic force microscopy after 0.0, 0.5, 10.0, 30.0, and 60.0 seconds of atmospheric He/O₂ plasma treatment. In this case, the surface roughness of polyimide increased from 7 ± 3 nm to 18 ± 8 nm after 0.5 s of treatment. The roughness value remained stable out to 10.0 seconds, but then further increased to 25 nm at 30.0 and 60.0 s of processing. The change in roughness with time is most likely due to polymer etching.

The change in surface composition of polyimide during plasma activation was characterized by XPS. In this polymer, the atomic percentages of carbon, oxygen and nitrogen are 76%, 17% and 7%, respectively. From the areas under the C 1s, O 1s and N 1s photoemission peaks, the atomic percentages of carbon, oxygen and nitrogen found on the untreated, control were 74%, 21% and 5%, respectively. This demonstrates good

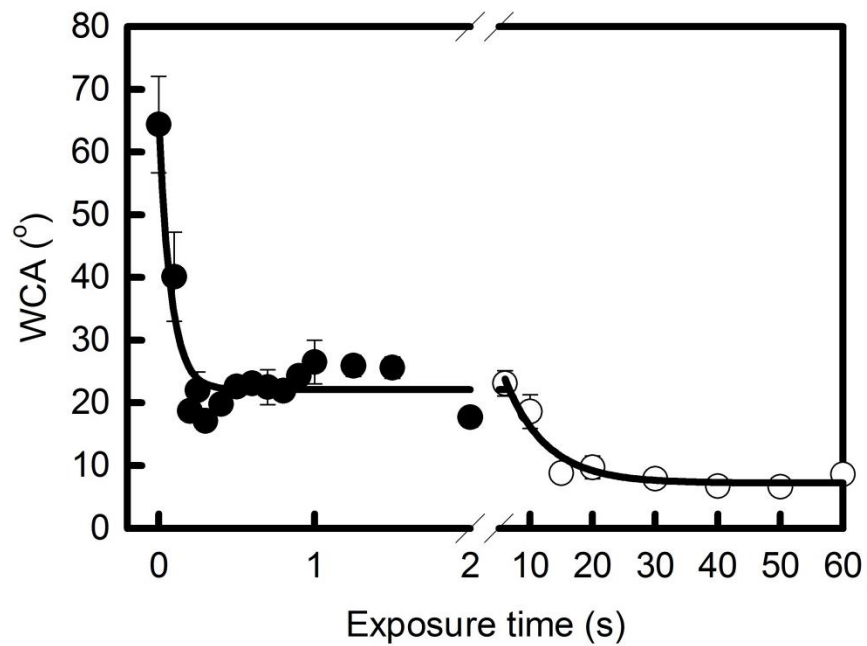


Figure 2.11. Dependence of the water contact angle (WCA) of polyimide on exposure time to the atmospheric pressure He/O₂ plasma. Solid dots (●) are data collected when WCA drops sharply with plasma exposure and open circles (○) are data collected when WCA becomes less sensitive to increasing plasma exposure.

Table 2.10. Dependence of polyimide surface roughness on exposure time to the atmospheric pressure He/O₂ plasma.

Exposure Time (s)	Roughness (nm)
0	7 ± 3
0.5	18 ± 8
10.0	17 ± 3
30.0	25 ± 3
60.0	25 ± 4

agreement with the bulk values. After sufficient exposure to the atmospheric pressure discharge, the carbon, oxygen and nitrogen amounts changed to 65%, 29% and 6%. The dependence of the surface oxygen concentration on treatment time is presented in Figure 2.12. Treatment was essentially complete after 1.0 s of exposure. The curve in the Figure is the best fit of Equation (6) to the data. The first-order rate constant obtained for atmospheric plasma oxidation of polyimide is $k_O = 2.9 \pm 1.5 \text{ s}^{-1}$. This value is close to that measured for FR-4 surface oxidation.

Figure 2.13 shows the carbon 1s spectra of polyimide before and after plasma activation. The spectrum of the control sample has been deconvoluted into four peaks located at 284.6, 285.5, 286.1, and 288.3 eV. These features are assigned to the aromatic/aliphatic carbon atoms (C=C and C-C bonds), amine carbon atoms (C-N bond), alcohol and ether carbon atoms (C-O bonds), and carbonyl carbon atoms (C=O bonds), respectively. The spectrum of the plasma treated specimen shows an additional peak at 289.1 eV, which is assigned to carboxylic acid groups (O-C=O bond) [59,89,97-99]. Based on the areas under each of the peaks, the distribution of surface carbon between these states was found to be 67% aromatic/aliphatic, 7% amine, 15% alcohol/ether, and 12% carbonyl groups.

Shown in Figure 2.14 is the distribution of oxidized carbon atoms on the polyimide surface as a function of the exposure time to the atmospheric pressure He/O₂, RF capacitive discharge. Initially, the untreated surface had roughly equal amounts of carbon atoms in C-O single-bonded and C=O double-bonded states. The amounts of these species increased on the surface with 0.5 s of plasma exposure. Then at 1.0 s of

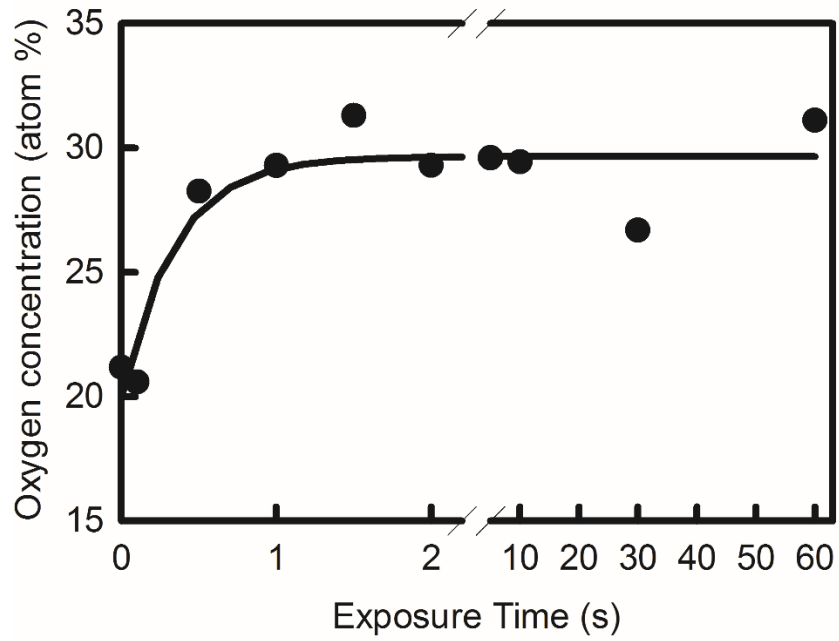


Figure 2.12. The oxygen atomic% on the polyimide surface as a function of exposure time to the atmospheric pressure He/O₂ plasma.

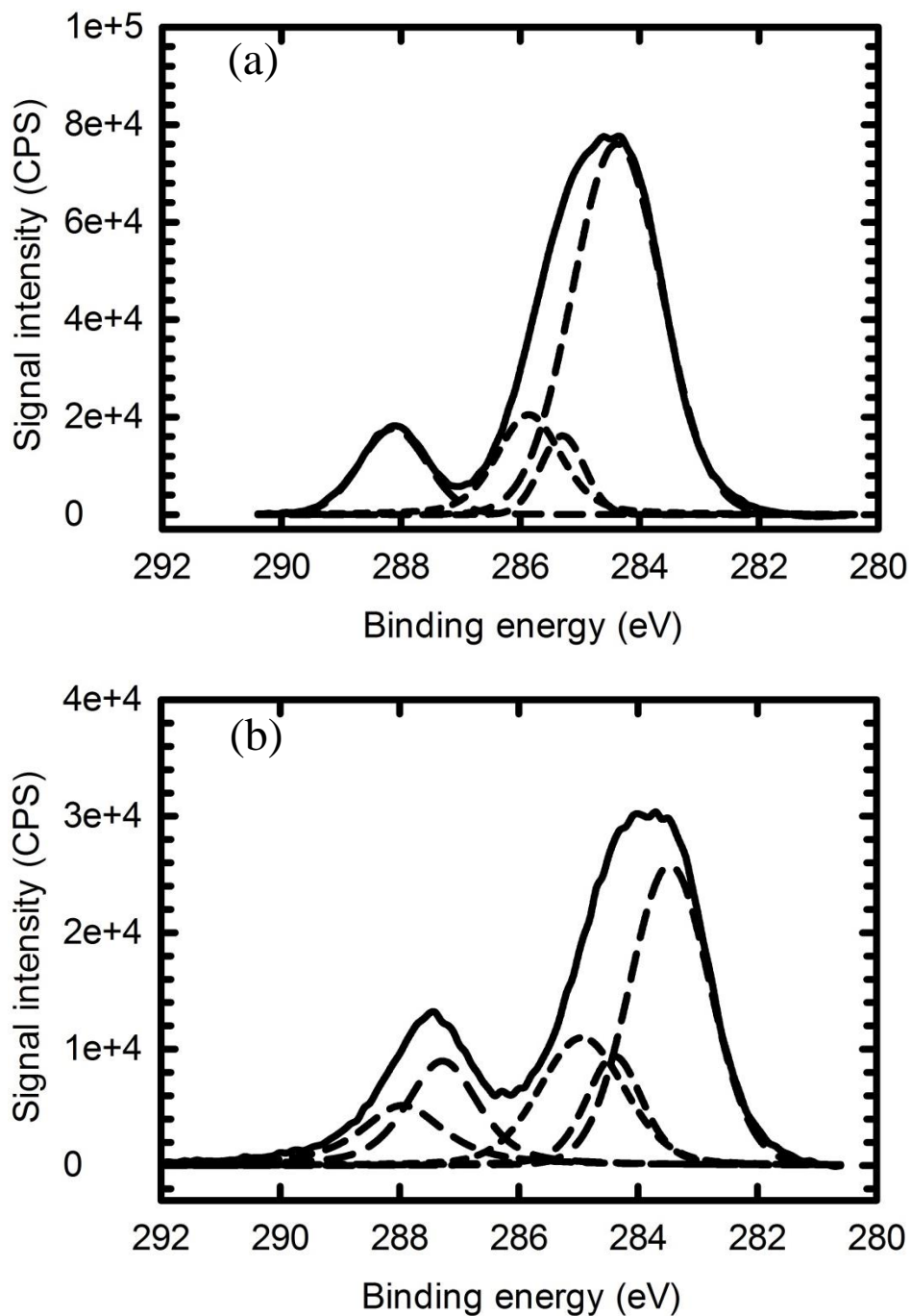


Figure 2.13. The carbon 1s spectra for polyimide: (a) before plasma treatment, and (b) after 10 s exposure to the atmospheric pressure He/O₂ plasma.

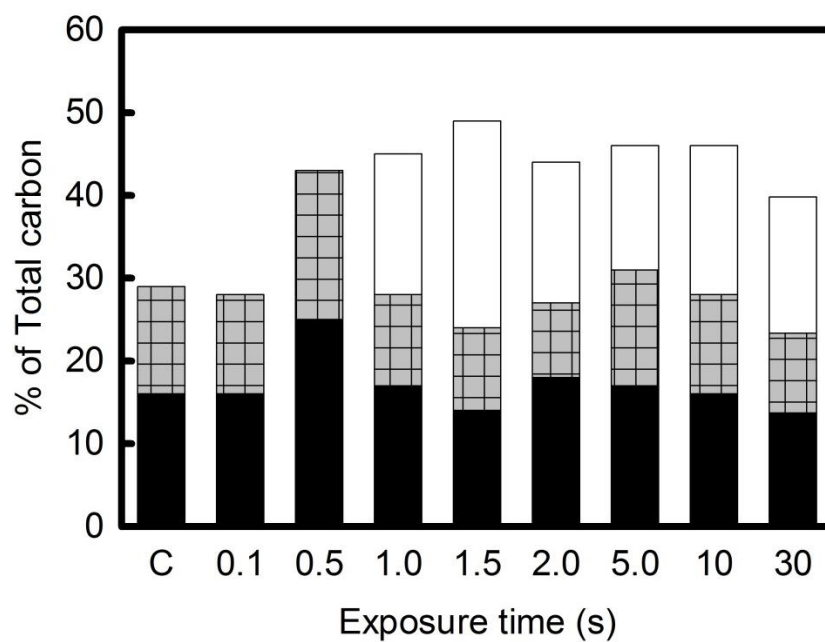





Figure 2.14. Distribution of oxidized carbon groups on the polyimide surface before and after the atmospheric pressure He/O₂ plasma treatment.  represents the C-O groups,  represents the C=O groups, and  represents the O=C-O groups.

plasma exposure, a significant number of carboxylic acid groups were generated on the surface. The distribution of species, 44% C-O, 30% C=O and 26% O-C=O, remained constant with longer treatments out to 30.0 s.

The effect of plasma treatment on the bond strength between polyimide and epoxy underfill was qualitatively evaluated using the T-peel test (ASTM D-1876) [68]. However, the sample preparation procedure was modified from the standard protocol as follows: Two pieces of 17.8 x 10.2 cm² polyimide sheets were bonded together using Hysol FP4549 underfill resin. The dimension of the bonded area was 12.7 x 10.2 cm². The bonded sample was cured at 160 °C and 55.2 MPa. The thickness of the underfill was controlled at 400 μm by using a stainless steel spacer during the adhesive cure.

Figure 2.15 shows the failure mode of the PI samples after the T-peel test. The untreated polyimide sheet was completely removed from the underfill surface when a peeling motion was applied. The force required for the delamination to occur was so small that it could not be detected by the 10 kN load cell on the Instron. In contrast, the plasma treated polyimide sheet was bonded to the underfill so strongly such that the sheet broke at the edge of the bonded region. Since the failure had occurred in the substrate, the quantitative bond strength between the plasma treated PI and the underfill could not be determined.

Polyimide treated with the atmospheric pressure He/O₂ plasma shows a dramatic improvement in bond strength to epoxy underfill. The degree of improvement is as good if not better than that reported for vacuum plasma treatment. Surface activation of the



Figure 2.15. T-peel failure mode of polyimide (PI) samples is (a) interfacial for PI not treated by atmospheric pressure He/O₂ plasma treatment, and (b) cohesive in the polymer for PI treated by the plasma treatment.

polymer changes the failure mechanism from interfacial at the adhesive-PI interface to cohesive within the underfill layer, or within the bulk PI film itself. The results presented above show that the bond strength correlates with the oxidation of the PI surface. A significant number of carboxylic acid groups are generated by plasma treatment, and these appear to be effective for chemically bonding to the epoxy adhesive [91,92].

The polymer chains comprising FR-4 and polyimide contain many aromatic rings. These rings are attacked by the atomic oxygen atoms produced in the plasma. In order to produce one carboxylic acid functional group, the aromatic ring must react with 3 oxygen atoms [75]. Therefore, one expects that plasma sources generating a large flux of ground-state oxygen atoms should activate these materials quickly. This is borne out by the results presented above. The atmospheric pressure RF capacitive discharge in He/O₂ generates up to 1.0 volume% oxygen atoms in the beam exiting from the source [51]. The bond strength of FR-4 and polyimide towards epoxy adhesives is maximized after 1.0 to 2.0 seconds exposure to this plasma beam.

2.6. Vacuum versus atmospheric plasmas for use in semiconductor packaging

The results presented in this chapter indicate that both vacuum plasmas and RF atmospheric pressure plasmas are effective for activating polymer surfaces for adhesion. Therefore, the selection of the appropriate equipment for surface activation should be based on the specific application, and which process provides the desired throughput, cost of ownership, and yield. In cases where large parts, such as whole PCBs, need to be treated, the vacuum plasma may be the lowest cost option. Since this machine operates in batch mode, large numbers of PCBs can be stacked on shelves and treated

simultaneously inside the chamber. By contrast, if one wants to treat a single part at a time, and to be able to trace back the plasma process performance to individual parts that were treated, then the atmospheric pressure plasma may be the better option. This is particularly true if the plasma can damage some of the materials passing through the process, such as the JEDEC trays. An advantage of the atmospheric pressure plasma is that it only treats those parts of the substrate that are scanned over by the reactive gas beam, and leaves the rest of the workpiece untouched.

Another difference between atmospheric and vacuum discharges is the way the substrate is contacted with the plasma. In the former case, the substrate is placed downstream of the plasma, so that the sample surface is only subjected to neutral reactive species that survive in the afterglow. By contrast, in the vacuum plasma, the substrate is immersed in the ionized gas discharge. Here, the sample surface is subjected to energetic electrons, high-energy argon ion bombardment, UV light, and the reactive neutral species. Argon ion bombardment can be advantageous if inorganic contaminants need to be sputtered off the substrate surface. On the other hand, if the bond pad consists of a 100 nm of gold on top of copper, then you certainly do not want Ar^+ sputtering to occur. In this case, the atmospheric pressure plasma may be the best choice, because it will thoroughly clean the gold without sputtering away a single Au atom.

In addition to activating polymer surfaces for bonding, vacuum and atmospheric pressure plasmas may be used to remove organic contamination [100]. Commonly seen organic contaminants in electronic packaging include epoxy bleed out during die attach, solder flux residue after reflow, and smears following via drilling. The presence of these contaminants on the substrate surface will adversely affect the assembly operation. The

atmospheric pressure He/O₂ plasma, with an atomic oxygen concentration of up to 1.0 volume% in the reactive gas beam can rapidly oxidize these contaminants and convert them into CO₂ gas [74]. In addition, since the plasma beam may be focused into a small spot that cleans only the area of interest, the process will not affect nearby delicate and expensive integrated circuits.

References

1. SEMI, Global semiconductor packaging materials outlook-2013/2014, <http://www.semi.org/en/node/45446> .
2. D.L. Thomas, D. O'Connor and J.A. Zitz, Area array leverage: Why and how to choose a package, in: *Area Array Interconnection Handbook*, K. Puttlitz and P.A. Totta (Eds.), pp. 1011-1030, Springer US, Norwell, MA (2001).
3. D. Frear, Packaging materials, in: *Springer Handbook of Electronic and Photonic Materials*, S. Kasap and P. Capper (Eds.), first edition, pp. 1267-1285, Springer Science + Business Media, New York (2006).
4. Electronic Engineering Times, The package interconnect selection quandary, http://www.eetimes.com/document.asp?doc_id=1225866 (2003).
5. M. Strobel, C.S. Lyons and K.L. Mittals (Eds.) *Plasma Surface Modification of Polymers: Relevance to Adhesion*, CRC Press, Boca Raton, FL (1994).
6. Semiconductor Manufacturing & Design Community, Industry Inches Towards 3D Chips, <http://semimd.com/blog/2013/04/02/industry-inches-towards-3d-chips/> (2013).
7. M.A. Lieberman and A.J. Lichtenberg, *Principles of Plasma Discharges and Materials Processing*, first edition, pp. 1-153, John Wiley & Sons, New York (1994).
8. F.F. Chen and J.P. Chang, *Lecture Notes on Principles of Plasma Processing*, Kluwer Academic/Plenum, New York (2003).
9. Y. P. Raizer, *Gas Discharge Physics*, Springer-Verlag, Berlin (1991).

10. Department of Energy Database, High frequency breakdown voltage, <http://www.osti.gov> (2011).
11. A. Schutze, J. Y. Jeong, S. E. Babayan, J. Park, G. S. Selwyn and R. F. Hicks, The atmospheric-pressure plasma jet: A review and comparison to other plasma sources. *IEEE Trans. Plasma Sci.* **26**, 1685-1694 (1998).
12. R. Hackam, Total secondary ionization coefficients and breakdown potentials of monoatomic gases between mild steel coaxial cylinders. *J. Phys. B* **2**, 201-215 (1969).
13. M. Moravej, X. Yang, G. R. Nowling, J. P. Chang, R. F. Hicks and S. E. Babayan, Physics of high-pressure helium and argon radio-frequency plasmas. *J. Appl. Phys.* **96**, 7011-7017 (2004).
14. NIST Standard Reference Database, Electron-Impact Ionization Cross Sections, in: *NIST Chemistry WebBook*, <http://webbook.nist.gov> (2011).
15. L. J. Kieffer and G. H. Dunn, Electron impact ionization cross-section data for atoms, atomic ions, and diatomic molecules: I. Experimental data. *Rev. Modern Phys.* **38**, 1-35 (1966).
16. S. Denifl, M. Santo, A. Stamatovic, P. Scheier and T. D. Mark, Electron-impact ionization of helium clusters close to the threshold: Appearance energies. *J. Chem. Phys.* **124**, 1-8 (2006).
17. D. C. Frost and C. A. McDowell, Studies of the ionization of molecules by electron impact. I. Excited states of the nitrogen molecular ion, Proc. Royal Soc. London. Series A **232**, 227-235 (1955).

18. W. F. Chan, G. Cooper and C. E. Brion, Absolute optical oscillator strengths for the photoabsorption of molecular oxygen (5–30 eV) at high resolution. *Chem. Phys.* **170**, 99-109 (1993).
19. J. Park, I. Henins, H. W. Herrmann and G. S. Selwyn, Gas breakdown in an atmospheric pressure radio-frequency capacitive plasma source, *J. Appl. Phys.* **89**, 15-19 (2001).
20. J. L. Walsh, Y. T. Zhang, F. Iza and M. G. Kong, Atmospheric-pressure gas breakdown from 2 to 100 MHz, *Appl. Phys. Lett.* **93**, 221505 (2008).
21. M. Moravej, X. Yang, R. F. Hicks, J. Penelon and S. E. Babayan, A radio-frequency nonequilibrium atmospheric pressure plasma operating with argon and oxygen, *J. Appl. Phys.* **99**, 093305 (2006).
22. S.Z. Li, Q. Wu, J.L. Zhang, D.Z. Wang and H.S. Uhm, Discharge characteristics of a radio-frequency capacitively coupled Ar/O₂ glow discharge at atmospheric pressure, *Thin Solid Films* **519**, 6990-6993 (2011).
23. J. L. Walsh and M. G. Kong, Room-temperature atmospheric argon plasma jet sustained with submicrosecond high-voltage pulses, *Appl. Phys. Lett.* **91**, 221502 (2007).
24. X. Yang, M. Moravej, G. R. Nowling, S. E. Babayan, J. Panelon, J. P. Chang and R. F. Hicks, Comparison of an atmospheric pressure radio-frequency discharge operating in the alpha and gamma modes, *Plasma Sources Sci. Technol.* **14**, 314-320 (2005).
25. J. J. Shi and M. G. Kong, Mechanisms of the alpha and gamma modes in radio-frequency atmospheric glow discharges, *J. Appl. Phys.* **97**, 023306 (2005).

26. Surfx Technologies, Atomflo™ 500,
<http://www.surfxtechnologies.com/products/atomflo-500/> (2013).
27. Nordson March, AP-1000 plasma treatment system,
<http://ww1.prweb.com/prfiles/2006/05/09/383537/AP1000new00172dpi.jpg>
(2013).
28. Y. Li, P. Kuai, P. Huo and C.J. Liu, Fabrication of CuO nanofibers via the plasma deposition of Cu(OH)₂, *Mater. Lett.* **63**, 188-190 (2009).
29. Plasmatreat, Openair® plasma sources,
<http://www.plasmatreat.co.uk/products-systems/plasma-system-components.html>
(2013).
30. T.S. Williams, H. Yu and R.F. Hicks, Atmospheric pressure plasma activation of polymers and composites for adhesive bonding, *Rev. Adhesion Adhesives* **1**, 46-87 (2013).
31. J. Ehlbeck, U. Schnabel, M. Polak, J. Winter, T. von Woedtke, R. Brandenburg, T. von dem Hagen and K. D. Weltmann, Low temperature atmospheric pressure plasma sources for microbial decontamination, *J. Phys. D: Appl. Phys.* **44**, 013002 (2011).
32. Y. Akishev, M. Grushin, A. Napartovich and N. Trushkin, Novel ac and dc non-thermal plasma sources for cold surface treatment of polymer films and fabrics at atmospheric pressure, *Plasmas Polym.* **7**, 261-289 (2002).
33. V. Nehra, A. Kumar and H.K. Dwivedi, Atmospheric non –thermal plasma sources, *Int. J. Eng.* **2**, 53-68 (2008).

34. Y. Kusano, Atmospheric pressure plasma processing for polymer adhesion – A review, *J. Adhesion* (2013), <http://dx.doi.org/10.1080/00218464.2013.804407> (published online).
35. M. Thomas and K.L. Mittal (Eds.), *Atmospheric Pressure Plasma Treatment of Polymers: Relevance to Adhesion*, Wiley-Scrivener, Beverly, MA (2013).
36. J.R. Roth, *Industrial Plasma Engineering: Principles*, Vol 1, IOP Publishing, Bristol, UK (2003).
37. C. Tendero, C. Tixier, P. Tristant, J. Desmaison and P. Leprince, Atmospheric pressure plasmas: A review. *Spectrochimica Acta Part B* **61**, 2-30 (2006).
38. O. Sakai, Y. Kishimoto and K. Tachibana, Integrated coaxial-hollow micro dielectric-barrier-discharges for a large-area plasma source operating at around atmospheric pressure. *J. Phys. D: Appl. Phys.* **38**, 431-441 (2005).
39. A. Jaworek and A. Krupa, Corona discharge from a multipoint electrode in flowing air. *J. Electrostatics* **38**, 187-197 (1996).
40. M. Moravej, X. Yang, M. Barankin, J. Penelon, S.E. Babayan and R.F. Hicks, Properties of an atmospheric pressure radio-frequency argon and nitrogen plasma, *Plasma Sources Sci. Technol.* **15**, 205-210 (2006).
41. S.E. Babayan, G. Ding, G.R. Nowling, X. Yang and R.F. Hicks, Characterization of the active species in the afterglow of a nitrogen and helium atmospheric-pressure plasma, *Plasma Chem. Plasma Processes* **22**, 255-269 (2001).
42. J. Park, I. Henins, H. W. Herrmann, G. S. Selwyn, J. Y. Jeong, R. F. Hicks, D. Shim and C. S. Chang, An atmospheric pressure plasma source. *Appl. Phys. Letters* **76**, 288-290 (2000).

43. X. Yang, S.E. Babayan and R.F. Hicks, Measurement of the fluorine atom concentration in a carbon tetrafluoride and helium atmospheric-pressure plasma, *Plasma Sources Sci. Technol.* **12**, 484-488 (2003).
44. O. Guaitella, L. Gatilova and A. Rousseau, Plasma-photocatalyst interaction: Production of oxygen atoms in a low pressure discharge, *Appl. Phys. Lett.* **86**, 151502 (2005).
45. E. Stoffels, W.W. Stoffels, D. Vender, M. Kando, G.M.W. Kroesen and F.J. de Hoog, Negative ions in a radio-frequency oxygen plasma, *Phys. Rev. E.* **51**, 2425-2435 (1995).
46. S. Denifl, M. Santo, A. Stamatovic, P. Scheier and T. D. Mark, Electron-impact ionization of helium clusters close to the threshold: Appearance energies. *J. Chem. Phys.* **124**, 1-8 (2006).
47. V.V. Ivanov, K.S. Klopovsky, D.V. Lopaev, A.T. Rakhimov and T.V. Rakhimova, Experimental and theoretical investigation of oxygen glow discharge structure at low pressures, *IEEE Trans. Plasma Sci.* **27**, 1279-1287 (1999).
48. M. Shibata, N. Nakano and T. Makabe, Effect of $O_2(a^1\Delta_g)$ on plasma structure in oxygen radio frequency discharges, *J. Appl. Phys.* **80**, 6142-6147 (1996).
49. J.S. Sousa, K. Niemi, L.J. Cox, Q.Th. Algwari, T.Gans and D. O'Connell, Cold atmospheric pressure plasma jets as sources of singlet delta oxygen for biomedical applications, *J. Appl. Phys.* **109**, 123302 (2011).
50. X. Lu, M. Laroussi and V. Puech, On atmospheric-pressure non-equilibrium plasma jets and plasma bullets, *Plasma Sources Sci. Technol* **21**, 034005 (2012).

51. E. Gonzalez, M. D. Barankin, P. C. Guschl and R. F. Hicks, Surface activation of poly(methyl methacrylate) via remote atmospheric pressure plasma. *Plasma Process. Polym.* **7**, 482-493 (2010).
52. Onboard Techology, Understand when to use FR-4 or high frequency laminates. <http://www.rogerscorp.com/documents/2122/acm/articles/Understanding-When-To-Use-FR-4-Or-High-Frequency-Laminates.pdf> (2011).
53. C.A. Camp, Solder masks, in: *Electronic Materials Handbook*, Vol. 1, M.L. Minges (Ed.), pp. 553-560, ASM International, Materials Park, Ohio (1989).
54. H.K. Yun, K. Cho, J.K. Kim, C.E. Park, S.M. Sim, S.Y. Oh and J.M. Park, Effect of plasma treatment of polyimide on the adhesion strength of epoxy resin/polyimide joints, *J. Adhesion Sci. Technol.* **11**, 95-104 (1997).
55. B.I. Noh, C.S. Seok, W.C. Moon and S.B. Jung, Effect of plasma treatment on adhesion characteristics at interfaces between underfill and substrate, *Int. J. Adhesion Adhesives* **27**, 200-206 (2007).
56. M.L. Sham, M. Lam and J.K. Kim, Adhesion characteristics of underfill material with various package components after plasma and UV/ozone treatments, in: *Proceedings of the Advances in Electronic Materials and Packaging*, 208-215 (2001).
57. J.D. Getty and J. Zhao, Plasma treatment for underfill process in flip chip packaging, in *Proceedings of the Pan Pacific Symposium* (2005).
58. F. D. Egitto, F. Emmi, R. S. Horwath and V. Vukanovic, Plasma-etching of organic materials .1. Polyimide in O₂-CF₄, *J. Vac. Sci. Technol., B*, **3**, 893-904 (1985).

59. K.L. Mittal, The role of the interface in adhesion phenomena, *Polym. Eng. Sci.* **17**, 467-473 (1977).
60. D. Bhusari, H. Hayden, R. Tanikella, S.A.B. Allen and P.A. Kohl, Plasma treatment and surface analysis of polyimide films for electroless copper buildup process, *J. Electrochem. Soc.* **152**, F162-F170 (2005).
61. M. A. Uddin, M. O. Alam, Y. C. Chan and H. P. Chan, Plasma cleaning of the flex substrate for flip-chip bonding with anisotropic conductive adhesive film, *J. Electronic Mater.* **32**, 1117-1124 (2003).
62. J. Zhao, J.D. Getty and D. Chir, Plasma processing for enhanced underfill, published in: *Chip Scale Review*,
<http://www.chipscalereview.com/issues/0704/article.php?type=feature&article=f6>
(2004).
63. PLASMAtech, Ultra-pure cleaning with low pressure gas plasma, in: Company Technical Paper, <http://www.plasmatechnology.com/pdf/PlasmaCleaningv2.pdf>
(2007)
64. J. Zhao and J.D. Getty, Plasma for underfill process in flipchip packaging, in: March Plasma Systems Application Notes, <http://www.nordson.com/en-us/divisions/march/support/Literature/Documents/techpaper-semiconductorapplications2.pdf> (2006).
65. Standard test method for apparent shear strength of single-lap-joint adhesively bonded metal specimens by tension loading (metal-to-metal), ASTM D1002-10 (2013).

66. Standard test method for determining strength of adhesively bonded rigid plastic lap-shear joints in shear by tension loading, ASTM D3163-01 (2013).
67. Test method for measurement of adhesive strength between leadframes and molding compounds, SEMI G69-0996 (2013).
68. Standard test method for peel resistance of adhesives (T-peel test), ASTM D1876-08 (2013).
69. Standard test method for 90 degree peel resistance of adhesives, ASTM D-6862-11 (2013).
70. G. Borcia, C. A. Anderson and N. M. D. Brown, The surface oxidation of selected polymers using an atmospheric pressure air dielectric barrier discharge. Part I. *Appl. Surface Sci.* **221**, 203-214 (2004).
71. G. Borcia, C. A. Anderson and N. M. D. Brown, The surface oxidation of selected polymers using an atmospheric pressure air dielectric barrier discharge. Part II. *Appl. Surface Sci.* **225**, 186-197 (2004).
72. D. D. Pappas, A. A. Bujanda, J. A. Orlicki and R. E. Jensen, Chemical and morphological modification of polymers under a helium-oxygen dielectric barrier discharge. *Surface Coatings Technol.* **203**, 830-834 (2008).
73. E. R. Ionita, M. D. Ionita, E. C. Stancu, M. Teodorescu and G. Dinescu, Small size plasma tools for material processing at atmospheric pressure. *Appl. Surface Sci.* **255**, 5448-5452 (2009).
74. E. Gonzalez, M. D. Barankin, P. C. Guschl and R. F. Hicks, Remote atmospheric-pressure plasma activation of the surfaces of polyethylene terephthalate and polyethylene naphthalate. *Langmuir* **24**, 12636-12643 (2008).

75. E. Gonzalez, M. D. Barankin, P. C. Guschl and R. F. Hicks, Ring opening of aromatic polymers by remote atmospheric-pressure plasma. *IEEE Trans. Plasma Sci.* **37**, 823-831 (2009).
76. P. Esena, C. Riccardi, S. Zanini, M. Tontini, G. Poletti and F. Orsini, Surface modification of PET film by a DBD device at atmospheric pressure. *Surface Coatings Technol.* **200**, 664-667 (2005).
77. S. Yang and M. C. Gupta, Surface modification of polyethyleneterephthalate by an atmospheric-pressure plasma source. *Surface Coatings Technol.* **187**, 172-176 (2004).
78. M. Noeske, J. Degenhardt, S. Strudthoff and U. Lommatzsch, Plasma jet treatment of five polymers at atmospheric pressure: Surface modifications and the relevance for adhesion. *Intl. J. Adhesion Adhesives* **24**, 171-177 (2004).
79. T. Homola, J. Matousek, B. Hergelova, M. Kormunda, L. Wu and M. Cernak, Activation of poly(ethylene terephthalate) surfaces by atmospheric pressure plasma. *Polymer Degradation Stability* **97**, 2249-2254 (2012).
80. K. G. Kostov, A. L. R. dos Santos, R. Y. Honda, P. A. P. Nascente, M. E. Kayama, M. A. Algatti and R. P. Mota, Treatment of PET and PU polymers by atmospheric pressure plasma generated in dielectric barrier discharge in air. *Surface Coatings Technol.* **204**, 3064-3068 (2010).
81. O. J. Kwon, S. W. Myung, C. S. Lee and H. S. Choi, Comparison of the surface characteristics of polypropylene films treated by Ar and mixed gas (Ar/O₂) atmospheric pressure plasma. *J. Colloid Interface Sci.* **295**, 409-416 (2006).

82. H. M. S. Iqbal, S. Bhowmik and R. Benedictus, Surface modification of high performance polymers by atmospheric pressure plasma and failure mechanism of adhesive bonded joints. *Intl. J. Adhesion Adhesives* **30**, 418-424 (2010).
83. H.S. Fogler, *Elements of Chemical Reaction Engineering*, third edition, Prentice Hall, Saddle River, New Jersey (1999).
84. R. Sanapala, Characterization of FR-4 printed circuit board laminates before and after exposure to lead-free soldering conditions, Master thesis, University of Maryland, College Park, MD, USA (2008).
85. M. Rakotomalala, S. Wagner, and M. Doring, Recent developments in halogen free flame retardants for epoxy resins for electrical and electronic applications, *Materials* **3**, 4300-4327 (2010).
86. Y. X. Liu, E. T. Kang, K. G. Neoh, J. F. Zhang, C. Q. Cui and T. B. Lim, Surface graft copolymerization enhanced adhesion of an epoxy-based printed circuit board substrate (Fr-4) to copper, *IEEE Trans. Adv. Packaging* **22**, 214-220 (1999).
87. G. Z. Xiao, M. Delamar and M. E. R. Shanahan, Irreversible interactions between water and DGEBA/DDA epoxy resin during hygrothermal aging, *J. Appl. Polym. Sci.* **65**, 449-458 (1997).
88. C.D. Wagner and G.E. Muilenberg, *Handbook of X-ray Photoelectron Spectroscopy: A Reference Book of Standard Data for Use in X-ray Photoelectron Spectroscopy*, pp. 38-39, Perkin-Elmer Corp., Eden Prairie, MN (1979).
89. B. I. Noh and S. B. Jung, Characterisation of FR-4 substrate with various plasma treatment conditions, *Mater. Sci. Technol.* **23**, 792-798 (2007).
90. Personal communication with Kash Mittal (June 17, 2013).

91. M. Fedoseev, M. Gurina, V. Sdobnov and A. Kondyurin, Study of the reaction of epoxides with carboxylic acids by IR and Raman spectrometry. *J. Raman Spectroscopy* **27**, 413-418 (1995).
92. W. Blank and M. Picci, Catalysis of the epoxy-carboxyl reaction. *J. Coating Technol.* **74**, 33-41 (March 2002).
93. R. J. Zaldivar, H. I. Kim, G. L. Steckel, J. P. Nokes and B. A. Morgan, Effect of processing parameter changes on the adhesion of plasma-treated carbon fiber reinforced epoxy composites. *J. Composite Mater.* **44**, 1435-1453 (2010).
94. R. J. Zaldivar, H. I. Kim, G. L. Steckel, H. I. Kim and B. A. Morgan, The effect of atmospheric plasma treatment on the chemistry, morphology and resultant bonding behavior of a PAN-based carbon fiber-reinforced epoxy composite. *J. Composite Mater.* **44**, 137-156 (2010).
95. L. F. M. da Silva, T. N. S. S. Rodrigues, M. A. V. Figueiredo, M. F. S. F. de Moura and J. A. G. Chousal, Effect of adhesive type and thickness on the lap shear strength, *J. Adhesion* **82**, 1091-1115 (2006).
96. A. D. Crocombe, Global yielding as a failure criterion for bonded joints, *Int. J. Adhesion Adhesives* **9**, 145-153 (1989).
97. R.A. Difelice, An investigation of plasma pretreatments and plasma polymerized thin films for titanium/polyimide adhesion, Ph.D. thesis, Virginia Polytechnic Institute and State University, Blacksburg, VA, USA (2001).
98. N. Inagaki, S. Tasaka and K. Hibi, Surface modification of Kapton film by plasma treatments, *J. Polym. Sci., PartA: Polym. Chem.* **30**, 1425-1431 (1992).

99. S.B. Lee and Y.-K. Kim, Adhesion improvement of polyimide/metal interface by He/O₂/NF₃ atmospheric pressure plasma, *Plasma Process Polym.*, 6, S525-S529 (2009).
100. D.F. O’Kane and K.L. Mittal, Plasma cleaning of metal surfaces, *J. Vac. Sci. Technol.* **11**, 567-569 (1974).

Chapter 3

Surface Preparation using Atmospheric Pressure Plasma for Adhesive Bonding of Carbon-Fiber-Reinforced Epoxy Laminates

Abstract

The effect of surface preparation methods on the surface composition of carbon-fiber-reinforced composites (Cycom® 5320-1/IM7 and Cycom® 977-3/IM7) has been studied. Methods of interest include peel ply, mechanical abrasion, and atmospheric pressure plasma oxidation. Analyzing untreated 5320-1 and 977-3 by X-ray photoelectron spectroscopy revealed that the surfaces contained 26 and 30 atom% fluorine, respectively. The fluorine may affect the adhesive bonding of composites and can be removed by using peel ply or aggressive sanding. Exposure to plasma was the only technique that increased the oxygen concentration of 5320-1 and 977-3, raising them to 33 and 40 atom%, respectively. The changes in surface chemistry after different treatments were compared to published work. Results from previous publications suggested that the change in surface chemistry of 5320-1 and 977-3 by plasma oxidation is likely to increase their adhesive bonding strength.

3.1 Introduction

Carbon fiber reinforced composite (CFRC) continued to gain traction as structural material for aircrafts and satellites. Adhesively bonded CFRCs show many advantages over metals held together by mechanical fasteners and rivets. Benefits brought about by CFRC include high strength-to-weight ratio, easy to shape, resistance to corrosion, high stress bearing area, and fast repair capability [1]. Previous work has reported that pretreating the surface of composites with peel ply, sanding, and atmospheric pressure plasma [2,3] leads to higher adhesion strength between the composites and adhesives. The enhancement in adhesion has been attributed to cleaner surfaces, a rougher morphology, higher oxygen concentrations, and the presence of specific functional groups

Here, we report on effects of different treatments on the surface chemistry of carbon fiber reinforce epoxy composites (Cycom® 5320-1/IM7 and Cycom® 977-3/IM7). Samples were treated with peel ply, sanding, and atmospheric pressure helium and oxygen plasma and characterized using X-ray photoelectron spectroscopy (XPS). The effect of each treatment on the surface chemistry of the CFRC has been compared to previous work. A close relationship between surface chemistry and adhesion is shown.

3.2 Experimentation

3.2.1 Materials

The fiber reinforced epoxy composites used in this work were Cycom® 5320-1/IM7 (5320-1) and Cycom® 977-3/IM7 (977-3). Some of the 5320-1 samples were fabricated with peel ply while all of the 977-3 samples were manufactured without peel

ply. When peel ply was not used, the sample surface was covered with a release film during manufacture. In addition, one sample of MTM45-1/IM7 was used for comparison purpose in the discussion of surface cleanliness. More information on the MTM45-1/IM7 system can be found in the paper by Cheng et al [4].

Two-ply polyester acetone cloth (PROSAT® Quiltec®) was used to clean the sample surface. Sand paper with 200 grit was used when abrasion of the specimens was required.

3.2.2 Sample preparation

After peel ply (PP) or release film was removed from the sample, the surface was cleaned with an acetone wipe (AW) and dried. Afterwards, the sample was treated by sanding, plasma oxidation, or a combination of the two methods. Whenever sanding was required, the sample was abraded with the 200 grit sand paper. There were three levels of abrasion. The lightly sanded (S-) surface was gently abraded for 5 passes. The moderately sanded (S) surface was abraded until the reflective surface turned dull gray. The aggressively sanded (S+) surface was abraded until fiber became visible. Unless otherwise specified, when plasma oxidation was used in series with abrasion, the composite sample was moderately sanded. All sanded samples were cleaned with acetone and dried immediately after the abrasion. Since all samples were cleaned with acetone wipe, for the remaining part of this paper, epoxy composites fabricated without peel ply are referred to as AW, epoxy composites fabricated with peel are referred to as PPAW, and epoxy composites treated with mechanical abrasion are referred to as PPSAW and SAW for those fabricated with and without peel ply, respectively.

Plasma activation was accomplished using a Surfex[®] Technologies Atomflo[™] system equipped with a 2-in-wide linear beam source. The plasma was struck with radio frequency (RF) power at 27.12 MHz. The RF generator and matching network were model RF-3X and AM-10 from RF VII, Inc, respectively. An I&J Fisnar 7000C robot was used to translate the plasma source over the samples. A source to substrate distance of 2.0 ± 0.5 mm was maintained during all experiments. The scan speed of source over substrate used for 5320-1 was 14.8 ± 0.3 mm/s and for 977-3 was 4.3 ± 0.1 mm/s. At these scan speeds, the number of scans corresponding to 1 second of plasma exposure time has been calculated to be 4 and 1 scan for 5320-1 and 977-3, respectively. Plasma exposure time was estimated following the procedure described by Gonzalez et al [5]. A more detailed description of the plasma system and calculated exposure time can be found in the work by Cheng et al [4]. The RF power and gas flow used to generate the plasma are listed in Table 3.1 below.

3.2.3 Chemical and mechanical characterization

The surface composition and carbon bonding states of the CFRC were characterized using X-ray photoelectron spectroscopy (XPS) in an ultrahigh vacuum chamber with a base pressure of 1×10^{-9} Torr. Immediately after treatment, the sample coupon was placed into the chamber and characterized. Exposing samples to Mg K_{α} X-ray at 1253.6 eV excited core electrons from carbon (C) 1s, oxygen (O) 1s, nitrogen (N) 1s, fluorine (F) 1s, sulfur (S) 2p, and silicon (Si) 2p energy levels. The photoelectrons were detected using a PHI 3057 spectrometer. All spectra were taken in small-area mode with a 7° acceptance angle and 23.5 eV passing energy. The takeoff angle with respect to the surface normal was 25° . The C 1s, O 1s, N 1s, F 1s, S 2p, and Si 2p peaks were

Table 3.1. Plasma oxidation parameters for composite systems.

Material	Power (W)	Helium (LPM)	Oxygen (LPM)	Standoff (mm)	Scan Speed (mm/s)	Number of Scans
5320-1	150	30	0.50	2	14.8	4
977-3	180	30	0.75	2	4.3	1

referenced to sp^2/sp^3 carbon (284.6/285.0 eV), hydroxyls (532.8 eV), amine (298.4 eV), CF_2 (688.9 eV), SO_4^{2-} (168.5 eV), and SiO_2 (100.4 eV) [6]. The surface composition was calculated by integrating the photoemission peak intensity of each element and dividing by their corresponding sensitivity factors. These factors were 0.296, 0.711, 0.477, 1.000, 0.666, and 0.339 for C 1s, O 1s, N 1s, F 1s, S 2p, and Si 2p, respectively.

Error sources in XPS characterization include sample loading, measurement, and data analysis. The error from sample loading was determined by transferring the same sample from the loading chamber to the stage three times and obtaining photoelectron spectra each time. The surface composition and carbon bonding states of the three spectra were compared, and the standard errors range was calculated. To account for error arising from the measurement, a sample was characterized three times without leaving the stage. To account for error arising from data analysis, the same set of data was deconvoluted three times. The standard errors for surface composition were 2.3, 2.5, and 0.6 atom% for carbon, oxygen, and nitrogen, respectively. The standard errors for the carbon bonding state were 3.2, 3.1, 2.5, and 1.4 % of total carbon atoms for sp^2/sp^3 carbon, hydroxyl carbon, carbonyl carbon, and carboxylic acid carbon, respectively.

3.3 Results

3.3.1 Effect of treatment methods on surface composition of 5320-1/IM7

Figure 3.1 shows the survey spectra of as-received 5320-1/IM7 with and without peel ply. The spectrum of the specimen fabricated without peel ply shows a strong peak at 688.9 eV, which is due to fluorine. In contrast, the specimen fabricated with peel ply does not have a photoemission peak at 688.9 eV. This implies that using peel ply during

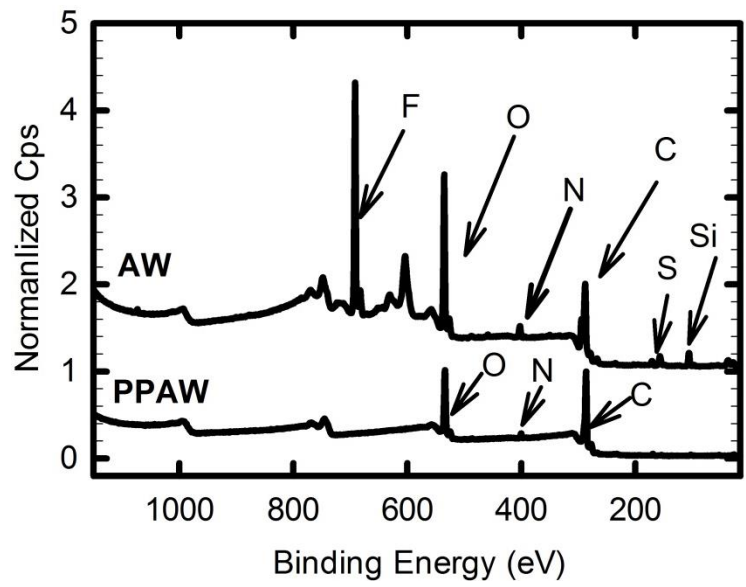


Figure 3.1. Survey spectra of 5320-1 fabricated without peel ply (AW) and with peel ply (PPAW).

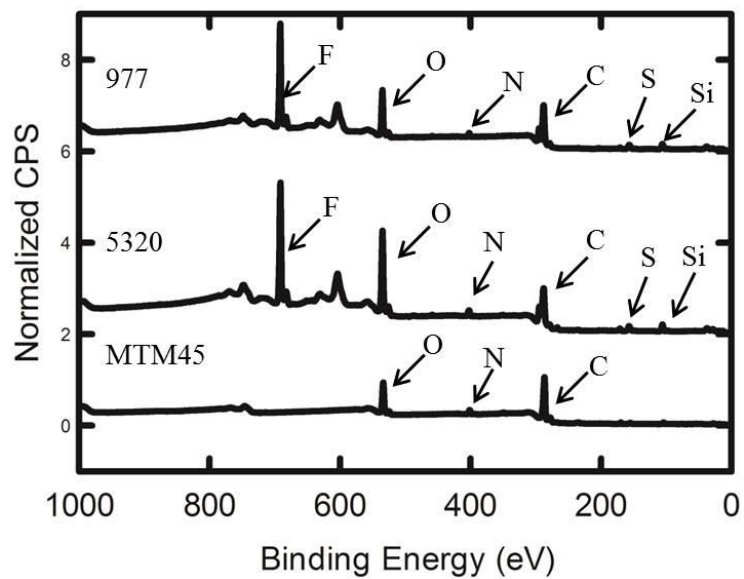


Figure 3.2. Survey spectra of 977-3, 5320-1, and MTM45-1 fabricated without peel ply.

manufacturing will prevent fluorine contamination of the composite surface. Figure 3.2 shows the survey spectra of 977-3, 5320-1, and MTM45-1 manufactured without peel ply. Spectra of both 5320-1 AW and 977-3 AW exhibit evidence of fluorine, but the spectrum of MTM45-1 AW remains fluorine free.

Feedback from the material supplier, indicates that the 5320-1 and 977-3 were fabricated using the same release film, but MTM45-1 was cured with a different release film. This information suggests that fluorine on the 5320-1 and 977-3 were transferred there from the release films used during the high temperature cure. Therefore, the selection of the release film plays a major role in the cleanliness of the composite surface. In addition to fluorine, traces of sulfur and silicon have been identified in the survey spectra of 5320-1 and 977-3. Sulfur is used in the iron catalyzed production of carbon fiber [7], moreover silicon is an ingredient for lubricants and mold releases [8]. However, because the detected concentrations of sulfur and silicon are only 0.7 and 3.9 atom%, these elements will not be examined further in this work.

Fluorinated polymers, due to their low surface energy can contribute to poor adhesion between the composite and the adhesive [9]. Table 3.2 shows that applying peel ply to the composite can prevent fluorine transfer to the bonding surface. However, peel ply and peel ply plus sanding do not change the oxygen concentration on the surface of the sample. Table 3.3 shows the effect of plasma oxidation on 5320-1 AW. After 15 s of plasma exposure, the surface concentration of fluorine is reduced to 1.0 atom%. Simultaneously, the oxygen concentration increases from 23.5 to 33.4 atom% in 15 s. The nitrogen concentration also increases from 2.9 to 9.3 atom%.

Table 3.2. Effect of peel ply and peel ply plus sanding on the surface chemistry of 5320-1 AW epoxy composite.

	Surface composition (atom%)			
	C1s	O1s	N1s	F1s
AW	42.9	23.5	2.9	26.0
PPAW	70.1	26.4	2.1	0.0
PPSAW	72.4	22.0	3.7	0.2
PPS+AW	75.6	17.2	5.0	0.4
PPS-AW	73.6	19.8	4.6	0.4

Table 3.3. Effect of plasma oxidation on the surface chemistry of 5320-1 AW epoxy composite.

	Surface composition (atom%)			
	C1s	O1s	N1s	F1s
0 s Plasma	42.9	23.5	2.9	26.0
1 s Plasma	54.5	15.1	2.8	23.7
3 s Plasma	49.7	22.8	4.5	19.1
6 s Plasma	48.1	27.8	8.8	9.1
9 s Plasma	45.7	32.8	9.9	3.7
15 s Plasma	47.5	33.4	9.3	1.0

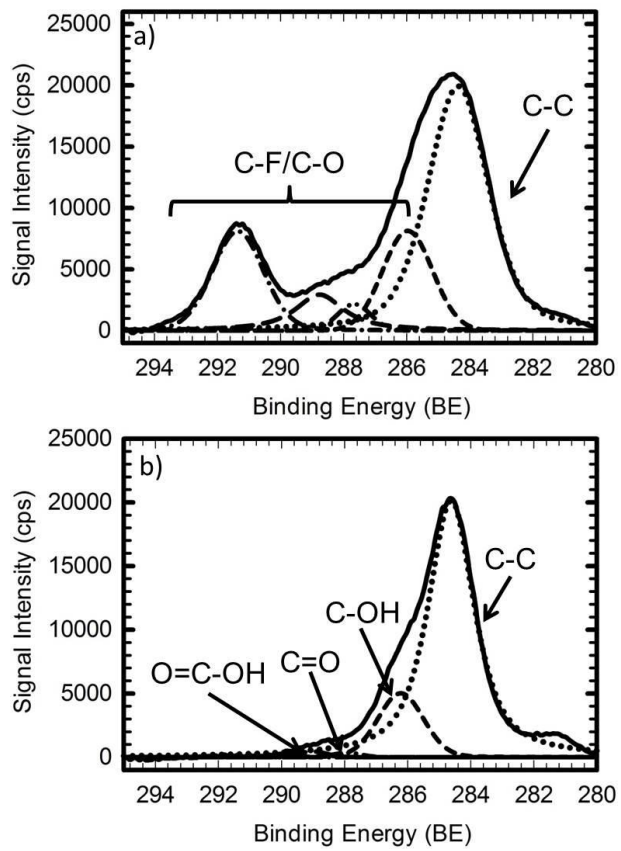


Figure 3.3. a) Carbon 1s spectrum of 5320-1 AW before cleaning and after 15 s of treatment.

Figure 3.3a) and 3.3b) shows the C 1s spectra of 5320-1 AW before and after plasma cleaning. Deconvoluting the spectrum of the control sample reveals C-F_x species. The C-O and C-F peaks in the C 1s spectrum are overlapping, thus the carbon bonding states cannot be sorted out in this case. After 15s of plasma oxidation, the C 1s spectrum of the fluorine-free surface is deconvoluted into four peaks. The two major peaks at 284.6 and 286.2 eV correspond to the C-C and C-OH bonds. Two smaller peaks located at 287.9 and 289.0 eV are assigned to C=O and O=C-OH bonds. This result suggests that plasma oxidation of 5320-1 AW converts aromatic and aliphatic carbons into alcohols, and to a much less extent, carbonyls and carboxylic acids.

Figure 3.4 shows the response of 5320-1 PPAW to increasing plasma exposure times. From 0 to 9 seconds, the oxygen concentration increases linearly from 26.4 to 44.8 atom%. Beyond 9s, the change in oxygen concentration with increasing plasma exposure is minimal. In the absence of fluorine atoms, the C 1s spectra before and after plasma oxidation are deconvoluted to C-C, C-OH, C=O, and O=C-OH groups, which are located at 284.6, 286.2, 287.9, and 289.0 eV, respectively.

Figure 3.5 shows the effect of plasma exposure time on the carbon bonding states of 5320-1 PPAW. The fraction of oxidized carbon increases from 31.7 to 49.9 % of the total carbon atoms after 1 s of oxidation, and this value changes only slightly for exposure time beyond 1 s. Note that the fraction of oxidized carbon differs somewhat from the surface oxygen concentration in Figure 3.4. This difference is explained by the presence of elements other than C and O on the surface. The concentration of hydroxyl groups increases from 25.1 to 41.4 % of the total carbon after 1s of plasma oxidation.

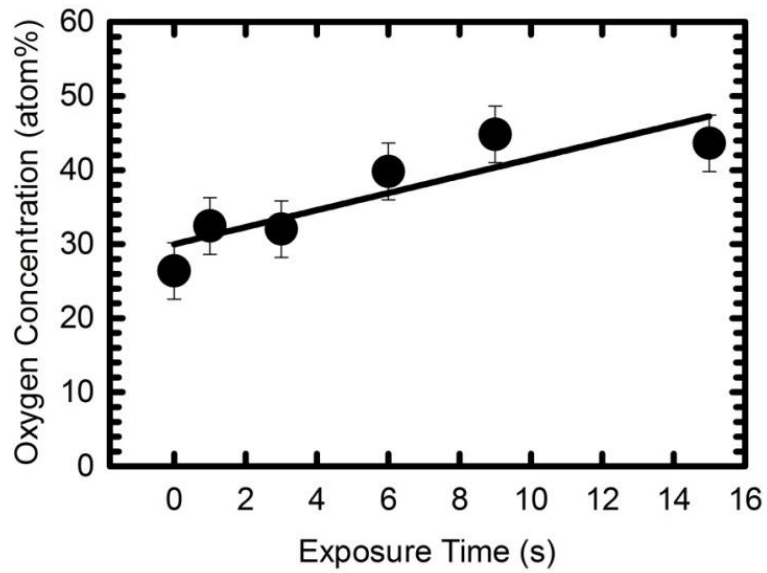


Figure 3.4. Oxygen concentration on the surface of 5320-1 PPAW as a function of plasma exposure time.

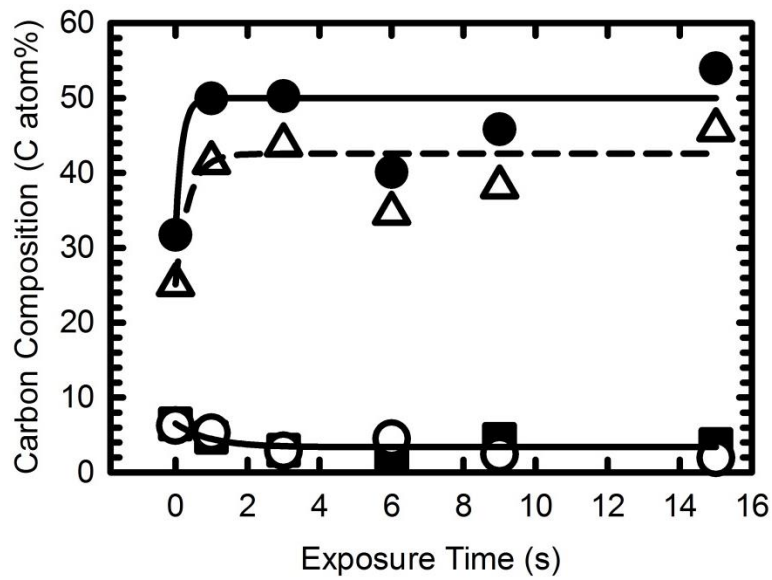


Figure 3.5. Fraction of oxidized carbon (●), C-OH (Δ), C=O (○), and O=C-OH (□) as a function of plasma exposure time for 5320-1 PPAW.

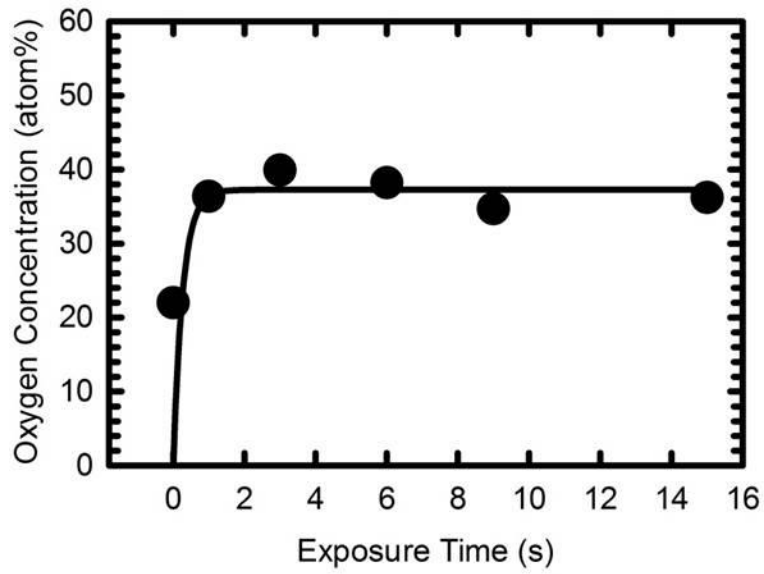


Figure 3.6. Oxygen concentration on the surface of 5320-1 PPSAW as a function of plasma exposure time.

After 1s, the concentration of hydroxyl group remains constant. Conversely, the fractions of carbonyl and carboxylic acid groups are unaffected by the plasma oxidation, and each of these groups account for 4 ± 2 % of total carbon atoms. These results are similar to plasma oxidation of 5320-1 AW for 15 s, which converts carbon atoms to mostly hydroxyl groups with little increase in the concentration of carbonyl and carboxylic acid groups. Figure 3.6 shows the response of the surface oxygen concentration on sanded 5320-1 (PPSAW) to plasma exposure time. In contrast to the unsanded 5320-1 (PPAW), the surface composition is more sensitive to plasma oxidation. The oxygen concentration of 5320-1 PPSAW increases rapidly. The surface oxygen concentration of 5320-1 PPSAW increases from 22.0 atom% before treatment to 39.9 atom% after 3 s of exposure to the He+O₂ plasma.

The distribution of carbon bonding states is plotted in Figure 3.7. Within 1 second, the fraction of oxidized carbon rises rapidly from 16.3 to 48.9 % of total carbon atoms. When the exposure time is extended beyond 1 s, the amount of oxidized carbon decreases gradually to about 26 ± 4 atom% of total carbon atoms. Similarly, the percentage of hydroxyl groups jumps from 14.3 to 32.7 % in 1 s of exposure. Thereafter, the fraction of hydroxyl groups declines with exposure to about 17 ± 3 atom% after 9s of oxidation. The fractions of C=O and O=C-OH groups on 5320-1 PPSAW shows some initial response to plasma oxidation. In 6 s, the percentage of carbonyl group increases from 0.8 % of total carbon atoms to 3.6 % and the percentage of carboxyl group increases from 1.2 % of total carbon to 12.6 %. Beyond 6s of treatment, the carbonyl and carboxylic acid groups decrease gradually in concentration to about 5.0 atom %.

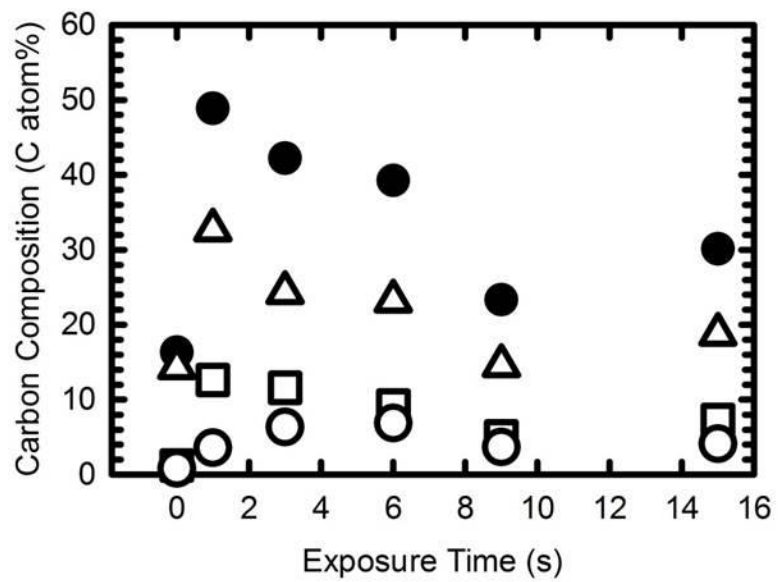


Figure 3.7. Carbon bonding state on the surface of 5320-1 PPSAW including total oxidized carbon (●), C-OH (▲), C=O (○), and C-OOH (□) as a function of plasma exposure time.

Table 3.4. Effects of mechanical abrasion on the surface chemistry of 977-3.

	Surface composition (atom%)			
	C1s	O1s	N1s	F1s
AW	46.2	17.4	1.9	29.9
SAW	59.1	16.0	2.9	18.6
SAW+	43.8	40.8	9.1	1.4
SAW-	57.6	19.8	2.8	15.4

Table 3.5. Effects of plasma oxidation on the surface chemistry of 977-3.

	Surface composition (atom%)			
	C1s	O1s	N1s	F1s
AW 0s Plasma	46.2	17.4	1.9	29.9
AW 3s Plasma	20.3	40.8	0.5	24.6
AW 6s Plasma	20.8	43.1	1.0	20.9
AW 9s Plasma	34.9	32.9	3.1	22.2

3.3.2 Effect of treatment methods on surface composition of 977-3/IM7

Since 977-3/IM7 composites were fabricated without peel ply, the surfaces of these as-receive samples were covered with up to 30 atom% fluorine. Table 3.4 shows the effect of mechanical abrasion on the surface chemistry of 977-3 AW. It is seen that though sanding is capable of removing fluorine atoms from 977-3, the cleaning process is highly dependent on the applied force and abrasion time. Very aggressive abrasion is needed to create a fluorine free surface. Table 3.5 shows the effect of plasma oxidation on 977-3 AW. Unlike the treatment of 5320-1 AW, 9 s of plasma oxidation on 977-3 AW only reduces the concentration of fluorine atoms to 22 ± 2 %. The different response by 5320-1 AW and 977-3 AW to plasma cleaning is likely due to the difference in the diffusion depth of fluorine atoms into the composites during curing. Table 3.6 shows the combined effect of mechanical abrasion and plasma oxidation in reducing the concentration of fluorine atoms on 977-3. In this case, 9 s of plasma cleaning reduces the concentration of fluorine atoms to 8.1 atom%.

Also evident in Tables 3.4, the oxygen concentration on 977-3 does not change with mechanical abrasion unless aggressive sanding is employed. It is suspected that when a sample is abraded aggressively, the treatment removes contaminated surface layer to expose an oxygen-rich underlayer, leading to an increase in oxygen concentration from 17.4 to 40.8 atom%. Table 3.5 shows that 3 s of plasma oxidation increases the surface oxygen concentration of 977-3 to a value of 38 ± 5 atom%. Since both C-O_x and C-F_x are present on the sample surface, it is difficult to identify the carbon bonding states by deconvoluting the C 1s peak. Table 3.6 shows that the oxygen concentration on

Table 3.6. Combined effects of mechanical abrasion and plasma oxidation on the surface chemistry of 977-3.

	Surface composition (atom%)			
	C1s	O1s	N1s	F1s
SAW 0s Plasma	59.1	16.0	2.9	18.6
SAW 3s Plasma	60.9	25.9	4.8	6.3
SAW 6s Plasma	52.8	26.7	4.6	12.7
SAW 9s Plasma	54.8	27.5	5.2	8.1

moderately sanded 977-3 increases from 16.0 to 25.9 atom% after 3 s of plasma exposure, and remains constant with further treatment time.

3.3.3 Effect of surface treatment on composite adhesion

The surface chemistry of 5320-1 and 977-3 collected after different treatment methods correlates well to previously published results. For example, Hollaway et al. [10] and Flinn et al. [11] stated that the function of peel ply is to prevent contamination and to provide a clean bonding surface. Davies et al. [12] affirms that samples fabricated using peel ply do not show higher bonding strength than clean samples fabricated without peel ply. Results from these researcher coincides with the current finding that peel ply does not functionalize the composite. Jölly et al. [13] and Zaldivar et al. [2,14] discovered that the increase in adhesion strength after mechanical abrasion is related to the surface structure of the specimen. In fact, Gude and coworkers [15] reported that after abrasion, the mode I fracture energy of a composite shows a linear relation to its surface roughness. This information address the question why is the surface oxygen concentration insensitive to sanding when mechanical abrasion is known to improve the bonding strength between adhesively jointed composites.

Zaldivar and coworkers [2,14] have also noticed that the oxygen plasma activation of fiber reinforced epoxy composite affects both the surface chemistry of the composite and its adhesive bonding strength. They correlated the bonding strength to the extent of surface oxidation, specifically the fraction of carbons that are carboxylic acids. In their case, Zaldivar reported that the adhesion strength of the bonded joint increases linearly with the concentration of carboxylic acids. Williams et al. [3] have summarized

the effect of plasma activation on the adhesive bonding between polymers. In his work, the increase in adhesion strength between polymers after plasma activation was only related to the total oxygen concentration on the polymer surface instead of specific functional group. In current work, an increase in the oxygen concentration on 5320-1 and 977-3 is observed after plasma activation. The results from this work show that plasma activation of composite surface converts carbon atoms into hydroxyl group instead of carboxylic acid groups, as in the case of Zaldivar et al [2,14]. However, this result could be simply a difference in the composition of the epoxy resin used to make the material. The stiffness of the carbon fibers may also play a role in the effect of preparation procedure on adhesion strength and failure mode.

It is expected that the oxidation of carbon atoms into hydroxyl groups should contribute toward enhancing the adhesive bonding strength 5320-1 and 977-3 samples, as see in examples in Williams' review. Lastly, it is interest to note that after Zaldivar treated the epoxy composite with the plasma, there were 2 to 4 atom% fluorine remaining on the bonding surface [2]. This however, didn't prevent the adhesively bonded sample from achieving 100% cohesive failure. We hypothesize that the fluorine contaminant may not play a major role in the adhesion of plasma oxidized samples, because the high concentration of oxidized functional groups provides sufficient sites for the adhesive to bind to.

3.4 Summary

Different surface preparation methods were compared for Cycom® 5320-1/IM7 and 977-3/IM7 composite systems. It was found that the untreated surfaces of both

epoxy composite were rich in fluorine contaminants. Applying peel ply to the composite surface prevented contaminant diffusion surface layer, however peel ply removal did not activate the composite. Mechanical abrasion and plasma oxidation slowly removed fluorine contaminants from the composite surfaces. However, only plasma treatment was able to populate the sample surface with functional groups. The surface chemistry of 5320-1 and 977-3 showed good correlation to previous work. For the effect of different surface preparation procedures on the adhesion strength of 5320-1/IM7 and 977-3/IM7, refer to work by Cheng et al [4] and Palmer et al [16].

References

1. Composites UK, NCN report-Adhesive bonding of Composites, <http://www.compositesuk.co.uk/Information/FAQs/Joining.aspx> (2014).
2. R. J. Zaldivar, H. I. Kim, G. L. Steckel, J. P. Nokes and B. A. Morgan, Effect of processing parameter changes on the adhesion of plasma-treated carbon fiber reinforced epoxy composites. *J. Composite Mater.* **44**, 1435-1453 (2010).
3. T.S. Williams, H. Yu and R.F. Hicks, Atmospheric pressure plasma activation of polymers and composites for adhesive bonding, *Rev. Adhes. Adhes.*, **1**, 46-87 (2013).
4. D. Cheng and M. Grigoriev, "Trust: Atmospheric Plasma Recipe Development." *SAMPE Technical Conference Proceedings*. Seattle, WA, June 2-5, 2014. ITAR CD-ROM.
5. E. Gonzalez, M. D. Barankin, P. C. Guschl and R. F. Hicks, Remote atmospheric-pressure plasma activation of the surfaces of Polyethylene Terephthalate and Polyethylene Naphthalate. *Langmuir* **24**, 12636-12643 (2008).
6. C.D. Wagner and G.E. Muilenberg, *Handbook of x-ray photoelectron spectroscopy: a reference book of standard data for use in x-ray photoelectron spectroscopy*, pp. 38-39, Perkin-Elmer Corp. (1979).
7. P. Morgan, *Carbon Fibers and Their Composites*, Taylor & Francis Group, Boca Raton (2005).
8. G. L. Anderson, S. D. Stanley, G. L. Young, R. A. Brown, K. B. Evans and L. A. Wurth, The Effects of Silicone Contamination on Bond Performance of Various Bond Systems, *J. Adhes.* **86**, 1159-1177 (2010).

9. M. R. Wertheimer, L. Martinu and J. E. Klemberg-Sapieha, Plasma treatment of polymers to improve adhesion, in: *Adhesion Promotion Techniques*, K. L. Mittal (Ed.), pp 147-153, Marcel Dekker, Inc., New York (2002).
10. L.C. Hollaway and P.R. Head, *Advance Polymer Composites and Polymers in the Civil Infrastructure*, first edition, pp. 121-123, Elsevier Science Ltd, Oxford (2001).
11. Brian D. Flinn, Brian K. Clark, Jeffrey Satterwhite and Peter J. Van Voast, Influence of peel ply type on adhesive bonding of composites, Proceedings of the Sampe 2007 Annual Technical Conference, Baltimore, MD (2007).
12. P. Davies, C. Baley, H. Loaec and Y. Grohens, Interlaminar Tests for marine applications. Evaluation of the influence of peel plies and fabrication delays, *Appl. Compos. Mater.*, **12**, 293-307 (2005).
13. I. Jölly, M. Wolfahrt, G. Pinter and W. Kern, Surface characterization and functionalization of composites to optimize bonded repairs for aircraft structure, presented at:FACC Technical Colloquium, Salzburg, Austria (2012).
14. R. J. Zaldivar, H. I. Kim, G. L. Steckel, H. I. Kim and B. A. Morgan, The effect of atmospheric plasma treatment on the chemistry, morphology and resultant bonding behavior of a PAN-based carbon fiber-reinforced epoxy composite. *J. Composite Mater.* **44**, 137-156 (2010).
15. M. R. Gude, S. G. Prolongo, A. Ureña, Adhesive bonding of carbon fibre/epoxy laminates: Correlation between surface and mechanical properties. *Surf. Coat. Technol.* **207**, 602-607 (2012).

16. Palmer, M., Cheng, D., Grigoriev, M., “TRUST: Qualification of Atmospheric Plasma Surface Preparation for the No Bolt Bondline.” *SAMPE Technical Conference Proceedings*. Seattle, WA, June 2-5, 2014. ITAR CD-ROM.

Chapter 4

Rapid Oxidative Activation of Carbon Nanotube Yarn and Sheet by a Radio Frequency, Atmospheric Pressure Helium and Oxygen Plasma

Abstract

Carbon nanotube yarn and sheet were activated using radio frequency, atmospheric pressure, helium and oxygen plasmas. The nanotubes were exposed to the plasma afterglow, which contained $8.0 \times 10^{16} \text{ cm}^{-3}$ ground state O atoms, $8.0 \times 10^{16} \text{ cm}^{-3}$ metastable O_2 ($^1\Delta_g$), and $1.0 \times 10^{16} \text{ cm}^{-3}$ ozone. X-ray photoelectron spectroscopy and infrared spectroscopy revealed that 30 seconds of plasma treatment converted 25.2 % of the carbon atoms on the CNT surface to oxidized species, producing 17.0 % alcohols, 5.9 % carbonyls, and 2.3 % carboxylic acids. The electrical resistivity increased linearly with the extent of oxidation of the CNT from 4 to $9 \times 10^{-6} \Omega\text{-m}$. On the other hand, the tensile strength of the yarn was decreased by only 27% following plasma oxidation.

4.1 Introduction

The characterization of the multiwall carbon nanotubes (CNTs) by Sumio Iijima in 1991 [1] initiated a two-decades long research effort to exploit the mechanical, electrical, and thermal properties of these materials. One of the proposed uses of carbon nanotubes is to serve as a reinforcement material in composites. The ability of the nanotubes to improve composite properties depends heavily on their compatibility with the polymer matrix. Carbon nanotubes tend to agglomerate, and are difficult to disperse in organic or inorganic solvents [2]. Thus, one of the challenges in fabricating carbon nanotube reinforced composites is to uniformly distribute a high percentage of the nanotubes in the resin. In more recent years, the production of nanotube fibers, yarn and sheet, has provided a means of making large-scale structures out of CNT reinforced composites. However, the carbon nanotube yarns and sheets exhibit tensile strengths well below their theoretical limits, i.e., in the range of 1.0 – 2.0 GPa, due to fiber pull out within the nanotube bundles [3]. To overcome this problem, methods are being developed to crosslink together the CNT with resins.

Currently, the standard approach to activate carbon nanotubes for chemical coupling is to immerse them in an acid solution at elevated temperature for several hours [4]. Acids commonly used to treat nanotubes include nitric acid, sulfuric acid, piranha solution, or a mixture of nitric and sulfuric acids. This treatment inserts hydroxyl (-OH) and carboxylic acid (-COOH) groups onto the nanotube surface, which enables it to form covalent bonds with polymers. The harsh reaction conditions in the acid bath convert a large fraction of the sp^2 carbon atoms into ketones and carboxylic acids through ring opening reactions. This can lead to structural damage of the CNT and reduces the tensile strength of yarns and sheets [5]. Alternatively, the carbon nanotubes may be activated under more mild conditions using plasma chemistry [6].

Plasma treatment of carbon nanotubes has been performed under vacuum and at atmospheric pressure. The length of nanotubes exposure to vacuum plasma can vary from 5 s to 1800 s, and up to 25 % of the carbon atoms are oxidized [7-11]. By comparison, atmospheric pressure plasmas are more suitable for continuous processing of CNT. Previous work on treating nanotubes includes: arc-like discharges [12, 13], dielectric barrier discharges [5, 14, 15], and radio frequency (RF) argon and oxygen plasma [16-18]. The plasma treatment time of CNTs at atmospheric pressure ranges from 3 s to 120 s. Up to 9.0 atom% oxidized carbon groups have been generated.

In this work, we report on the activation of carbon nanotube yarn and sheet using a radio frequency (RF), atmospheric pressure (AP), helium and oxygen plasma. Changes in the chemical properties of the CNT have been analyzed by water contact angle measurements (WCA), X-ray photoelectron spectroscopy (XPS), Fourier transform infrared spectroscopy (FT-IR), and scanning electron microscopy (SEM). In addition, the mechanical and electrical properties of the nanotube yarn were measured using a microforce tensile machine and a multimeter. It was found that a maximum of 25 % of the exposed carbon atoms on the CNT were oxidized by the plasma over an exposure time of 30 s, which is a significantly higher level of activation. This doubled the electrical resistivity, while decreasing the yarn tensile strength from about 550 to 404 MPa.

4.2 Experimental methods

4.2.1 Materials

Both the carbon nanotube yarn and sheet used in this work were acquired from Nanocomp Inc. The nanotubes were grown by chemical vapor deposition and were spun into a

yarn or compressed into a sheet after exiting the furnace. The average diameter of a yarn ranged from 35 to 45 μm , whereas the thickness of the sheets was approximately 20 μm . Tensile strength and electrical resistivity measurements were performed using the yarn, conversely, the surface characterization by XPS, FT-IR, and SEM was performed on the sheet.

4.2.2 Plasma treatment

An AtomfloTM 400L2 from Surfx[®] Technologies LLC was used in this work. The 2-inch wide linear plasma source was powered by an RF generator with a matching network operating at 27.12 MHz. The plasma was fed with 30.0 L/min of industrial grade helium (99.995%) and 0.5 L/min of ultrahigh-purity oxygen (99.999%) at 1 atm, and it was operated with 150 W of applied power. An XYZ robot, RB300-XY from Surfx[®] Technologies LLC, was used to accurately and reproducibly translate the plasma source over the samples.

Prior to plasma treatment, the nanotube yarn was cut into 4.0 cm or 10.0 cm segments, while the sheet was cut into squares with dimensions of 1.0 x 1.0 or 2.0 x 2.0 cm^2 . The samples were fixed to a stage during the experiment, and the plasma device was adjusted to a 5.0 mm vertical distance from the sample. The plasma device was then scanned over the sample at 200 mm/s or 20 mm/s depending on the desired exposure time. The exposure time under the plasma was calculated by dividing the effective plasma beam width, L , by the scan speed, and then multiplying by the number of scans. For the linear beam plasma, the effective width was $L=2.1$ cm [19].

4.2.3 Surface characterization

The water contact angle (WCA) on a carbon nanotube sheet was measured using a Krüss EasyDrop goniometer. To make the measurement, a 2 μL water droplet was brought into contact with the sample surface. The shape of the water droplet was captured by a digital camera, and a

software program quickly calculated the contact angle. Six measurements were made for each sample, and the average contact angle was reported.

The surface composition of carbon nanotube sheet before and after the plasma treatment was analyzed by X-ray photoelectron spectroscopy (XPS). The 1.0 x 1.0 cm² square sheets were mounted on a molybdenum sample holder and loaded onto the stage in the ultrahigh vacuum chamber. Core-level photoemission spectra of C 1s and O 1s lines were collected with a PHI 3057 spectrometer using Mg K α X-rays source at 1253.6 eV. All XPS spectra were taken in small-area mode with a 7 $^\circ$ acceptance angle and 23.5 eV passing energy. The detection angle with respect to the surface normal was 25 $^\circ$. The resolution of the source + analyzer is 1.4 eV. The collected spectra data were analyzed using XPS Peaks version 4.1. The background contribution to signal intensity was removed via method proposed by Tougaard et. al [20]. The surface atomic composition was calculated by integrating the area under the carbon 1s and oxygen 1s photoemission peaks and divide the results by their respective sensitivity factor, 0.30 and 0.71 respectively [21].

Fourier transform infrared spectroscopy was used to identify the functional groups that were formed on the carbon nanotube surface by plasma treatment. The FTS-50A spectrometer used in these experiments was manufactured by Bio-Rad, and it was equipped with a mercury cadmium telluride (MCT) detector. For these measurements, the CNT sheet was cut into a 2.0 x 2.0 cm² square and fixed over a 13.0 mm circular opening on a stainless steel slide. The sample thickness was reduced through layer by layer removal with Kapton[®] tape until the light throughput across the sample became measureable by the detector. The spectra were collected at 8 cm⁻¹ resolution with signal-averaging over 2048 scans. A single beam spectrum of the pristine sheet was taken first. Subsequently, the sheet was exposed to the plasma while remaining

attached to the slide. A single beam spectrum was collected after each iteration of plasma treatment. Absorbance spectra were calculated of the treated samples, using the untreated sample as the background reference.

The surface topography of the carbon nanotube sheet before and after plasma treatment was obtained using a Nova 600 NanoLab DualBeamTM SEM/FIB from FEI CompanyTM. The control and plasma-activated samples were examined at a magnification of 19,000 X to determine the effect of the plasma process on the surface of the nanotube sheet. More detailed scans of the samples were taken at approximately 150,000 X to observe changes in individual fibers.

4.2.4 Dispersion in resin

Three pieces of CNT yarn from the same spool were dispersed in 3 ml of dicyclopentadiene (DCPD) monomer. The yarn samples were given three different treatments: 1) exposure to the plasma operated at conditions described in the first paragraph of section 2.2, with a 20 mm/s scan speed for 30 seconds; 2) immersion in a solution of 3 ml of DCPD monomer with 0.15 ml of [(5-bicyclo[2.2.1]hept-2-enyl)ethyl]trimethoxysilane coupling agent; and 3) plasma activation followed by immersion in the coupling agent. Following these processes, the samples were immersed in DCPD monomer and placed in an ultrasonic bath for 30 minutes. The amount of dispersion of the CNTs into the resin was observed visually.

4.2.5 Electrical conductivity

The electrical resistivity of the CNT yarn was measured by laying a 40-mm sample flat on an insulating glass slide. The two ends of the yarn were glued to the slide using electrically conductive silver paste. A small square of molybdenum (Mo) foil was pressed against the silver

paste at each end of the yarn in order to improve the sample's contact to the electrical probes. Electrical measurements were taken by contacting the probe tips of a Fluke 114 multimeter to the molybdenum contacts.

4.2.6 Tensile testing

The mechanical strength of the CNT yarn was characterized by longitudinal tension. The tensile test was carried out according to ASTM D 3822-07 [22], in which A MTS Tytron 250 microforce testing system with 50 N load cell was used. During the test, the displacement control was set to a crosshead speed of 5 mm/min. Sample CNT yarns were first mounted on paper frames with 10 mm gauge length using cyanoacrylate glue. The diameter of each yarn was measured at nine locations under optical microscope. The average of the nine measurements was used to calculate the apparent cross-sectional area and subsequently to calculate the tensile strength of the yarns. The measurements were performed at room temperature. At least five samples were tested after each treatment time. The average and standard deviation of the tensile strength were reported.

4.3 Results

4.3.1 Surface energy

Pictures of the contact angle between the water droplet and the nanotube sheet before and after plasma treatment are shown in Figure 4.1. Prior to plasma treatment, the carbon nanotube sheet has a low surface energy, making it hydrophobic with a WCA of 120°. Exposing the CNT to the plasma for 10 s reduces the contact angle between the water droplet and the surface to $< 5^\circ$, i.e. it becomes superhydrophilic. Even with plasma exposure only on the top side of the CNT

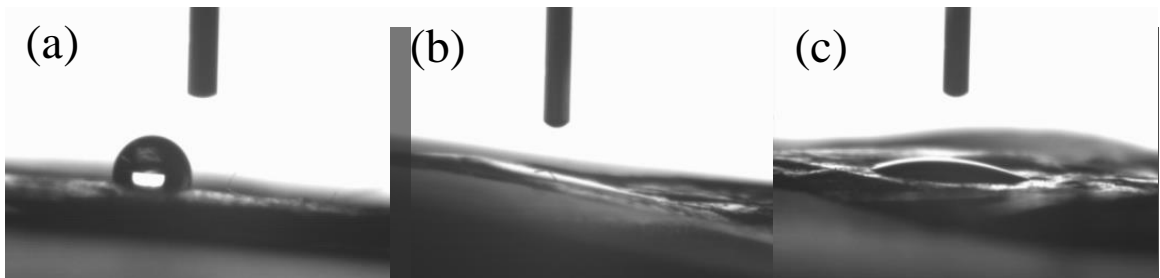


Figure 4.1. Water contact angles recorded on (a) as-received CNT sheet, (b) front side of CNT sheet after 10 s of plasma treatment, and (c) back side of CNT sheet after 30 s of plasma treatment.

sheet, one finds that the WCA on the backside of the CNT sheet has fallen to 30° after a 30 s of plasma exposure.

The dependence of the water contact angle on the plasma exposure time is shown in Figure 4.2. Here, the solid squares represent measurements that were obtained from the front surface of the sample, whereas the open circles represent measurements that were obtained from the back. The water contact angle on the front side follows an exponential decay with exposure time to a final value < 5° after 5 seconds. The contact angle as a function of the exposure time t was fitted with the following equation :

$$WCA(t) = WCA_{Max} + [(WCA_o - WCA_{MAX}) \exp(-k_{WCA}t)], \quad (1)$$

where the WCA_o is the initial contact angle, WCA_{max} is the final contact angle, and k_{WCA} is the first-order rate constant for the reduction of the water contact angle. The solid line in Figure 4.1 represents the best fit of Eq. (1) to the contact angle measured on the front surface of the sheet. A first order rate constant of 3.1 s⁻¹ was calculated from the fitted line.

The contact angle values on the back surface of the CNT as a function of plasma exposure time are also presented in Figure 4.2. For the first 5 s of the plasma exposure, the WCA on the backside is 125°. After 5 s, the contact angle starts dropping with exposure time at a linear rate, so that after 30 s, it has fallen to 30°. Measurements beyond 30 s were not taken. The delay in the response of the water contact angle on the back surface of the CNT is likely due to the fact that sites for adsorption of the reactive species on the front side must first be consumed before reaction can begin on the back. Note that the front side WCA reaches its final minimum value after only 5 s.

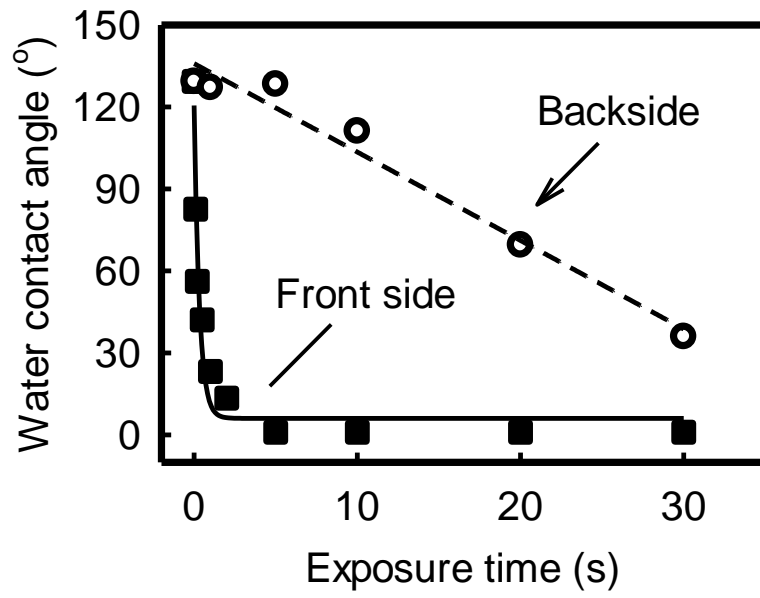


Figure 4.2. Dependence of water contact angle on plasma exposure time on the front and back side of the carbon nanotube sheet.

4.3.2 Surface composition

Shown in Figure 4.3 are the XPS survey spectra of the CNT sheet before and after its exposure to the atmospheric pressure helium and oxygen plasma. There are two dominant photoemission peaks present in the spectra, which correspond to photoelectrons ejected from C 1s and O 1s core orbitals at 285 and 520 eV, respectively [21]. Prior to the plasma treatment, the intensity of O 1s peak on the CNTs is negligible. The appearance of O 1s peak on the CNTs with plasma exposure time is clearly evident. A photoemission peak close to 411 eV is observed on some of the spectra, which is assigned to the molybdenum 3p orbital [21]. This feature is due to the Mo sample holder and may be neglected.

The C 1s photoemission spectrum of the as-received sample is shown in Figure 4.4 (a). The spectrum is deconvoluted into 2 peaks, which are assigned to sp^2 - sp^3 carbon (peak no. 1) and π - π^* interactions (peak no. 5), respectively. No oxidized carbon groups are assigned to this spectrum, because the O 1s emission in Figure 4.3 indicates that the oxygen concentration on the untreated surface is below 2%. The sp^2 - sp^3 carbon atoms are assigned to a single peak since the difference in their binding energies is less than the resolution of the spectrometer. To deconvolute this spectrum, the center of peak 5 is fixed to 291.8 eV in the data analysis program, and the peak is adjusted using the software until it fits the geometry of the high energy tail. The remainder of the spectrum is assigned to the sp^2 - sp^3 carbons centered at 284.6 eV (peak no. 1). Analogous to highly ordered pyrolytic graphite, the sp^2 - sp^3 peak is asymmetric with a long tail on the high energy side [24]. The asymmetric peak shape has been explained by Ago and Van Attekum as arising from many-body interactions of the conduction electrons induced by low energy electron-hole excitation [24, 25].

An example of carbon 1s emission from the plasma-activated CNT is shown in

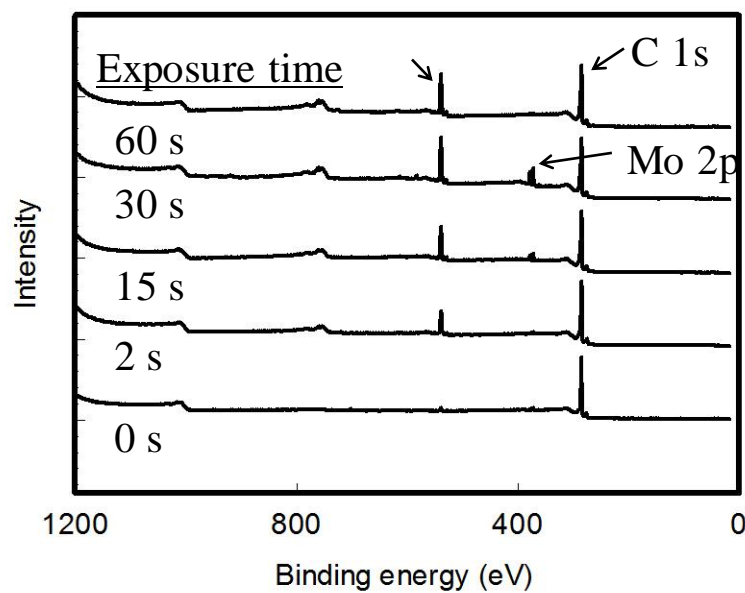


Figure 4.3. XPS survey spectra of the CNT as a function of plasma exposure time.

Figure 4.4 (b). This spectrum has been deconvoluted into 5 peaks. Peak 1 centered at 284.6 eV and peak 5 centered at 291.8 eV are assigned to the sp^2 - sp^3 carbon atoms and the π - π^* interactions, as in Figure 4.4 (a). Peaks 2 through 4, located at 286.3 eV, 287.9 eV, and 289.0 eV, are assigned to alcohols (-OH), ketones (C=O), and carboxylic acids (HO-C=O), respectively. Peaks 1 and 5 are generated by fitting the corresponding peaks from the control sample (a) into the spectrum of the plasma-activated sample (b), maintaining the same positions and numerical multiplier for both features. Next, peaks 2, 3 and 4 are deconvoluted into the alcohol, ketone, and carboxylic acid groups. Here the center of the alcohol, ketone, and carboxylic acid peaks are fixed at 1.7, 3.3, and 4.4 eV from the apex of peak 1 in accordance with previously published results [21, 25].

The distribution of oxidized carbon atoms at different plasma exposure times is listed in Table 4.1. The untreated CNT sheet received from Nanocomp Inc. contains greater than 98.0% sp^2 - sp^3 carbon and less than 2.0% oxidized carbon. The amount of sp^2 - sp^3 carbon decreases to 84.3% after 2 seconds of treatment. The oxidized carbon atoms are distributed as following: 10.7% hydroxyl groups, 2.6% ketones, and 2.4% carboxylic acids. The amount of oxidized carbon increases with plasma exposure time, which causes the fraction of bound alcohol and ketones to rise to 17.0 and 5.9 %, respectively, after 30 seconds of treatment. Conversely, the fraction of carbons associated with carboxylic acid groups remains constant with exposure time at about 2.5%.

The oxygen-to-carbon ratio is plotted against the plasma exposure time in Figure 4.5. This ratio was calculated using two methods. First, the amount of oxygen and carbon were obtained by integrating the areas under the O 1s and C 1s photoemission peaks and dividing these areas by the corresponding sensitivity factor. Secondly, the oxygen composition was

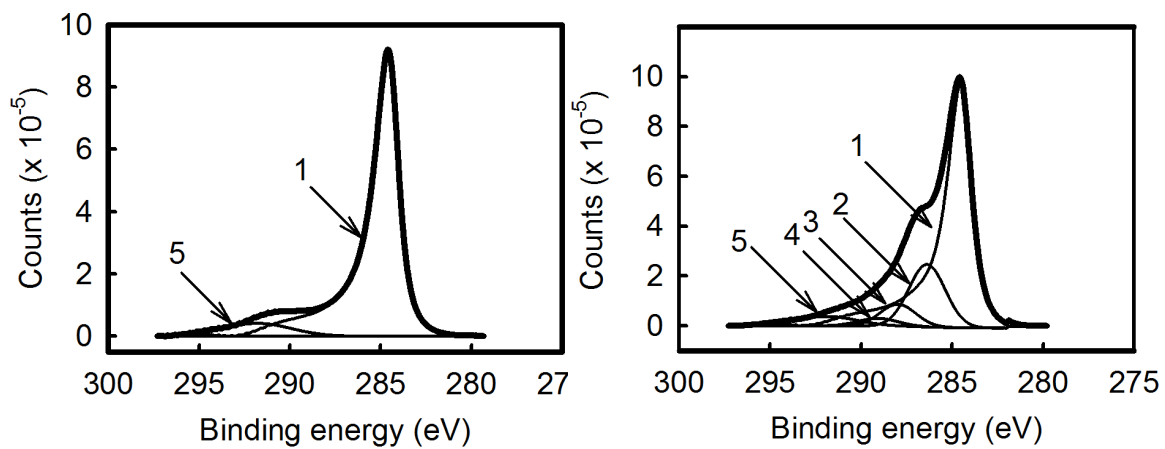


Figure 4.4. The C 1s photoemission spectrum of CNT sheet: (a) untreated, and (b) 30s of plasma activation.

calculated by summing the area under the oxidized C 1s constituents, and dividing this sum by the area under the entire C 1s band. Good agreement between the atomic ratios calculated by the two methods supports the method chosen to deconvolute the C 1s spectrum shown in Figure 4.4(b).

The dependence of oxygen to carbon ratio on the plasma exposure time, t , follows an exponential function represented by the following equation:

$$O/C(t) = O/C_o + (O/C_{MAX} - O/C_o)[1 - \exp(-k_{O/C}t)], \quad (2)$$

where O/C_o is the oxygen to carbon ratio prior to plasma exposure, O/C_{MAX} is the oxygen to carbon ratio when the value is saturated, and the $k_{O/C}$ is the first order rate constant for the oxidation of the carbon atoms. The solid and dashed lines in Figure 4.5 represent the best fit of Eq. (2) for the oxygen to carbon ratio calculated via the two methods. The $k_{O/C}$ calculated from the two best fit lines were 0.27 and 0.17 s^{-1} , respectively. These values are an order of magnitude lower than the rate constant for the reduction of the water contact angle (3.1 s^{-1}).

Single-beam infrared spectra of the CNT sheet are plotted in Figure 4.6 as a function of plasma exposure time from 0 to 30 s. There are three easily identifiable trends in the spectra. The light throughput between 400 cm^{-1} and 1200 cm^{-1} decreased strongly with treatment time, while the light throughput between 1200 cm^{-1} and 5000 cm^{-1} increased. In addition, a split positive and negative peak close to 1500 cm^{-1} grows in intensity as the CNT is exposed to the plasma. These trends are due to oxidation of the C=C double bonds on the nanotube, which breaks the conjugated ring structure, as discussed later.

The absorbance spectra of the carbon nanotube sheets are plotted in Figure 4.7. Figure 4.7(a) shows the spectra between 1400 cm^{-1} and 1800 cm^{-1} , with baseline correction by forcing 3 points at 1500 cm^{-1} , 1620 cm^{-1} and 1800 cm^{-1} to zero intensity. Figure 4.7(b) shows the spectra

Table 4.1. Carbon distribution on the surface of plasma treated carbon nanotube sheets.

Functional Groups	0 sec	2 sec	10 sec	30 sec	60 sec
sp ² & sp ³	> 98	84.3	80.1	74.8	71.7
C-O	< 2	10.7	14.9	17.0	18.5
C=O	-	2.6	2.3	5.9	7.7
O-C=O	-	2.4	2.7	2.3	2.0

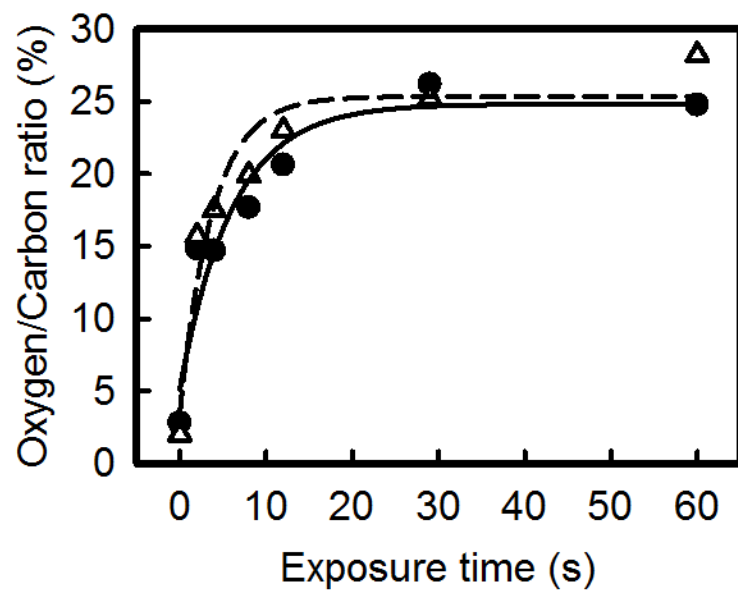


Figure 4.5. The oxygen to carbon ratio as a function of plasma exposure time (solid circles from O1s peak intensity; and open triangles from C1s peak intensity of oxidized carbon atoms).

between 2800 cm^{-1} and 4000 cm^{-1} with baseline correction at 2800 cm^{-1} and 4000 cm^{-1} . Positive peak at 1565 cm^{-1} (no. 1) is assigned to the C=C stretch of a non-conjugated olefin [6, 26, 27], whereas the negative peak at 1590 cm^{-1} (no. 2) is assigned to the C=C stretch of conjugated aromatic species [28, 29]. The presence of the two peaks demonstrates that exposing the carbon nanotube to the helium and oxygen plasma converts a fraction of the C=C double bonds into C-C single bonds. Note, according to the deconvoluted XPS result, C=O stretches associated with ketones and carboxylic acid should have appeared between 1680 and 1710 cm^{-1} [6, 30], however they are not observed. This may be due to insufficient signal-to-noise ratio for absorption by carbonyl and carboxyl groups in the transmission mode. The narrow peak at 3150 cm^{-1} (no. 3) is due to the stretching vibrations of isolated hydrogen groups. By contrast, the broad band from 3000 to 4000 cm^{-1} is assigned to the O-H stretching vibration of hydrogen-bonded hydroxyl groups [6, 31, 32]. The infrared absorption spectra indicate that hydroxyl groups are the dominant oxygenated species formed on the CNT after exposure to the atmospheric pressure helium and oxygen plasma. These findings are in agreement with the XPS results.

4.3.3 Dispersion in resin

The dispersion of the CNT yarns in dicyclopentadiene monomer is shown in Figure 4.8. Figure 4.8(a) shows that CNTs exposed to the plasma without the coupling agent do not disperse into the resin, because the liquid remains clear. Figure 4.8(b) shows that CNTs exposed to [(5-bicyclo[2.2.1]hept-2-enyl)ethyl]trimethoxysilane coupling agent without exposure to the plasma do not disperse in this resin. By contrast, it is observed in Figure 4.8(c) that CNTs which are first exposed to the plasma then treated with the coupling agent disperse in the resin, yielding a dark yellow suspension. This proves that exposing carbon

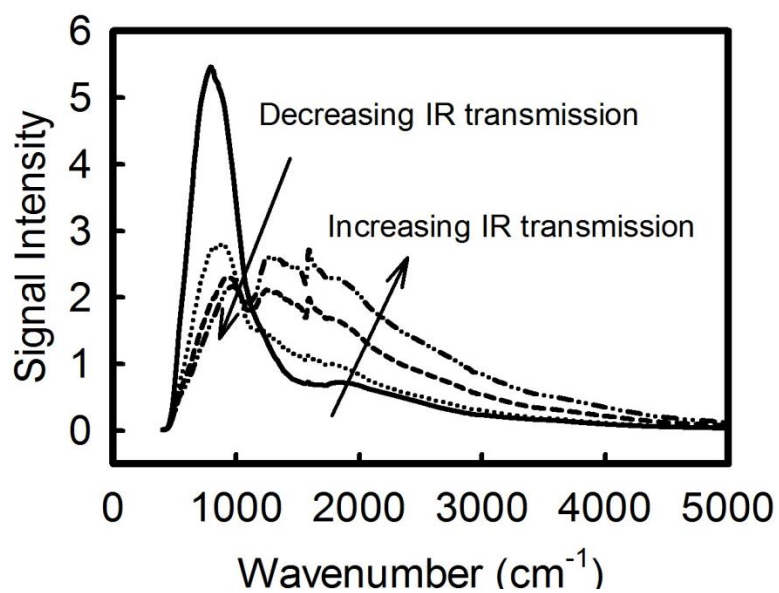


Figure 4.6. Infrared single beam spectra of CNT sheet following plasma exposures for 0.0 (—), 0.5 (-·-·), 5.0 (- - -), and 30.0 (····) s.

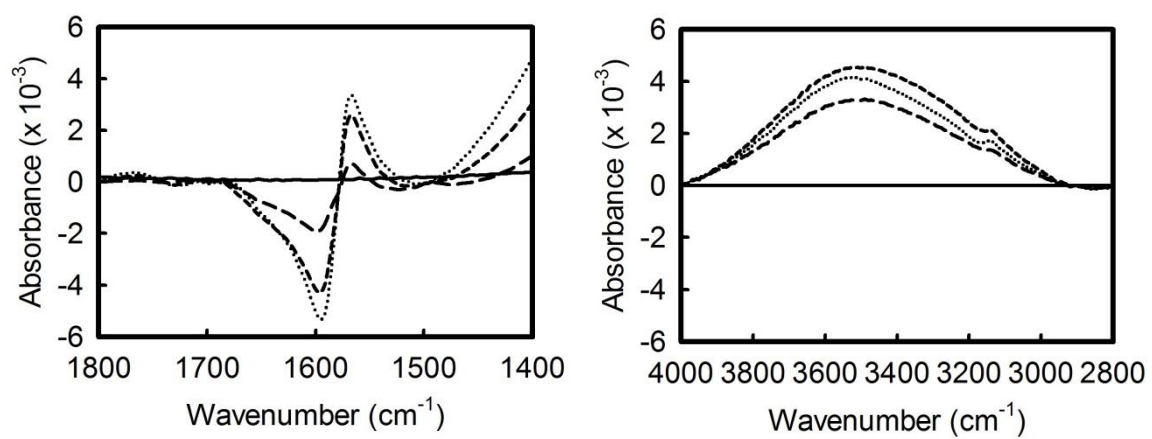


Figure 4.7. Infrared absorbance spectra of CNT as a function of exposure time to the plasma for 0.0, 0.5, 5.0, and 30.0 s.

nanotubes to the atmospheric pressure, helium and oxygen plasma activates them for reaction with the coupling agent and dispersion into the DCPD resin. Only a combined treatment by the plasma and the coupling agent was able to disperse the CNTs into the resin.

4.3.4 Surface morphology

Shown in Figure 4.9(a) thru (d) are scanning electron micrographs of the control sample and the sampled treated with the plasma for 30 s at 19,000X to 170,000X. Note that the fibrous strands in the images are bundles of CNT, each of which contains approximately 20 individual nanotubes. Prior to plasma treatment, the nanotube bundles were held together in a densely knitted mesh by van der Waals forces. Exposing the sample to the atmospheric pressure plasma led to the breakdown of the conjugated aromatic structure, which weakens the van der Waals interactions that hold the nanotube bundles together. As a result, the packing density of the bundles in image (c) is lower than that recorded in image (a). The plasma may also etch away amorphous carbon coating the CNT. The samples were further inspected at 150,000 and 170,000X magnifications, respectively. Image (b) shows that 200 nm amorphous carbon agglomerates are imbedded in the bundles of untreated CNT. Image (d) shows that plasma removes large amorphous agglomerates and leaves behind small clusters on the bundle surface. These clusters are most likely low-molecular-weight carbon materials that are byproducts of the oxidation process [19]. It is unclear whether these clusters are formed from CNT or from amorphous carbon imbedded in the bundles.

The interaction between the plasma and the nanotubes occurs on the surface of the bundles. Presently, there is no evidence showing that the plasma has penetrated into the bundles. Using the Brunauer, Emmett, and Teller's (BET) adsorption method, an average diameter of 9.4

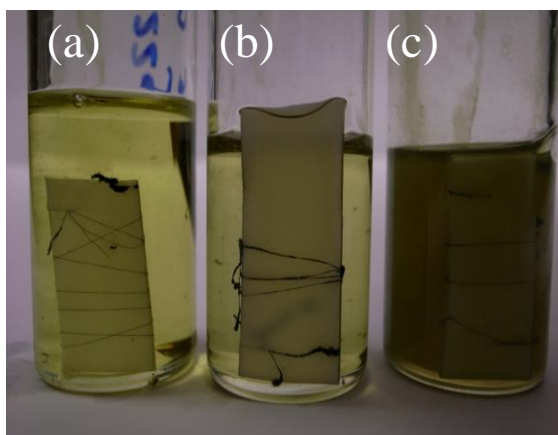


Figure 4.8. CNT yarns exposed to (a) plasma only, (b) coupling agent only; and (c) plasma then coupling agent. A combined treatment by the plasma and the coupling agent is required to disperse the CNTs into the resin.

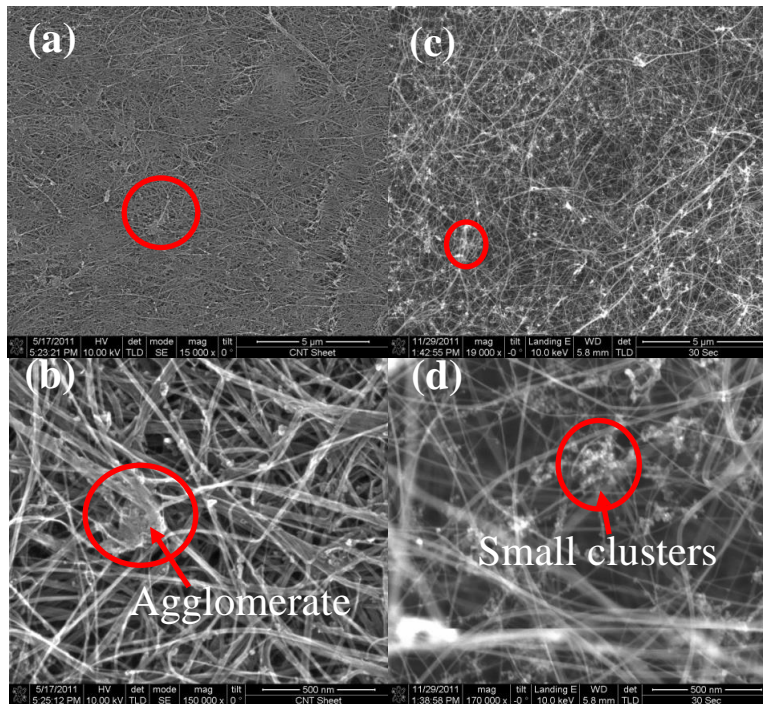


Figure 4.9. Scanning electron micrograph of CNT sheet before plasma treatment, (a) 15,000X and (b) 150,000X; and after exposure to plasma for 30s (c) 19,000X and (d) 170,000X.

nm was measured for the pores inside of the CNT bundles. The small pore diameter will likely limit the depth of penetration of the reactive species into the bundles. In comparison the average diameter of the interspatial voids in the nanotube yarn and sheet is approximately 0.2 μm , which should be sufficient for reactive species to travel from one surface of the sheet to the other. This explains why the water contact angle on the back surface of the nanotube sheet falls after plasma exposures greater than 5 s.

4.3.5 Mechanical and electrical properties

The electrical resistivity of the carbon nanotube yarn is plotted as a function of plasma treatment time in Figure 4.10(a). The resistivity of the untreated sample is $4.4 \times 10^{-6} \Omega\text{-m}$, which is two orders of magnitude higher than the electrical resistivity of graphene sheet [33]. The resistivity of the CNT yarn increases with exposure to the atmospheric pressure helium and oxygen plasma. After 2, 10, and 60 s treatment, the yarn rises to 6.3, 7.9, and $9.5 \times 10^{-6} \Omega\text{-m}$, respectively. After about 20 s, the yarn resistivity approaches the saturation value of $9.5 \times 10^{-6} \Omega\text{-m}$. This value is lower than the resistivity of carbon fibers commonly used in composites, such as T700 with a resistivity of $1.6 \times 10^{-5} \Omega\text{-m}^1$. The dependence of the resistivity on plasma exposure time t follows an exponential curve given by:

$$R(t) = R_o + (R_{Max} - R_o)[1 - \exp(-k_R t)], \quad (3)$$

where R_o is the sample resistivity before plasma exposure, R_{Max} is the saturated resistivity value, and k_R is the first-order rate constant for the change in the resistivity with exposure time. The best fit of Eq. (3) is plotted in Figure 4.10(a) as a solid line, and the rate constant, k_R , is 0.12 s^{-1} . This rate constant is close to the first order rate for the oxidation of carbon atoms $k_{O/C}$ (0.22 s^{-1}). In Figure 4.10(b), the resistivity is plotted against the oxygen-to-carbon ratio measured by XPS.

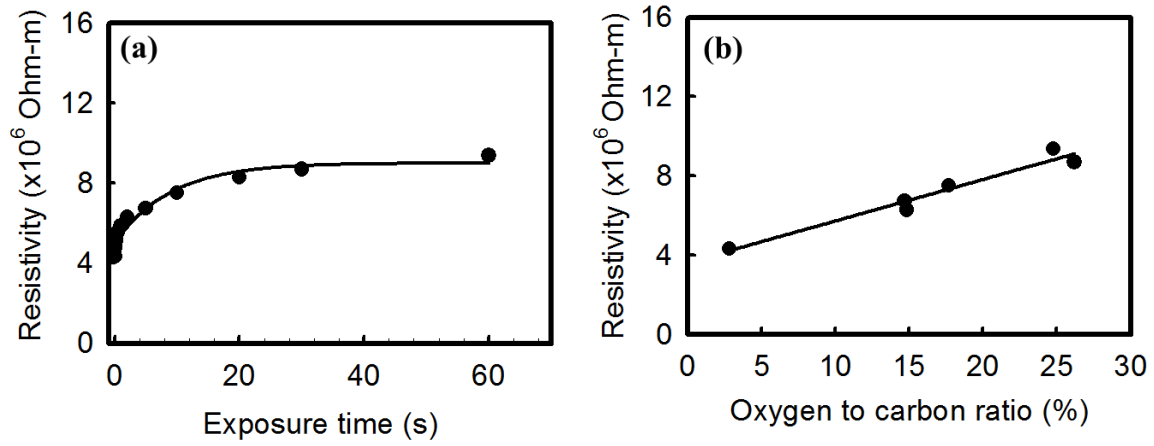


Figure 4.10. The electrical resistivity of the CNT yarn as a function of (a) the plasma exposure time, and (b) the oxygen to carbon ratio on the surface of the nanotubes.

A linear relationship is observed, confirming that the change in electrical resistivity is due to oxidation of the CNT.

The tensile strength of the nanotube yarn was also measured as a function of the exposure time under the helium and oxygen plasma. This result is plotted in Figure 4.11. For exposure times ranging from 0 to 12 s, the average tensile strength of the yarn dropped approximately 27% from 553.1 MPa to 403.8 MPa. The average tensile strength as a function of the exposure time has been fitted with a line, yielding a slope of 11.8 MPa/s. It is speculated that plasma activation reduces the tensile strength of the yarn primarily by weakening the van der Waals forces that hold the nanotube bundles together, rather than damaging the nanotube themselves.

4.4 Discussion

The radio frequency, atmospheric pressure, helium and oxygen plasma utilized in this work has been demonstrated to be an effective method for activating aromatic polymers [19, 34-36]. The detailed plasma chemistry has been studied by Jeong et. al. [37], and Gonzalez et. al. [36]. The plasma was reported to have an electron density ranging from 10^{11} to 10^{12} cm^{-3} at an average electron temperature of 1.5 eV. Interaction of the energetic free electrons with approximately 3.3×10^{17} cm^{-3} of molecular oxygen in helium generates approximately 8.0×10^{16} cm^{-3} ground state O (^3P), 8.0×10^{16} cm^{-3} metastable O₂ ($^1\Delta_g$), 2.0×10^{15} metastable O₂ ($^1\Sigma_g^+$), and 2.9×10^{15} O₃. Predicted profiles of these species in the exit beam from the plasma source are presented in Figure 4.12 [36]. The concentration of charged species may be neglected due to the high recombination rate for ions and electrons, and the lack of any source for ionization downstream of the electrodes [37].

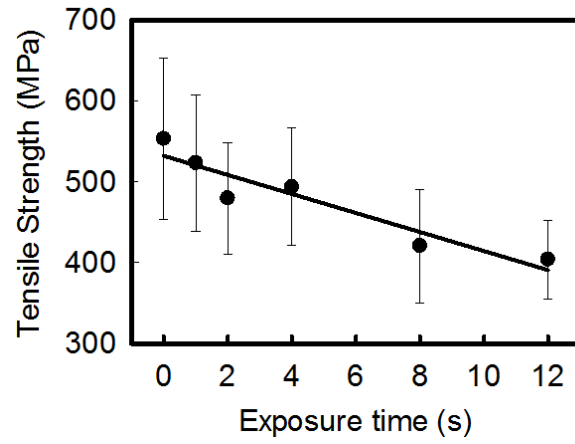


Figure 4.11. The tensile strength of CNT yarn as a function of the plasma exposure time.

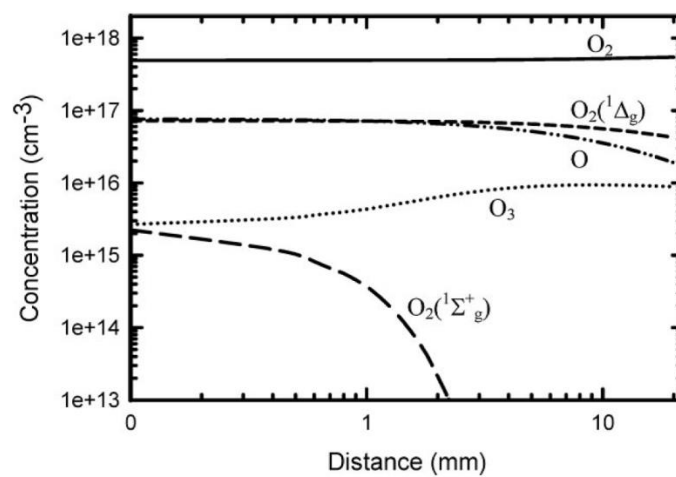


Figure 4.12. Dependence of the concentration of neutral species on distance from the atmospheric RF plasma exit at 200 W power, 40 L/min He, and 0.8 L/min O₂ [36].

Other ionized gas systems that have been used to functionalize carbon nanotubes include vacuum plasmas, arc-like discharges, dielectric barrier discharges, and radio frequency argon and oxygen plasma. The estimated concentrations of atomic oxygen, [O], and ozone, [O₃], produced in these different discharges are shown in Table 4.2 [38-48]. The estimated oxygen atom concentration in the vacuum plasma is approximately $1.0 \times 10^{14} \text{ cm}^{-3}$, and the concentration of ozone is below $1.0 \times 10^{10} \text{ cm}^{-3}$ [45-47]. The reactive species concentration of the arc discharge is estimated for inside the arc, where the atomic oxygen concentration can be as high as 10 % by volume of the gas, while the ozone concentration is below $1.0 \times 10^{10} \text{ cm}^{-3}$ [45]. Note that the temperature of the arc, which is several thousand degrees Celsius, renders it unsuitable to treat the CNT directly. Instead, the discharge is cooled by blowing air at high velocity through the arc. This decreases the concentration of the reactive species in the afterglow by several orders of magnitude. To the author's knowledge, no published estimates are available for the atomic oxygen and ozone concentration in the afterglow of an arc discharge fed with air. Estimates of the oxygen atom concentration in dielectric barrier discharges ranges from 1.0×10^{11} to $1.0 \times 10^{14} \text{ cm}^{-3}$ [39, 48]. However, the ozone concentration produced by the DBD can be as high as $1.0 \times 10^{18} \text{ cm}^{-3}$. This is because conditions within this device (i.e., high density plasma streamers dispersed throughout the air) are favorable towards ozone generation from atomic and molecular oxygen [39, 45, 48]. The concentration of reactive species in the atmospheric pressure, RF, argon and oxygen plasma has not been published in previous work. We believe that the properties of the argon and oxygen plasma should be similar to the plasma used in this work, if operated at similar conditions.

Listed in Table 4.3 is the extent of oxidation for carbon nanotubes that are treated by different processes. Chen et. al. [7] reported on vacuum plasma oxidation of CNT. Their plasma was operated at 100 W in 200 mTorr of oxygen. It oxidized up to 23.3% of the carbon atoms on

Table 4.2. Atomic oxygen and ozone concentrations reported for the plasma systems used to treat carbon nanotubes.

Systems	Gas feed	[O] (cm ⁻³)	[O ₃] (cm ⁻³)	Ref.
Vacuum	Oxygen	10 ¹⁴	< 10 ¹⁰	7,45-47
Arc discharge	Air	~10 ^{18**}	<10 ¹⁰	38,39,45
Dielectric Barrier	Air	10 ¹² -10 ¹⁴	10 ¹⁶ -10 ¹⁸	38-40,42,45
Atmospheric RF Plasma	1.5% O ₂ in He	10 ¹⁶ -10 ¹⁷	10 ¹⁵ -10 ¹⁶	36,37,41,44,45

** Atomic oxygen concentration of the arc discharge is estimated for inside of the arc.

Table 4.3. Effect of treatment method and time on the extent of oxidation and distribution of oxidized species on the surface of nanotubes.

Treatment method	Time	% Oxidized carbon	% C-OH	% C=O	% O-C=O	Ref.
Vacuum plasma	2-30 min	24.3	18.2	4.0	2.1	7-9
Arc-like discharge	3 s	6.9	5.3	-	1.6	12-13
Dielectric barrier discharge	4 s	8.2	6.6	-	1.6	5,14,15,49
Atmospheric Ar/O ₂ Plasma	2-3 min	8.5	-	-	-	16-18
Atmospheric He/O ₂ Plasma	30 s	25.2	17.0	5.9	2.3	this work
Acid Bath	1-24 hr	23.0	9.8	6.8	6.4	5,23,27

the CNT surface after a 20 min treatment. About 75% of the bound oxygen was attributed to hydroxyl groups with the remainder split between carbonyl groups and carboxylic acid groups. Similarly, Chen et. al [8] and Wang et. al. [9] oxidized carbon nanotubes using microwave vacuum plasma that operated at 700 W. Treatment times ranged from 5 to 15 min. It was found that conversion into hydroxyls dominated at lower exposure times, while carboxylic acids were the main product after 10 min.

Kolacyk et. al. [12] used an arc-like discharge to functionalize the CNT at temperatures in the afterglow from 400 to 900 °C. In their study, the nanotubes were dispersed in distilled water and then injected into the plasma through a nebulizer. After the CNT spent approximately 3s in the plasma, 6.9% of the nanotube surface became oxidized, with a hydroxyl to carboxyl ratio of 3.2 [12-13]. The oxidation of carbon nanotubes by atmospheric pressure dielectric barrier discharge was reported by Okpalugo et. al [14]. Prior to the process, the samples were first dispersed in methanol, and then deposited on gold or silicon substrates as a thin film by the drop-dry technique. Subsequently, the CNT film was exposed to the atmospheric pressure air plasma for 4 seconds at 500 W of delivered power. Approximately 8% of carbon atoms on the surface of the film were oxidized, with 80% of these forming hydroxyl groups.

Charlier et. al., Demoisson et. al., and Claessens et. al. have reported on the oxidation of carbon nanotubes using a radio frequency, argon and oxygen plasma. Claessens report that exposing CNT to the plasma operated at 80 W and 0.07 vol% oxygen flow for 3 minutes converted 8.5 % of the sp^2 - sp^3 carbons into oxidized functional groups. The distribution of the oxidized carbons, however, was not reported. With the RF, AP, helium and oxygen plasma investigated herein, the rate of oxidation is faster compared to the other plasma systems. As shown in Figure 4.5, only 10 s exposure is needed to oxidize 20 % of surface carbon atoms, and 25 % are oxidized after 30

s. The distribution of oxidized species is same as in other studies, with ~70% of the oxidized carbon atoms appearing as alcohols (C-OH).

Carbon nanotubes have also been oxidized by immersion in strong acid [15, 22]. This process takes from 1 to 24 hours. The degree of oxidation is 20-25 %, similar to that obtained with plasmas, but requires hours instead of seconds to complete. The distribution of oxygen containing functional groups produced by acid treatment is shown in Table 4.3. Compared to plasma, fewer hydroxyl groups and more carbonyls and carboxylic acids are formed.

A mechanism is proposed in Figure 4.13 for the activation of carbon nanotubes by atomic oxygen. Since the atomic oxygen concentration in the afterglow of the radio frequency helium and oxygen plasma is 8 times higher than that of ozone, reaction by ozone is neglected. In the first step, atomic oxygen is inserted into the aromatic double bond forming a three-member epoxy ring. This is analogous to the mechanism observed for the oxidation of graphite with O atoms [50,51]. The strain in the epoxy group is relieved in step (2) when a water molecule from ambient air reacts with the epoxy group, opening the ring and inserting a diol across the original C=C double bond. Although some authors have suggested that the hydroxyl groups can undergo further oxidation to produce carbonyl or carboxylic acid groups [8], the data obtained in the present study indicates that this reaction does not occur to a large extent during plasma activation.

The presence of hydroxyl groups on the nanotube surface is verified by results shown in Figure 4.8, since [(5-bicyclo[2.2.1]hept-2-enyl)ethyl]trimethoxysilane coupling agents react readily to hydroxyl groups only. Functionalizing carbon nanotubes with hydroxyl groups should make it possible to attach other molecules, e.g. polymers, to the CNT surface, while keep the structure relatively intact. However, this approach is not without potential drawbacks, such as increased resistivity (Figure 4.10) and decreased yarn strength (Figure 4.11).

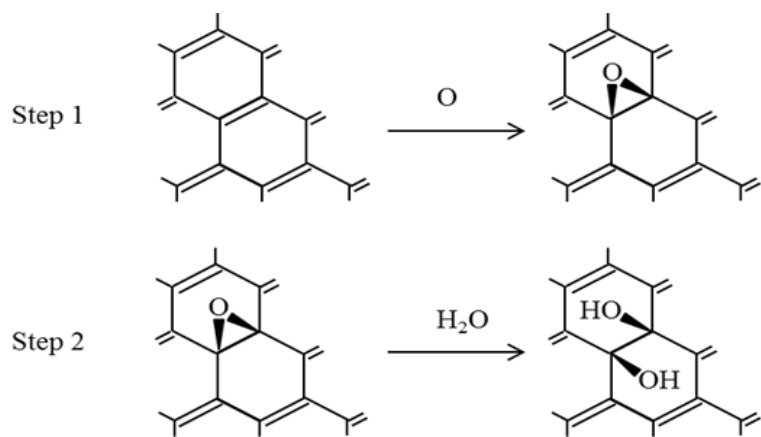


Figure 4.13. A proposed mechanism for the oxidation of carbon nanotubes by exposure to the atmospheric pressure, helium and oxygen plasma.

4.5 Summary

A radio frequency, atmospheric pressure, helium and oxygen plasma was used to functionalize carbon nanotube yarn and sheet. Exposing the CNT to the plasma for 10 s converted 20% of the carbon atoms on the surface of the nanotube bundles into oxidized species, of which 75% were hydroxyl groups. The electrical resistivity of the nanotube yarn increased in direct proportion to the extent of oxidation. A small reduction in the tensile strength of the yarn was observed following the treatment as well.

Acknowledgements

We would like to thank the US government for providing the required funding for this work.

References

- [1] Iijima S. Helical Microtubules of Graphitic Carbon. *Nature*. 1991;354(6348):56-8.
- [2] Tasis D, Tagmatarchis N, Bianco A, Prato M. Chemistry of carbon nanotubes. *Chemical Reviews*. 2006;106(3):1105-36.
- [3] Hirsch A, Vostrowsky O. Functionalization of Carbon Nanotubes. *Functional Molecular Nanostructures*. In: Schlüter AD, ed.: Springer Berlin / Heidelberg 2005, p. 193-237.
- [4] Osorio AG, Silveira ICL, Bueno VL, Bergmann CP. H₂SO₄/HNO₃/HCl— Functionalization and its effect on dispersion of carbon nanotubes in aqueous media. *Appl Surf Sci*. 2008;255(5, Part 1):2485-9.
- [5] Ziegler KJ, Gu Z, Peng H, Flor EL, Hauge RH, Smalley RE. Controlled Oxidative Cutting of Single-Walled Carbon Nanotubes. *Journal of the American Chemical Society*. 2005;127(5):1541-7.
- [6] Naseh MV KA, Mortazavi Y, Sahraei OA, Pourfayaz F, Sedghi SM. Functionalization of Carbon Nanotubes Using Nitric Acid Oxidation and DBD Plasma. *World Academy of Science, Engineering and Technology*. 2009;49:3.
- [7] Chen W, Liu X, Liu Y, Bang Y, Kim H-I. Preparation of O/W Pickering emulsion with oxygen plasma treated carbon nanotubes as surfactants. *Journal of Industrial and Engineering Chemistry*. 2011;17(3):455-60.
- [8] Chen C, Liang B, Ogino A, Wang X, Nagatsu M. Oxygen Functionalization of Multiwall Carbon Nanotubes by Microwave-Excited Surface-Wave Plasma Treatment. *The Journal of Physical Chemistry C*. 2009;113(18):7659-65.

- [9] Wang S, Wang T, Li Y, Zhao X, Han J, Wang J. Plasma Activation of Integrated Carbon Nanotube Electrodes for Electrochemical Detection of Catechol. *Plasma Science and Technology*. 2007;9(2):194.
- [10] Felten A, Bittencourt C, Pireaux JJ. Radio-Frequency Plasma Functionalization of Carbon Nanotubes Surface O₂, NH₃, and CF₄ Treatments. *Journal of Applied Physics*. 2005;98(7):0743081-0743089.
- [11] Lobo AO, Ramos SC, Antunes EF, Marciano FR, Trava-Airoldi VJ, Corat EJ. Fast Functionalization of Vertically Aligned Multiwalled Carbon Nanotubes Using Oxygen Plasma. *Material Letters*. 2012;70:89-93.
- [12] Kolacyak D, Ihde J, Lommatzsch U. Carbon nanotube functionalization by atmospheric pressure plasma and post-plasma reactions. *Surface and Coatings Technology*. 2011;205, Supplement 2(0):S605-S8.
- [13] Kolacyak D, Ihde J, Merten C, Hartwig A, Lommatzsch U. Fast functionalization of multi-walled carbon nanotubes by an atmospheric pressure plasma jet. *Journal of Colloid and Interface Science*. 2011;359(1):311-7.
- [14] Okpalugo TIT, Papakonstantinou P, Murphy H, Mclaughlin J, Brown NMD. Oxidative functionalization of carbon nanotubes in atmospheric pressure filamentary dielectric barrier discharge (APDBD). *Carbon*. 2005;43(14):2951-9.
- [15] Wang W-H, Huang B-C, Wang L-S, Ye D-Q. Oxidative treatment of multi-wall carbon nanotubes with oxygen dielectric barrier discharge plasma. *Surface and Coatings Technology*. 2011;205(21–22):4896-901.
- [16] Claessens N, Demoisson F, Dufour T, Mansour A, Felten A, Guillot J, Pireaux JJ, Renier F. Carbon nanotubes Decorated with Gold, Platinum and Rhodium Clusters by Injection

- of Colloidal Solutions Into the Post-Discharge of an RF Atmospheric Plasma. *Nanotechnology*. 2010;21:3856031-3856036.
- [17] Demoisson F, Raes M, Terryn H, Guillot J, Migeon HN, Reniers F. Characterization of Gold Nanoclusters Deposited on HOPG by Atmospheric Plasma Treatment. *Surface and Interface Analysis*. 2008;40:566-570.
- [18] Charlier JC, Arnaud L, Avilov IV, Delgado M, Demoisson F, Espinosa EH, Ewels CP, Felten A, Guillot J, Ionescu R, Leghrib R, Llobet E, Mansour A, Migeon HN, Pireaux JJ, Reniers F, Suarez-Martinez I, Watson GE, Zanolli Z. Carbon Nanotubes Randomly Decorated with Gold Clusters: From Nano²hybrid Atomic Structures to Gas Sensing Prototypes. *Nanotechnology*. 2009;20:3755011-3755010.
- [19] Gonzalez E, Barankin MD, Guschl PC, Hicks RF. Remote Atmospheric-Pressure Plasma Activation of the Surfaces of Polyethylene Terephthalate and Polyethylene Naphthalate. *Langmuir*. 2008;24(21):12636-43.
- [20] Tougaard S, Jansson C. Background Correction in XPS: Comparison of Validity of Different Methods. *Surface and Interface Analysis*. 1992;19:171-174.
- [21] Wagner CD, Muilenberg GE. Handbook of x-ray photoelectron spectroscopy: a reference book of standard data for use in x-ray photoelectron spectroscopy: Perkin-Elmer Corp., Physical Electronics Division; 1979: 38-39.
- [22] International A. Tensile Properties of Single Textile Fibers. West Conshohocken, PA: ASTM International. 2011: 864-873.
- [23] Sahoo NG, Cheng HKF, Li L, Chan SH, Judeh Z, Zhao JH. Specific Functionalization of Carbon Nanotubes for Advanced Polymer Nanocomposites. *Advanced Functional Materials*. 2009;19(24):3962-71.

- [24] Ago H, Kugler T, Cacialli F, Salaneck WR, Shaffer MSP, Windle AH, et al. Work functions and surface functional groups of multiwall carbon nanotubes. *Journal of Physical Chemistry B*. 1999;103(38):8116-21.
- [25] Vanattekum PMTM, Wertheim GK. Excitonic Effects in Core-Hole Screening. *Phys Rev Lett*. 1979;43(25):1896-8.
- [26] Mawhinney DB, Naumenko V, Kuznetsova A, Yates JT, Liu J, Smalley RE. Infrared spectral evidence for the etching of carbon nanotubes: Ozone oxidation at 298 K. *Journal of the American Chemical Society*. 2000;122(10):2383-4.
- [27] Zhao C, Ji L, Liu H, Hu G, Zhang S, Yang M, et al. Functionalized carbon nanotubes containing isocyanate groups. *Journal of Solid State Chemistry*. 2004;177(12):4394-8.
- [28] Paredes JI, Villar-Rodil S, Martinez-Alonso A, Tascon JMD. Graphene oxide dispersions in organic solvents. *Langmuir*. 2008;24(19):10560-4.
- [29] Hontoria-Lucas C, López-Peinado AJ, López-González JdD, Rojas-Cervantes ML, RM. Study of oxygen-containing groups in a series of graphite oxides: Physical and chemical characterization. *Carbon*. 1995;33(11):1585-92.
- [30] Lee DW, De Los Santos L, Seo JW, Felix LL, Bustamante A, Cole JM, et al. The Structure of Graphite Oxide: Investigation of Its Surface Chemical Groups. *Journal of Physical Chemistry B*. 2010;114(17):5723-8.
- [31] Socrates G. *Infrared characteristic group frequencies*: Wiley; 1980.
- [32] Herzberg G. *Infrared and Raman spectra of polyatomic molecules*: R.E. Krieger Pub. Co.; 1991.
- [33] Chen JH, Jang C, Xiao SD, Ishigami M, Fuhrer MS. Intrinsic and extrinsic performance limits of graphene devices on SiO₂. *Nat Nanotechnol*. 2008;3(4):206-9.

- [34] Gonzalez E, Barankin MD, Guschl PC, Hicks RF. Ring Opening of Aromatic Polymers by Remote Atmospheric-Pressure Plasma. *Ieee T Plasma Sci.* 2009;37(6):823-31.
- [35] Gonzalez E, Hicks RF. Surface Analysis of Polymers Treated by Remote Atmospheric Pressure Plasma. *Langmuir.* 2010;26(5):3710-9.
- [36] Gonzalez E, Barankin MD, Guschl PC, Hicks RF. Surface Activation of Poly(methyl methacrylate) via Remote Atmospheric Pressure Plasma. *Plasma Processes and Polymers.* 2010;7(6):482-93.
- [37] Jeong W, Kessler MR. Toughness Enhancement in ROMP Functionalized Carbon Nanotube/Polydicyclopentadiene Composites. *Chemistry of Materials.* 2008;20(22):7060-8.
- [38] Tendero C, Tixier C, Tristant P, Desmaison J, Leprince P. Atmospheric pressure plasmas: A review. *Spectrochimica Acta Part B-Atomic Spectroscopy.* 2006;61(1):2-30.
- [39] Fridman A, Chirokov A, Gutsol A. Non-thermal atmospheric pressure discharges. *Journal of Physics D: Applied Physics.* 2005;38(2):R1.
- [40] Sakai O, Kishimoto Y, Tachibana K. Integrated coaxial-hollow micro dielectric-barrier-discharges for a large-area plasma source operating at around atmospheric pressure. *Journal of Physics D-Applied Physics.* 2005;38(3):431-41.
- [41] Park J, Henins I, Herrmann HW, Selwyn GS. Gas breakdown in an atmospheric pressure radio-frequency capacitive plasma source. *Journal of Applied Physics.* 2001;89(1):15-9.
- [42] Kang WS, Kim HS, Hong SH. Atomic oxygen generation by in-situ plasma and post-plasma in dielectric barrier discharges for surface treatment. *Thin Solid Films.* 2010;518(22):6578-82.

- [43] Trelles J, Chazelas C, Vardelle A, Heberlein J. Arc Plasma Torch Modeling. *Journal of Thermal Spray Technology*. 2009;18(5):728-52.
- [44] Moravej M, Hicks RF. Atmospheric plasma deposition of coatings using a capacitive discharge source. *Chem Vapor Depos*. 2005;11(11-12):469-76.
- [45] Schutze A, Jeong JY, Babayan SE, Park J, Selwyn GS, Hicks RF. The atmospheric-pressure plasma jet: A review and comparison to other plasma sources. *Ieee T Plasma Sci*. 1998;26(6):1685-94.
- [46] Vrlinic T, Mille C, Debarnot D, Poncin-Epaillard F. Oxygen atom density in capacitively coupled RF oxygen plasma. *Vacuum*. 2009;83(5):792-6.
- [47] Vesel A, Mozetic M, Balat-Pichelin M. Oxygen atom density in microwave oxygen plasma. *Vacuum*. 2007;81(9):1088-93.
- [48] Valentin IG, Gerhard JP. The development of dielectric barrier discharges in gas gaps and on surfaces. *Journal of Physics D: Applied Physics*. 2000;33(20):2618.
- [49] Datsyuk V, Kalyva M, Papagelis K, Parthenios J, Tasis D, Siokou A, et al. Chemical oxidation of multiwalled carbon nanotubes. *Carbon*. 2008;46(6):833-40.
- [50] Aviles F, Cauich-Rodriguez JV, Moo-Tah L, May-Pat A, Vargas-Coronado R. Evaluation of mild acid oxidation treatments for MWCNT functionalization. *Carbon*. 2009;47(13):2970-5.
- [51] Ajayan PM, Yakobson BI. Materials science - Oxygen breaks into carbon world. *Nature*. 2006;441(7095):818-9.

Chapter 5

Thermal, Electrical and Tensile Characterization of CNT/DCPD Sheet Composite

Abstract

Flexible carbon nanotube sheet has been stretched mechanically to 25 % elongation, chemically treated with dicyclopentadiene (DCPD) monomer, and cured into a composite. The composite exhibited average tensile strength of 640 MPa, elastic modulus of 28 GPa and density of 1.5 g/cm³. The thermal conductivity and electrical resistivity of the composite were 0.3 W/m-K and 2.6×10^{-3} ohm-m, respectively. Furthermore, the carbon nanotube composite had less than 1.0 wt% moisture uptake after soaking 7 days at 60 °C and 95 % humidity. These properties compare favorably to other sheet materials used in aerospace systems, such as 7075-T7 aluminum and aramid-fiber.

5.1. Introduction

Fiber-reinforced polymer composites are widely used in aerospace applications due to superior strength-to-weight ratio relative to metals [1]. Currently, most of the composites used on planes and satellites are reinforced with continuous carbon fibers. However, carbon fibers are extremely stiff and break when undergoing a knot test. Such stiffness limits the use of continuous carbon fiber as a structural support in applications such as honeycomb core, satellite antenna, and cable, where flexible material is required [2]. Fibers composed of carbon nanotubes (CNT) with high ultimate tensile strength and elongation to failure, but with relatively low modulus, have been considered as a potential alternative to continuous carbon-fiber composites.

The ultimate tensile strength of individual single wall and multi-walled nanotubes has been reported to be as high as 150 and 80 GPa [3-6], respectively. The modulus of elasticity of the CNT ranges from 0.9 to 1.2 TPa [3-6], and the elongation to failure is between 5 and 15 % [5-8]. Nevertheless, the use of carbon nanotubes as a reinforcement in thermoset or thermoplastic composites has been limited by poor dispersion and low fiber loading [9-12]. If the rule of mixtures is obeyed, then at 10 % loading, the mechanical properties of the composite will be limited to about 10% of that of the CNT alone [12].

Nanocomp Technologies Inc. and the University of Cambridge have independently developed a method to fabricate carbon nanotube aerogels via chemical vapor deposition (CVD) [13-14]. The aerogel network can be condensed into a micro-porous sheet [13-14]. The CNT sheet is flexible, but stiffens up when combined with a resin matrix. It has been shown that prepregs with up to 60% fiber loading can be fabricated by high-pressure injection of BMI/solvent into the porous sheets [15].

We have developed a method to produce composites by infusing Nanocomp's carbon nanotube sheet with dicyclopentadiene (DCPD), a low viscosity resin [16]. Jeong and Kessler [17] have established the strong affinity of DCPD towards CNT. When the sheets are submerged in the resin, monomer molecules infiltrate the porous structure without any applied pressure. A composite of mechanically aligned CNT sheet, cured in DCPD, exhibits a threefold improvement in tensile strength compared to sheet that is aligned, but not made into a composite [16].

Herein, we describe a composite fabricated from functionalized carbon nanotube sheet and dicyclopentadiene. This method is similar to that reported by us previously [16], except that the surface of the CNT fibers have been chemically modified prior to polymer infusion to achieve better crosslinking. The product has an average tensile strength higher than 600 MPa, which is comparable to that of aerospace grade aluminum 7075-T6 [18]. The structural, thermal, electrical and environmental properties of this novel composite material are presented below.

5.2. Experimental Methods

5.2.1. Materials

The carbon nanotube sheets, EMSHIELD™, were acquired from Nanocomp Technologies, Inc. The areal density of the as-grown sheets was measured to be approximately 15 grams per square meter (g/m^2). The nanotubes were collected on a drum rotated at 6 m/min and were partially aligned by the rotational motion. Once collected from the drum, the sheets were treated to consolidate and reduce the interspatial voids.

The dicyclopentadiene used in this work was supplied by Materia, Inc. (CAS #77-73-6), and it contained approximately 70.0 mole% dimers and 30.0 mole% trimers. The monomer consists of two 5-member rings, each with a pair of double bonds located at the opposite ends of

the molecule. Polymerization of DCPD occurred by a Diels-Alder reaction that was catalyzed by a second generation Grubbs Catalyst (CAS #246047-72-3) obtained from Sigma Aldrich Corp. The resin to catalyst ratio used in this work was 1500:1.

There were two types of proprietary functional chemicals used in this work. The first chemical (A) was responsible for bridging the nanotubes, and the second one (B) was used to crosslink the CNTs to the resin matrix. These molecules had one or two alkoxy-silane groups for bonding to oxygenated groups present on the activated nanotube surfaces.

5.2.2. Sample preparation

The sheet was first activated by being exposed to an atmospheric pressure, helium and oxygen plasma, operated at 150 W RF power, 30 SLM He flow, and 0.5 SLM O₂ flow (Atomflo™ 400 by Surfx Technologies LLC). The sheet was treated for 15 s on each side. The plasma-activated sheet was mounted on Instron grips and stretched at 1 mm/min until 25 % elongation was achieved. During stretching, the CNT sheet was kept wet with toluene. At the end of the chemical/mechanical treatment, the samples were heated to evaporate any excess solvent.

Next, the carbon nanotube sheets were immersed in a resin catalyst mixture for 30 seconds. The resin infused samples were then sandwiched between two perforated release plies lined with bleeder ply and compressed to 5.0 MPa to extrude the excess resin. The samples were placed in between flat fluorinated polymer films and cured at 14.0 MPa pressure. The cure cycle consisted of 2 hours at 60 °C, and 5 hours at 150 °C. Finally, the samples were cooled to below 30 °C before being released from the press.

5.2.3. Characterization

The density of the CNT/DCPD composite was measured using a helium pycnometer in accordance to ASTM D2638-10 [19]. The sample chamber was pressurized to a set value and then connected to a second chamber of the same volume initially under vacuum. The volume of the samples was calculated using Boyle's law, and the density was obtained from the known sample mass. The fiber weight fraction in the composites was estimated from thermogravimetric analysis (TGA) in air. This procedure utilized a modified version of ASTM D3171-99 [20]. Since the resin and the nanotubes have different oxidation temperatures [16], mass loss with increased temperature can be related to the resin and nanotube content. Furthermore, the ratio between nanotubes and the residue catalyst is fixed, thereby, the mass of the residual iron oxide as a fraction of the total mass can be used to provide confirmation of the estimated fiber fraction.

The porosity of the CNT sheet before resin infusion was calculated from nitrogen BET data collected at 77 K using a Micromeritics ASAP 2020 analyzer. The nitrogen adsorption method, coupled with the Barrett-Joyner-Halenda analysis, is effective in characterizing pore sizes ranging from 1 to 300 nm. Pit defects and any interfacial delamination in the composite were detected using ultrasonic scanning (Sonoscan, Inc). The resolution of the ultrasonic sound wave was 20 μm .

The electrical conductivity of the composites was measured at room temperature using a SII287 electrochemical test station (Solartron Analytical). The thermal conductivity of the samples was obtained using a DTC-300 thermal conductivity meter by TA Instruments. The measurements were collected using a range 2 measurement cylinder (0.002 to 0.02 $\text{m}^2\text{K/W}$) from 20 to 100 $^\circ\text{C}$. Modulated differential scanning calorimetry was performed on a Discovery DSC

from TA Instruments, and the heat capacity was calculated using data from 20 to 100 °C, ramped at 2 °C/min. The thermal expansion coefficient (CTE) measurements were collected from a Q400 thermo-mechanical analyzer (TA Instruments), using a heat-cool-heat protocol starting from -10 °C and increasing to 110 °C at 1 °C per minute under 0.05N load.

Tensile strength, modulus of elasticity, and elongation to failure were measured on an Instron 5966, dual-column testing system following a modified ASTM D3822 procedure. Each sample was cut to 20 mm x 2 mm in size and mounted onto a paper frame. Once gripped with the clamps, the paper frame was cut open, and the sample was stretched at 5 mm/min until failure. The ultimate tensile strength and elongation to failure were recorded at the time sample failure occurred. The Young's modulus was calculated from the linear slope of the elastic region on the stress-strain curve, which is usually between 0.0 and 0.5 % elongation. The fracture surface of the CNT/DCPD was inspected with a Nova 600 NanoLab DualBeam™ SEM/FIB from FEI.

The moisture uptake of the CNT/DCPD composite was measured following ASTM D5229. Samples cured under vacuum and under air were both placed in an environmental chamber operating at 60 °C and 95 % humidity. The mass change due to moisture uptake by the samples was recorded daily for seven days.

5.3. Results

5.3.1. Structural properties

The measured density of the CNT/DCPD composite material is approximately 1.5 g/cm³. Figure 5.1 shows the mass loss (solid line) and derivative mass loss (dotted line) of the sheet, as determined by TGA in air. The mass loss curve has three downward stair steps at 350, 500 and

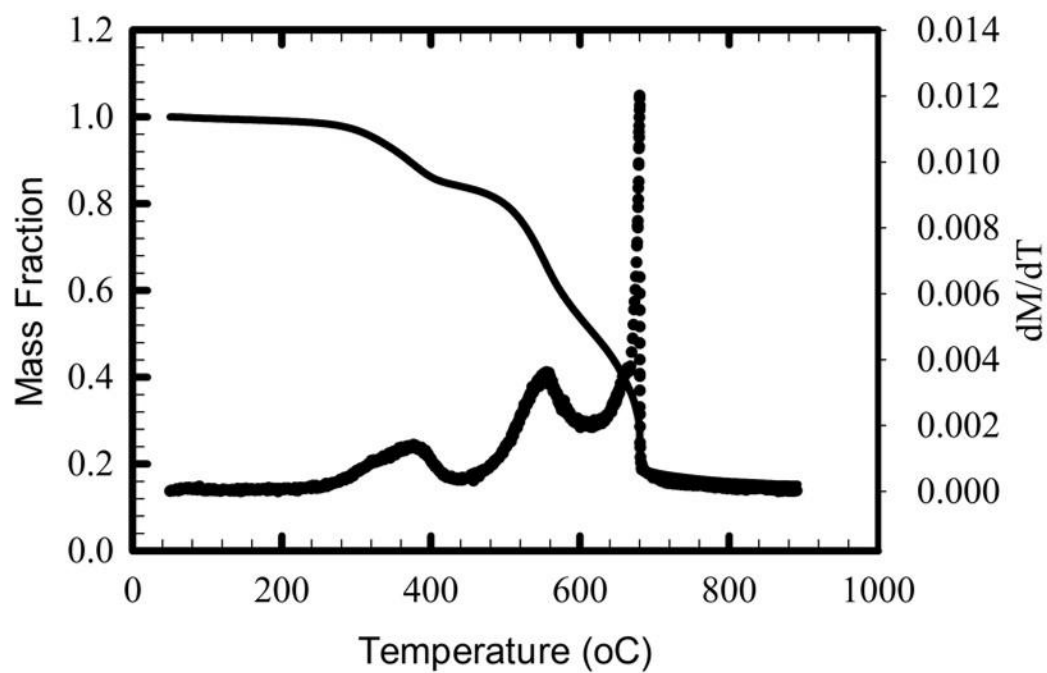


Figure 5.1. The TGA mass loss of CNT composite (—) and the derivative of mass loss with temperature (····).

600 °C, before reaching a baseline at 700 °C. This information is also reflected by the four peaks in the derivative plot. Mass loss prior to 550 °C is assigned to DCPD decomposition as suggested by the mass loss of DCPD in TGA measured in our previous work [16]. Only a small fraction of the CNTs decompose below this temperature. Integrating the area under the derivative peaks reveals that the CNT accounts for 60 ± 5 wt% of the composite. The mass of the oxidized catalyst residue accounts for 15 wt% of the composite. In the as-received sheet, the oxidized catalyst residue makes up 27 ± 3 wt%. Comparing these two values for the catalyst weight fraction indicates that the CNT fiber fraction in the composite is about 50 ± 5 wt%. This value is in good agreement with the fiber weight fraction estimated from the TGA mass loss.

Shown in Figure 5.2 (a) are the nitrogen adsorption isotherms of the CNT sheet before and after mechanical alignment. Figure 5.2 (b) shows the volume distribution of pores with different diameters. The solid lines represent the as-received samples and the dotted lines represent the sheets after mechanical alignment. Integrating the adsorbed nitrogen volume over all pore sizes between 1.7 and 300.0 nm shows negligible change in the total adsorbed volume before and after mechanical stretching. The adsorbed volume decreased from 0.755 to 0.749 cm^3g^{-1} , which is within the error of the measurement. It is noted that nitrogen adsorption in pores with diameters below 10 nm remains unaffected by mechanical stretching, while adsorption in pores with diameters ranging from 10 to 50 nm shows some changes. The smaller pores are thought to correspond to the spaces within the nanotube bundles, while the larger diameter pores are more likely associated to the spaces between the fiber bundles. Since the amount of adsorbed nitrogen did not change much, it is proposed that the change in the diameter of the pores in the range from 35 to 25 nm is a result of structural rearrangement of the CNT

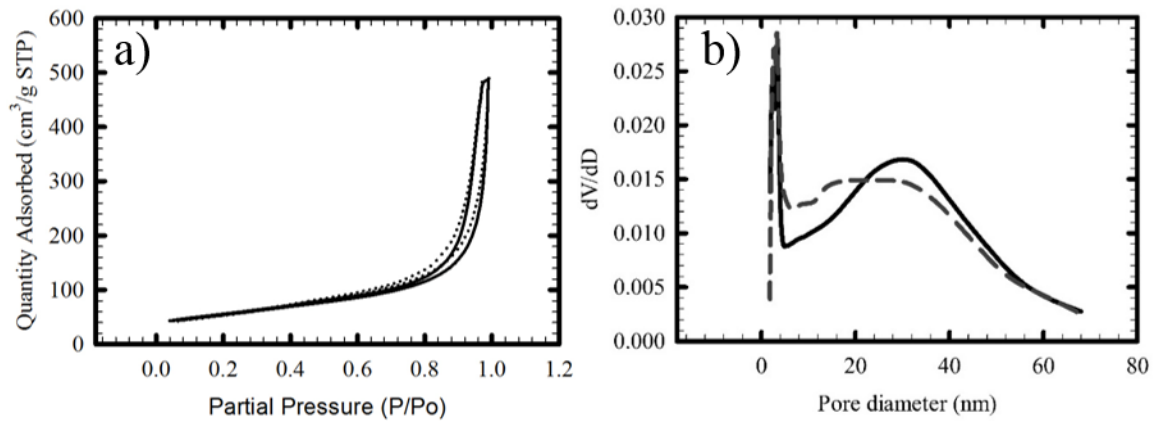


Figure 5.2. (a) Nitrogen adsorption isotherm of CNT sheet before (—) and after (- - -) mechanical alignment. (b) Pore volume distribution in CNT sheet before (—) and after (- - -) mechanical alignment.

network. There is no evidence for elimination of pores through consolidation and alignment of the nanotubes. Whether large voids exist in the composite was examined by ultrasonic scanning. It was found that less than 0.5 vol.% of the composite contains voids with a diameter larger than 20 μm .

5.3.2. Electrical and thermal properties

The electrical and thermal properties of the DCPD/CNT composite are presented in Table 5.1. The electrical resistivity measured across the planar direction of the CNT/DCPD sheet is 2.6×10^{-3} ohm-m. The in-plane thermal conductivity of the composite is 0.27 W/m-K at 25 °C, and increases slightly to 0.3 W/m-K at 100 °C. The specific heat of the composite measured at 100 °C is 0.98 J/g-K. Lastly, the coefficient of thermal expansion is 0.12 $\mu\text{m}/\text{m-K}$. In general, these numbers are comparable to conventional carbon-fiber-reinforced epoxy composites [21,22].

5.3.3. Tensile properties

The stress-strain curves of the CNT sheets and sheet composites are shown in Figure 5.3 (a) and (b). In both figures, the solid line represents unmodified CNT, or composites fabricated from unmodified sheets. The dashed, dashed-dotted, and dotted lines in (b) represent the composites fabricated from stretched, chemically functionalized, and stretched plus chemically functionalized CNT sheets. It is noted that stretching and/or chemical functionalization increases the tensile strength of the composites, while at the same time, decreasing their elongation to failure. The tensile properties of these materials are summarized in Table 5.2. It is observed that mechanically stretching the CNT sheets increases their ultimate tensile strength from 51 ± 9 to 77 ± 10 MPa, while reducing the elongation to failure from 24 ± 1 to 8 ± 1 %. Infusion and

Table 5.1. Electrical and thermal properties of CNT/DCPD composite at 25 °C.

	Electrical resistivity (Ω -m)	Thermal conductivity (W/m-K)	Specific heat (J/g-K)	CTE (μ m/m- $^{\circ}$ C)	Ref.
CNT/DCPD	3×10^{-3}	0.3	0.98	0.12	--
Aligned CNT	5.28×10^{-6}	31 W/m-K	---	--	[23]
CF/Epoxy	1.5×10^{-3}	0.5 - 1.5	1.1	-	[21,22]

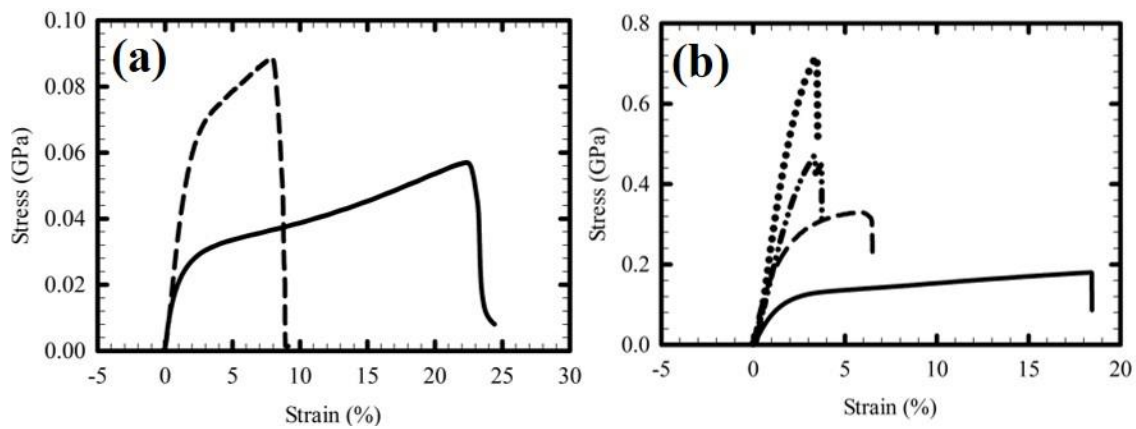


Figure 5.3. Stress strain curve of (a) CNT sheet before (—) and after (- - -) stretching, and (b) stress and strain curve of the DCPD/CNT composite fabricated from CNT sheet as-received (—), stretched (- - -), functionalized (— · - ·), and stretch and functionalized (· · ·).

Table 5.2. Tensile properties of CNT sheet and DCPD/CNT composites.

	Tensile Strength (MPa)	Elastic Modulus (GPa)	Elongation (%)
DCPD	45	2.0	5.5
As-received sheet	50 ± 9	2.1 ± 0.8	24.0 ± 1.0
Stretched sheet	80 ± 10	3.3 ± 0.8	8.0 ± 1.2
CNT/DCPD	200 ± 30	10 ± 2	19.0 ± 2.0
s-CNT/DCPD	345 ± 30	18 ± 4	6.9 ± 0.2
f-CNT/DCPD	420 ± 40	19 ± 3	4.4 ± 0.6
s-f-CNT/DCPD	640 ± 50	28 ± 4	3.7 ± 0.2

polymerization of DCPD throughout the CNT produces a composite with a tensile strength and elongation to failure of 200 ± 30 MPa and 19 ± 2 %, respectively. If the CNT sheets are first stretched and then infused and cured with DCPD, the tensile strength increases to 345 ± 30 MPa, while the elongation to failure drops to 6.9 ± 0.2 %. Similar strength and elongation values of the composite are achieved by functionalizing the CNT instead of stretching it: 420 ± 40 MPa and 4.4 ± 0.6 %. Finally, stretching and functionalizing the CNT, followed by infusing and curing DCPD into the sheet yields a composite with the highest tensile strength and lowest elongation to failure: 640 ± 50 MPa, and 3.7 ± 0.2 %, respectively.

The Young's modulus of the as-received CNT sheet is 2.1 ± 0.8 GPa. This value increases to 3.3 ± 0.8 GPa after it is stretched to enhance fiber alignment. The modulus of the CNT sheet with infused and cured DCPD resin is 9.6 ± 2.0 GPa. If one modifies the CNT sheets by stretching, functionalization, and application of both of these processes, and then polymerizes the DCPD throughout the matrix, the Young's modulus increases to 18 ± 4 GPa, 19 ± 3 GPa, and 28 ± 4 GPa, respectively. Note that the modulus for dicyclopentadiene polymer is 2.0 GPa [24]. In summary, by combining the CNT sheet together with the DCPD resin in a composite, and enhancing the interaction between these two components by mechanical and chemical means, one produces a material that is 12 times stronger and 14 times tougher than the CNT sheet by itself.

5.3.4. Moisture uptake

The moisture uptake of the CNT/DCPD composite measured over the course of 7 days is shown in Figure 5.4. The fractional mass change of the sample cured under vacuum is negligible over the testing period. This is consistent with the fact that both dicyclopentadiene polymer and carbon nanotubes are hydrophobic. However, if the composite is cured in air instead, the

material absorbs up to 3.0 wt% water, which is comparable to the uptake of cured epoxy composites. It may be that during curing in air, some oxidation of the polymer occurs that makes the material more hydroscopic.

5.4. Discussion

The CNT sheet composite fabricated in this work is intended for uses in aerospace applications where high-strength and flexibility is required. In order to produce enough material for practical applications, the CNT sheet used in the composite is a product of high-volume CVD growth by Nanocomp [25]. The growth rate of the Nanocomp CVD process depends on the amount of catalyst added, and to produce material at a reasonable rate, the amount of catalyst in the sheet must be >10 wt%. Unless specifically treated, these catalysts remain in the CNT sheet, primarily at junctions between the nanotube bundles. The tensile strength of the un-modified CNT sheet used in this study is 50 MPa.

Previous work has shown that mechanically stretching the CNT structure helps to align the nanotubes [23,26,27]. The CNT sheets can be stretched up to a maximum of 25 % without breaking. At 25 % elongation, the degree of alignment of the nanotube bundles in the sheet is reported to be ~50 % [28], and the tensile strength increases to about 80 MPa. An electron micrograph of the as-grown sheet is shown in Figure 5.4 (a). It reveals a structure similar to that of a fishing net. The network of CNT bundles is held together by knots at the points of intersection [28]. The length of the bundles between two knots is approximately 150 nm. Figure 5.4 (b) shows that stretching the sheet causes the bundles to partially aligned in the pull direction without collapsing the network. Figure 5.2 (b), also reveals that mechanical stretching does not

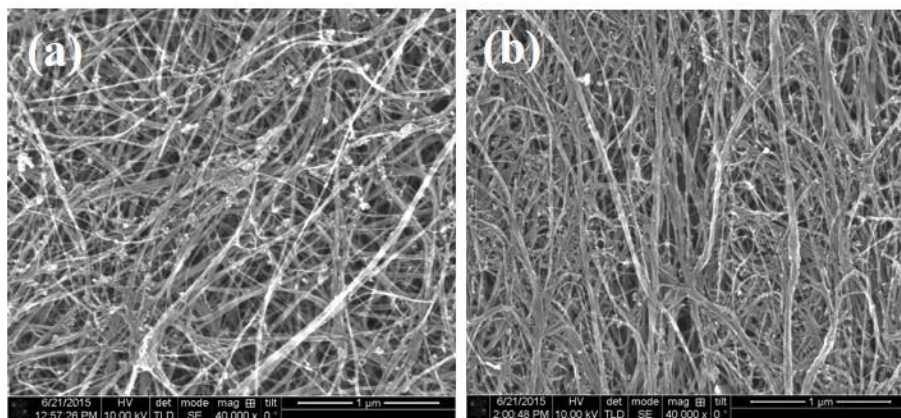


Figure 5.4 (a) Entangled CNT network in the as-grown sheet, and (b) CNT sheet after mechanical stretching.

have much affect on the volume of pores inside the sheet. Under such circumstances, 50 % alignment is probably the best that can be achieved.

The mechanical properties of the CNT sheet produced in this work and in previous studies are compared in Table 5.3. The nanotube sheet used in the present work exhibits a tensile strength of 50 MPa, which is 4 to 6 times less than materials investigated previously. For example, the CNT sheet grown by Han et al., [27], using less than 10 wt% catalyst in a CVD apparatus, had a starting tensile strength of 200 MPa. The ribbon spun by Wang et al., [26] from a forest of nanotube arrays had an initial tensile strength of 300 MPa. Cheng et al., [23] acquired their carbon nanotube sheets from Nanocomp, Inc., but their material was grown at a slower rate than the material used herein, and it started with a tensile strength of 200 MPa. In these cases, the differences in the tensile strength of the nanotube sheets may be traced back to their method of preparation.

After mechanical stretching, a tensile strength of 80 MPa is observed in this study, compared to 600 to 670 MPa reported previously. This difference may be attributable to the level of mechanical alignment achieved by stretching. As can be seen in Figure 5.4 (b), the nanotube bundles remain entangled in a porous network after stretching to 25% elongation, and do not collapse into a consolidated array of nanotubes. By contrast, Han et al., [27] reported 80% alignment of the nanotubes by stretching his fiber to 20 % elongation. Cheng [23] claimed to have aligned up to 90 % of the nanotubes in his sheet by stretching it to 40%. Wang [26] reported that pulling his CNT ribbon through a stretch roller aligned 90% of the bundles. These authors attributed the enhancement in the tensile strength of the nanotube sheet to an increase in the contact area between the nanotube surfaces after consolidation [23,26,27].

Table 5.3. Tensile strength and elastic modulus of CNT sheet and composite this work and reported previously.

	As-received sheet		Stretched sheet		Stretched sheet composite	
	Strength (MPa)	E.Modulus (GPa)	Strength (MPa)	E.Modulus (GPa)	Strength (MPa)	E.Modulus (GPa)
This Work	50	2	80	3	340	18
Han [27]	200	--	600	12	5,000	245
Wang [26]	300	21	--	--	4,000	266
Cheng [23]	205	1	668	25	2,000	169

The tensile strength of DCPD/CNT composites made from stretched nanotube sheet in this study is 340 MPa. In prior work, the stretch-aligned CNT sheet was infused with epoxy or bismaleimide (BMI) resin and cured to make a composite [23,26,27]. The tensile strengths of these composites were reported to be between 2 and 5 GPa were observed. The reason for this discrepancy is not entirely clear. As discussed above, the CNT sheet used herein is produced in large quantities for commercial applications. In this material the nanotube bundles cannot be consolidated into a dense array where all the nanotubes are in close contact with each other. In contrast, SEM pictures from previous studies show the starting material to consist of loosely arranged nanotube bundles without any knots tying them down [23,26,27]. Electron micrographs of these samples after stretching show ropes of nanotube bundles consolidated and aligned in the direction of stretching. Without knots, the nanotube bundles can be consolidated into a closely packed array. Nevertheless, no data has been reported on the porosity of the stretched sheet, so the extent of contact between nanotubes is not known.

To compensate for the lower strength of the material in the present work, chemical functionalization was used to further enhance the load sharing between the nanotube bundles in the composite. In this case, the tensile strength and elastic modulus increase to 640 ± 50 MPa and 28 ± 4 GPa, respectively. The interaction between the resin and the CNT network may be explained via a Capstan effect, where the nanotube bundles are forced to press and wrap around the resin through a tortuous path [16]. The frictional force between the resin and the nanotubes helps to prevent the bundles from slipping and pulling out under tension. Similarly, chemical crosslinking should confine the nanotube movement, and prevent the CNT bundles from sliding past each other. Electron micrographs of the composites made with chemical functionalization

show that fiber breakage occurs at the fracture interface, without the nanotubes pulling out of the resin.

In the previous work, the authors may have reported the tensile strength of the CNT composites as a function of the skeletal density of the nanotubes instead of the density of the composite [28-29]. This approach normalizes the stress calculation to demonstrate the force carried by the carbon nanotubes. The stress σ_{CNT} can be determined using equation (1) below:

$$\sigma_{CNT} = \frac{P_{Load}}{\lambda} \times \rho_{CNT} \quad (1)$$

where σ_{CNT} is the tensile stress in (N/m^2), P_{Load} is the measured load (N), λ is the linear density ($tex = g/km$), and ρ_{CNT} is the skeletal density of the nanotubes. The linear density can be calculated using equation (2):

$$\lambda = wt \times \rho_{Sheet} \quad (2)$$

where w and t are the width and thickness, and ρ_{sheet} is the density of the CNT sheet. Here, equations (1) and (2) can be combined to give:

$$\sigma_{CNT} = \sigma_T \times \frac{\rho_{CNT}}{\rho_{sheet}} \quad (3)$$

where σ_T is the tensile strength of the composite, and ρ_{sheet} is calculated based on the composite density and fiber wt%. The strength calculated by this method can be as high as 2 times the value of the composite strength calculated from the cross section. This combined with the lower strength of the starting CNT sheet could explain the differences reported in Table 5.3.

The CNT sheet composites reported here may be produced in large quantities for commercial applications. Therefore, it is instructive to compare the mechanical properties of the CNT/DCPD

composites to conventional carbon-fiber-reinforced composites (CFRC). These properties are listed in Table 5.4. The density of the CNT/DCPD composite is comparable to the CFRC, but its tensile strength and modulus are less than the value of the CFRC. However, the CNT/DCPD sheet composite is more flexible than any of the CFRCs. Shown in Figure 5.5 is a ten layer sheet composite from this work bent to a U shape without any signs of breaking or delamination. Furthermore, the nanotube sheet itself has passed a knot test without breaking, which is not possible for conventional carbon fiber. This allows CNT sheet to be shaped into complex parts and then fabricated into composites. Although the CNT/DCPD composite may not match CFRC in strength and stiffness, it is applicable to flexible or complex structures where carbon fiber cannot be used.

An example of a flexible composite application is the core of honeycomb structures. Currently, honeycomb cores are made from either aerospace grade aluminum or from aramid paper. The density, strength and modulus of aluminum 7075-T6 and Nomex® aramid-fiber are also shown in Table 5.4. The tensile strength of the CNT/DCPD composite exceeds both Nomex® paper and aluminum, while its density and Young's modulus [cite] falls in between the two materials. The higher density of the CNT composite in comparison to previously published values [16,23,26-29] is due to the increased catalyst loading for high volume production. The average Young's modulus of the CNT composite is about half the modulus of the aluminum sheet. However, the specific strength and elastic modulus of the CNT composite is 150% and 60% of aluminum, respectively. In applications where weight is more critical than volume, the CNT composite has an advantage over aluminum.

The thermal and electrical conductivity of the dicyclopentadiene/carbon nanotube composite is comparable to carbon-fiber-reinforced epoxy composites. Its moisture uptake, if

Table 5.4. Density, tensile strength, Young's modulus, and elongation to failure of the stretched and functionalized CNT/DCPD composite, Nomex® paper T410, and aluminum 7075-T6.

	Density (g/cm ³)	Tensile Stress (MPa)	Young's Modulus (GPa)	Elongation (%)
CNT/DCPD composite	1.5	640 ± 50	28 ± 4	3.7 ± 0.2
Int. Modulus CF/CYCOM 997	1.6	2,500	162	1.5
IM7/CYCOM 5250-4 BMI	1.6	2,900	169	< 2.0
Nomex® paper T410	0.8	93	3	12
Al-7075-T6	2.8	572	72	11

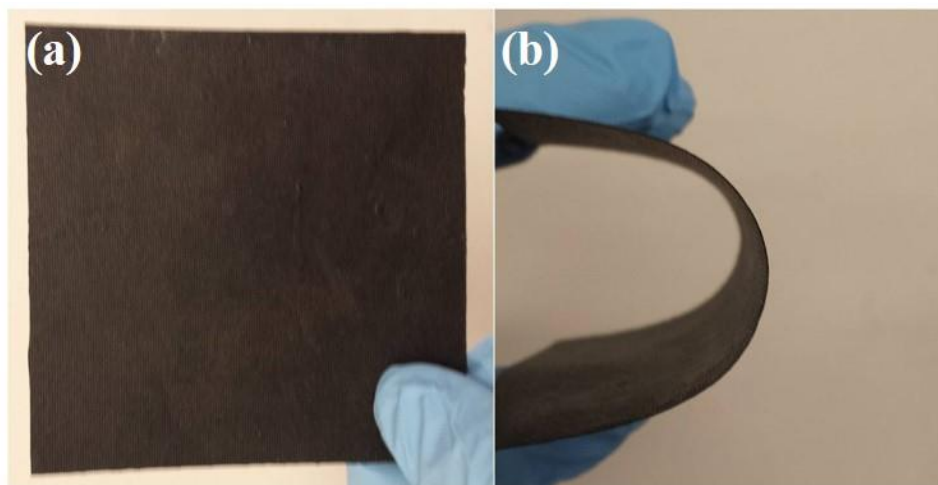


Figure 5.5. (a) A flat 10-ply CNT sheet composite and (b) a 10-ply CNT sheet bent to U shape.

cured under vacuum, is negligible, which is better than that of the currently used epoxy and BMI. This composite material has no substantial expansion with increasing temperature, which makes it suitable for applications where a thermally stable composite is needed.

5.5. Conclusions

A method of fabricating CNT/DCPD sheet composite has been developed which uses mechanical alignment and chemical functionalization to generate composites from commercially available CNT sheet. The composite produce by this method has higher tensile strength than aluminum and is more flexible than carbon-fiber-reinforced composites. The thermal conductance and electrical resistivity of the material is 0.3 W/m-K and $2.6 \times 10^{-3} \Omega\text{-m}$. If vacuum cured, this material has no appreciable moisture uptake. It can be used as an alternative to aluminum sheet in flexible applications where high strength and lightweight is needed.

•Reference

1. Manufacturing Engineering, Change-up Pitch: From metal to plastic, <http://www.sme.org/MEMagazine/Article.aspx?id=82709&taxid=1416>.
2. R. Day, S. Reznik, T. Vo, T. Sharif and Y. Vagapov, *Proceedings of the Third International Conference on Advanced Composite Materials and Technologies for Aerospace Applications* (2013).
3. M.F. Yu, B.S. Flies, S. Arepalli and R.S. Ruoff, Tensile loading of ropes of single wall carbon nanotubes and their mechanical properties, *Phys. Rev. Lett.* 84, 5552-5555 (2000).
4. R. Khare and S. Bose, Carbon nanotube based composites- a review, *Journal of Minerals & Materials Characterization & Engineering* 4, 31-46 (2005)
5. J.N. Coleman, U. Khan, W.J. Blau and Y.K. Gun'ko, Small by strong: A review of the mechanical properties of carbon nanotube-polymer composite, *Carbon* 44, 1624-1652 (2006).
6. R.S. Ruoff, D. Qian and W.K. Liu, Mechanical properties of carbon nanotubes: theoretical predictions and experimental measurement, *C.R. Physique* 4, 993-1008 (2003).
7. X.F. Zhang, Q.W. Li, Y. Tu, Y. Li, J.Y. Coulter, L.X. Zheng, Y.H. Zhao, Q.X. Jia, D.E. Peterson and Y.T. Zhu, Strong carbon-nanotube fibers spun from long carbon-nanotube arrays, *Small* 3, 244-248 (2007).
8. N.K. Naik, K.S. Pandya, V.R. Kavala, W.Zhang and N.A. Koratkar, High-strain rate compressive behavior of multi-walled carbon nanotube dispersed thermoset epoxy resin, *J. Compos, Mater.* 49, 903-910 (2015)

9. P.C. Ma, N.A. Siddiqui, G. Marom and J.K. Kim, Dispersion and functionalization of carbon nanotubes for polymer-based nanocomposites: A review, *Composites Part A* 41, 1345-1367 (2010).
10. J. Sandler, M.S.P. Shaffer, T. Prasse, W. Bauhofer, K. Shulte and A.H. Windle, Development of a dispersion process for carbon nanotubes in an epoxy matrix and the resulting electrical properties, *Polymer* 40, 5967-5971 (1999).
11. P. Garg, B.P. Singh, T.K. Gupta, I. Pandey and R.K. Seth, Effect of dispersion conditions on the mechanical properties of multi-walled carbon nanotubes based epoxy resin composite, *J. Polym. Res.* 18, 1387-1407 (2010).
12. C.X. Liu and J.W. Choi, Improved dispersion of carbon nanotubes in polymers at high concentrations, *Nanomaterials* 2, 329-347 (2012).
13. Y.L. Li, I.A. Kinloch and A.H. Windle, Direct Spinning of Carbon Nanotube Fibers from Chemical Vapor Deposition Synthesis, *Science* 304, 276-278 (2004)
14. J. Chaffee, D. Lashmore, D. Lewis, J. Mann, M. Shauer and B. White, Direct synthesis of CNT yarns and Sheets: in Proceedings of Nano Science and Technology Institute (2008).
15. Q. Cheng, J.W. Bao, J.G. Park, Z.Y. Liang, C. Zhang and B. Wang, High mechanical performance composite conductor: multi-walled carbon nanotube sheet/bismaleimide nanocomposites, *Advanced Functional Materials* 19, 3219-3225 (2009).
16. J. Severino, H. Yu, A. Wang, L. Carlson and R. Hicks, Strength of dicyclopentadiene and carbon nanotube composite sheets, *Manuscript in preparation*.
17. W.J. Jeong and M.R. Kessler, Toughness enhancement in ROMP functionalized carbon nanotube/polydicyclopentadiene composites, *Chem. Mater.* 20, 7060-7068 (2008).

18. Aerospace Specification Metals Inc., Aluminum 7075-T6; 7075-T651,
<http://asm.matweb.com/search/SpecificMaterial.asp?bassnum=MA7075T6>
19. Standard test method for real density of calcined petroleum coke by helium pycnometer, ASTM D2638-10 (2015).
20. Standard test methods for constituent content of composite materials, ASTM D3171-99 (2015).
21. Hexcel Corporation, HexTow[®] IM7 carbon fiber product data sheet:
<http://www.hexcel.com/resources/datasheets/carbon-fiber-data-sheets/im7.pdf>
22. Toray Carbon Fiber America Inc., TORAYCA[®] T300 data sheet:
<http://www.toraycfa.com/pdfs/T300DataSheet.pdf>
23. Q.F. Cheng, B. Wang, C. Zhang and Z.Y. Liang, Functionalized carbon-nanotube sheet/bismaleimide nanocomposites: mechanical and electrical performance beyond carbon-fiber composites, *Small* 6, 763-767 (2010).
24. G.O. Wilson (2002). *Novel self-healing materials chemistries for targeted applications* (Doctoral dissertation). Retrieved from ProQuest Dissertations and Theses. (Accession Order No. 3290429).
25. Nanocomp Inc., Nanocomp technology blog:
<http://www.nanocomptech.com/blog/need-to-know-part-2-sheets-tape-yarn>
26. X. Wang, Z.Z. Yong, Q.W. Li, P.D. Bradford, W. Liu, D.S. Tucker, W. Cai, H. Wang, F.G. Yuan and Y.T. Zhu, Ultrastrong, stiff and multifunctional carbon nanotube composites, *Mater. Res. Lett.* 1, 19-25 (2013).

27. Y. Han, X.H. Zhang, X.P. Yu, J.N. Zhao, S. Li, F. Liu, P. Gao, Y.Y. Zhang, T. Zhao and Q.W. Li, Bio-inspired aggregation control of carbon nanotubes for ultra-strong composite, *Sci. Rep.* 5, 11533; doi: 10.1038/srep11533 (2015).
28. J. Severino, L. Carlson and R. Hicks, Progression of alignment in stretched CNT sheets determined by wide angle X-ray scattering, *Manuscript in preparation*.
29. J. Severino, I. De Rosa, A. Venkert, H. Yu, W.B. Xin, L. Carlson and R. Hicks, Fabrication and characterization of solid composite yarns from carbon nanotube and dicyclopentadiene polymer, *Submitted to Carbon for review*.